CHARGE LOSS CORRECTION AND INTER-STRIP INTERPOLATION IN A HIGH-PURITY GERMANIUM DOUBLE-SIDED STRIP DETECTOR

by

Jason P. Hayward

A dissertation submitted in partial fulfillment
of the requirements for the degree of
Doctor of Philosophy
(Nuclear Engineering and Radiological Sciences)
in The University of Michigan
2008

Doctoral Committee:

Professor David K. Wehe, Chair
Emeritus Professor Glenn F. Knoll
Emeritus Professor Leslie W. Rogers
Associate Professor Zhong He

To my girls,
Shannon, Hannah, and Eliana

Acknowledgements

I'd like to thank my wife, Shannon, for proof-reading many drafts of my writing and for handling everything at home so I could focus on my research and writing. I also thank my advisor, David Wehe, for providing funding for my graduate education, allowing me the freedom and responsibility to learn to do research and teaching at the graduate level, and for direction, encouragement, and humor when needed. I thank Ethan Hull for providing me with the equipment I used to complete my research and for answering all of my questions. Additionally, I thank I.Y. Lee at Lawrence Berkeley National Laboratory as well as Bernard Phlips and Elena Novikova at Naval Research Laboratory for helping to get me started with my simulation work on double-sided strip detectors. I thank Jerry Fishman at NASA Marshall Space Flight Center for helping to fund my graduate work. Finally, I thank the members of my dissertation committee for volunteering their time.

Table of Contents

List of Figures

Figure

List of Tables

Table

List of Abbreviations

ACT	Advanced Compton Telescope
ADC	Analog-to-digital converter
BNC	BNC (bayonet Neill-Concelman) connector
CCE	Close Compton Event
DSSD	Double-sided strip detector
FPGA	Field-programmable gate array
FWHM	Full width at half maximum
GRETA	Gamma-ray Energy Tracking Array
HPGe	High-purity germanium
LBNL	Lawrence Berkeley National Laboratory
LLNL	Lawrence Livermore National Laboratory
LN_2	Liquid Nitrogen
mCi	milliCurie
MHz	Megahertz
NIM	Nuclear Instrumentation Module
NRL	Naval Research Laboratory
ISIR	Inter-strip interpolation ratio
SSI	Single site interaction
UM	University of Michigan
USB	Universal Serial Bus
SPARC	Scalable Processor ARChitecture

Glossary

Amorphous germanium (a-Ge): a non-crystalline allotropic form of germanium where no long range order is present, leaving atoms to form a continuous random network.

Axial direction: refers to the direction along the depth of the planar detector, which is perpendicular to either detector surface.

Bystander: a strip adjacent to a firing strip which does not collect any charge.

Charge-splitting ratio (r): for a single-site interaction which occurs in proximity to two adjacent strips, the ratio of charge collected on one strip over the charge collected by both adjacent strips.

Charge collection fraction ($1-f$): for a single-site interaction, the fraction of the total charge which is collected on one or two adjacent strips.

Charge loss fraction (f): for a single-site interaction in the vicinity of a gap between adjacent strips, the fraction of the total charge which remains uncollected by these strips.

Close Compton Event (CCE): any event where more than one interaction from the same sequence falls within the lateral bounds of two adjacent strips with respect to either detector side.

Compton imaging: the imaging of gamma radiation by use of Compton kinematics.

Compton sequence: the sequence of interactions in a detection system beginning with the Compton scatter of an incident gamma ray.

Cross-talk: undesired signal interference caused by capacitive or inductive coupling between adjacent preamplifier inputs.

Detection efficiency: for an incident radiation beam at a given gamma ray energy, the fraction of radiation quanta which are detected in a detector or detection system.

Detection system: the system of radiation detectors, readout and signal processing electronics, and other supporting hardware and software which together composing a Compton imaging instrument.

Event: any interaction or interaction sequence which causes at least one strip on each detector side to trigger in the electronic acquisition system.

Fast energy: A peak-to-peak measurement of a shaped fast signal recorded by the Spect32 system. The magnitude of the fast energy is proportional to the magnitude of the adjacent slow energy and the lateral proximity of the corresponding interaction. In the Spect32 system, fast energies are used to perform lateral position interpolation for in-strip interactions.

Fast signal: a transient signal (of zero net charge) adjacent to a strip which collects charge. The Spect32 system shapes these signals with a fast triangular filter over a time period of ~ 100 ns.

Flood field: uncollimated radiation incident perpendicularly upon the entire detector surface.

Gap event: any interaction or interaction sequence where one interaction falls close enough to a gap that: 1) some measurable fraction of its carriers remain uncollected by either adjacent strip, or 2) both adjacent strips are triggered by a Single Site Interaction.

Hevimet: an alloy of Tungsten (90%) which includes Copper and Nickel to make it lower cost and more easily machineable.

History: a simulated event.

Imaging efficiency: for an incident radiation beam at a given gamma ray energy, the fraction of radiation quanta which are selected for imaging by a detection system.

In-strip interaction: an interaction that occurs within the lateral bounds of a single strip.

Inter-strip Interpolation Ratio (ISIR): at a given gamma ray photopeak energy, the ratio of the maximum energy which can be lost to a strip gap over the FWHM of the photopeak, i.e., the photopeak formed by summing the energies of adjacent strips for all Single Site Interactions located in the gap between these strips.

Lateral direction: refers to a direction parallel to the surface of the planar detector, running along the direction of either the anode strips or the orthogonal cathode strips.

Loss Event: any interaction or interaction sequence where one interaction falls close enough to a gap that some measurable fraction of its carriers remain uncollected by either adjacent strip over the event time period.

Pitch: the lateral distance between the centers of adjacent detector strips.

Position interpolation: determination of the lateral position of an interaction with lateral resolution finer than the strip pitch, or determination of the depth of an interaction with depth resolution finer than the thickness of a single detector.

Position sensitive: characterized by a measureable change in response as interaction position in the detector changes.

Sensitivity: (gamma-ray astronomy) at a given gamma ray energy, the intensity of quanta at this energy that can be detected by a detection system at a given confidence level in a given observing time.

Single Site Interaction (SSI): an event of only one interaction that falls within the bounds of two adjacent strips with respect to each detector side.

Slow energy: An amplitude measurement of a shaped slow signal recorded by the Spect32 system. Upon energy calibration, slow energy is converted into gamma ray energy.

Slow signal: a signal on a strip which collects charge. The Spect32 system shapes these signals with trapezoidal filters over hundreds of μs to improve signal-to-noise.

Spect32: the prototype 32-channel electronic acquisition and signal processing system used with the UM HPGe double-sided strip detector.

Resolved CCE: a Close Compton Event which is properly identified by triggering and timing analysis. In the text, these are referred to as Close Compton Events.

Unresolved CCE: a Close Compton Event which is improperly identified by triggering and timing analysis. The separate interactions of these CCEs are close enough in depth that they trigger adjacent strips within 20 ns of each other, so these events are mistaken as SSIs.

1-1 event: An event which causes a single strip to trigger on each detector side. This is the expected detector response for a SSI which is in-strip with respect to both detector sides.

2-1 event: An event which causes two triggers on one detector side and one trigger on the opposite detector side.

2-2 event: An event which causes two triggers on each detector side.

2-3 event: An event which causes two triggers on one detector side and three triggers on the opposite side. It is not possible for this event to be caused by a single interaction.

Abstract

One fundamental design issue in the HPGe double-sided strip detector is the gap between strips, which makes up 1/6 of the 3 mm strip pitch in the UM detector. While a wide gap between strips reduces noise, thereby improving energy resolution, it also results in measurable charge loss in the UM detector. Charge loss on either detector side for a single interaction in a Compton sequence may eliminate that sequence from being included in image reconstruction. Furthermore, use of the signals obtained for interactions that occur in gaps is complicated by: 1) their sensitivity to the change in charge cloud geometries and 2) the difficulty of distinguishing single interactions from multiple close interactions.

In this work, methods for charge loss correction and inter-strip interpolation are described for interactions which fall in detector gaps. Over the energy range 60 – 1274 keV, charge loss correction increases photopeak counts by 15% on the anode side and 5% on the cathode side. Charge loss correction can be accomplished nearly as well when a second interaction falls beneath an adjacent strip. Inter-strip interpolation is able to determine the locations of these recovered events, yielding interaction position with lateral resolution of ~160 μm FWHM at 356 keV and ~310 μm FWHM at 662 keV. According to simulation, lateral resolution in the gap is fundamentally limited to these values due to charge cloud size, and lateral resolution < 100 μm FWHM may be achieved at 200 keV. When a second interaction falls beneath an adjacent strip, lateral resolution for the gap interaction is still finer than the width of the gap, and simulation shows potential for further improvement. These methods are suitable for real-time imaging applications, and they may be applied to other strip detector designs.

Chapter I

Introduction

I.A. The design challenge of the Advanced Compton Telescope

The aim of the Advanced Compton Telescope (ACT) is to allow imaging in the nuclear line region of the gamma ray spectrum (200 keV – 10 MeV) with significantly improved sensitivity. This will allow improved observation of nucleosynthesis products and dynamics of supernovae and novae. The mission is the primary tool "to uncover how supernovae and other stellar explosions work to create the elements." The ACT will also allow for improved imaging of other galaxies, pulsars, black holes, gamma-ray bursts, and other astrophysical objects [1].

The sensitivity of a gamma ray telescope is its most important design parameter because it allows for the observation of very faint nuclear line emissions from distant supernovae. At a given gamma ray energy, the sensitivity characterizes the intensity $\left(\gamma' s / cm^2 s\right)$ of quanta at this energy that can be detected by the detection system at a given confidence level (ex: 3σ) in a given observing time. For continuous spectra, broad band sensitivity S is defined as:

$$S = \frac{n_\sigma \sqrt{\frac{B}{(\Delta E / t_{obs})}}}{A_{eff}}$$

where n_σ is the confidence level, B is the background count rate, ΔE is the width of the energy band, t_{obs} is the observing time, and A_{eff} is the effective area. The effective area depends on the detection area, the detector total efficiency, the dead time, the imaging efficiency, the transparency of all material along the photon path, and energy thresholds. The narrow line sensitivity characterizes the intensity of an unresolved line that can be detected by the detection system at a given confidence level in a given observing time. There are two major differences in its definition. First, the peak efficiency is used instead of total efficiency. Second, it is computed on an energy band equal to the instrument spectral resolution (FWHM). [2]

The sensitivity is affected mainly by system energy resolution, position resolution, and detection efficiency. The background rejection methods employed are also very important, as data collected in astrophysical applications are background dominated. The background rejection methods also depend heavily upon position and energy resolution. The aggressive ACT design goal is 3σ sensitivity of 10^{-7} $\gamma' s / cm^2 s$ at 847 keV over 10^6 s, though astrophysical science would benefit from sensitivity to gamma ray quantities as low as 10^{-8} $\gamma' s / cm^2 s$. Doppler broadening of spectral lines to 3-5% must also be considered for one major objective [1].

In the literature, the Advanced Compton Telescope is projected to have a sensitivity 10-50 times that of its predecessor, COMPTEL (~10^{-5} γ $cm^{-2}s^{-1}$). This projection stems from its use of position sensitive detectors with excellent spatial resolution, which aid in

background rejection and dramatically reduce the width of the Compton scattered photon angle [1]. Yet, it would benefit NASA's mission to be able to improve sensitivity by two more orders of magnitude.

Both silicon and high-purity germanium (HPGe) double-sided strip detectors (DSSDs) have been proposed as part of the baseline concept for the ACT. While Naval Research Laboratory (NRL) is the lead on silicon DSSD development for the ACT, Lawrence Berkeley Laboratory (LBL) has taken leadership on HPGe DSSD development. NRL proposed that one way to dramatically improve sensitivity is to determine the direction of Compton scattered electrons in the detector material. An initial feasibility study revealed that this was improbable in DSSDs. Subsequently, other technical challenges in HPGe DSSD development were pursued.

I.B. Double-sided strip detector design challenges

This work addresses the first of the primary technical challenges with use of HPGe DSSDs, as stated in the ACT report [1], "optimization of the electrode and guard ring geometries… and exploration of inter-strip interpolation to optimize position resolution." Another primary technical challenge concerns the transfer of technology to a commercial manufacturer to provide the large number of detectors required for an ACT. In fact, the UM HPGe detector was the first of its kind obtained from the only commercial manufacturer of HPGe DSSDs, PHDs Co [3]. Upon delivery of the detector, the fundamental design issue remaining was stated: "What happens to charge collected in gaps between strips? Do we need narrower gaps [for improved energy position]? Can fabrication changes address and fix these issues?" [4]

D. Protic, the second of three HPGe DSSD fabricators worldwide, also recently identified gap design as an important area of study for improved detector performance. Measurements on an HPGe DSSD showed some abnormal pulses coming from interactions in the gap region, and no explanation was found for these pulses. It was also suggested that energy resolution may be improved by both widening and deepening of the grooves in between strips to reduce the contributions of capacitance and dielectric noise to energy resolution. Finally, the exploitation of charge-splitting for the best possible position resolution was advised [5].

M. Amman and P.N. Luke of LBNL are the third group worldwide that design HPGe DSSDs. In 2007, they published a paper discussing the current state of technical challenges remaining for HPGe DSSDs with amorphous semiconductor contacts [6]. Fundamental design issues identified included: (1) excessive leakage at temperatures significantly above that of liquid nitrogen, (2) leakage current degradation with temperature cycling, and (3) charge collection to inter-contact surfaces. Referring to the third issue, design changes similar to those proposed by Protic were recommended. Additionally, they recommended the development of signal processing techniques to correct for charge loss.

I.C. Approach to address ACT and DSSD design challenges

As discussed, ACT sensitivity improvement and related detector fabrication questions provide the primary motivation for this work. The solution to many of the design challenges focuses around the detector gap, as does the approach discussed in this work. In Section C.1, the detector response to gap interactions is introduced. In Section C.2, the

complications specific to gap interactions are introduced. In Section C.3, the approach to address ACT and DSSD design challenges is introduced.

I.C.1. Detector response to gap interactions

According to the Shockley-Ramo theorem [7], the charge Q and current i on a strip induced by a moving point charge q are given by:

$$Q = -q\varphi_o(\vec{r})$$

$$i = q\vec{v}(\vec{r}) \cdot \vec{E}_o(\vec{r}) \qquad (1)$$

where φ_o and $\vec{E}_o$ are the weighting potential and field at position $\vec{r}$, and $\vec{v}$ is the velocity of the point charge at $\vec{r}$. Simulation shows that the region of steepest gradient in φ_o is located in the gap between strips. The velocity $\vec{v}$ also varies most rapidly in the gap region, especially near the gap surface, where electric field is strongest and most non-uniform. Consequently, the induced current i varies most rapidly as a function of position in this region, making it the most position-sensitive area. Simulation and experiment results presented in this work show that the gap is sensitive even to the size and orientation of the charge-carrier clouds produced by energetic electrons. These energetic electrons come from photo-interactions in germanium.

I.C.2. Complications specific to gap interactions

Although the gap is very position sensitive, use of the data obtained for interactions that occur in the vicinity of a gap are complicated by: 1) incomplete charge-carrier collection, or charge loss, 2) the signal variance introduced by charge-carrier cloud size,

orientation, and lateral spreading, and 3) the difficulty of distinguishing single interactions from multiple close interactions. These three complications and their significance are further discussed in II.B. As a whole, they decrease efficiency, introduce unwanted background counts, degrade energy resolution, and result in increased position uncertainty using current interpolation methods, thereby reducing detection sensitivity.

I.C.3. Approach: improved readout methodology for gap interactions

In this work, measurement-based methods for charge loss correction and inter-strip interpolation for gap interactions in the UM HPGe DSSD are described. These novel methods treat the case where a second interaction falls beneath an adjacent strip, increasing their effectiveness for use in Compton imaging over a wide range of gamma ray energies.

This work is first-of-its-kind in multiple ways. The detector itself is the first detector of its kind, incorporating new amorphous germanium (a-Ge) strip, cryostat, and preamplifier designs. It is also the only HPGe DSSD fabricated with 3 mm strip pitch and a 500 μm gap. The detector is described in more detail in II.C.1. The electronics acquisition system is a first-of-a-kind prototype as well. This low cost, compact, light weight, very low power multi-channel data acquisition system was designed specifically for use with HPGe DSSDs. It employs a new FPGA-based method for lateral position interpolation, and the FPGA firmware is adjustable in software for research use. The electronics are described in more detail in II.C.2.

The UM HPGe detector simulation is the first to use Monte Carlo techniques to demonstrate the detector's response to gap interactions. Individual charge clouds are

drifted in 3D to the detector surface, and the splitting and collection of the carriers within the clouds are modeled. At the surface, lateral electric fields and transport in the a-Ge layers are modeled using three different techniques, and the validity of these techniques is tested by comparison with measured data. The simulation is described in more detail in Chapter III.

The adjustable 2D collimator employed in measurements is first-of-a-kind, allowing for a precise radiation beam spot size for gamma ray energies up to 662 keV. Additionally, custom high activity sources enabled data to be collected using small radiation spot sizes over a reasonable time period. Consequently, the characterization is applicable to gamma rays above 1 MeV, which is especially important for doing Compton imaging.

This work is the first to identify the lateral position and energy dependence of charge loss. Moreover, it is the first to determine a data-based charge loss correction method. This method is effective over a wide range of gamma ray energies, significantly increasing efficiency while reducing unwanted background. The inter-strip interpolation method is first-of-a-kind as well, aimed at improving detector sensitivity by reducing position uncertainty for gap interactions. Furthermore, the position uncertainty of each inter-strip interaction is calculated along with its position, lending itself to better use by advanced imaging reconstruction algorithms.

Altogether, this approach is attractive because it is conducive to doing real-time imaging with any HPGe detector and preamplifier design, as it is not computationally expensive and requires no use of fast signals or associated cross-talk corrections. A fast signal is defined as a transient signal (of zero net charge) adjacent to a strip which

collects charge. Furthermore, the methods should be transferrable to HPGe DSSDs with different gap-to-strip width ratios.

Most importantly, this work looks at a position-sensitive HPGe detector with a unique, first-of-a-kind perspective, motivated by the desire to improve ACT sensitivity by orders of magnitude. Charge loss and surface effects are explored as potentially advantageous. The gap is essentially treated as a very position sensitive strip, i.e., a strip read out by the response of adjacent strips. At low energies (< 100 keV), position resolution is limited mainly by energy resolution. At higher gamma ray energies, charge cloud size is the limit. This new perspective may lead to an improved HPGe DSSD design or potentially to design of a new, more promising position-sensitive detector altogether.

Chapter II

Background

The advent and the state-of-the-art of HPGe detectors and HPGe DSSDs is described. Past work on detector gap characterization, including studies on charge-splitting and charge loss, in similar HPGe DSSDs are also detailed. Next, an overview of the UM detection system is presented, including detector and readout system.

II.A. High-purity germanium detectors

The advent of HPGe detectors is described. The state-of-the-art in fabrication and performance of HPGe position sensitive detectors is reviewed. Additionally, current applications and future directions for HPGe are discussed.

II.A.1. The advent of germanium

Due to their small band gap and good charge collection, germanium (Ge) detectors have excellent energy resolution when operated at liquid nitrogen temperature. The first Ge detector was fabricated via lithium drifting in 1962. With a resolution of 6 keV at 1 MeV, its energy resolution was a factor of 10 better than its NaI predecessor [8]. Yet, its 1 mL volume rendered it only ~1% efficient. By 1970 energy resolution and efficiency had modestly improved, and Ge detectors used in coincidence became a workhorse to

construct complicated nuclear level schemes. The advent of high-purity germanium (HPGe) began in 1971, paving the way for much larger detectors to be fabricated [9]. Since this time, the main advances in HPGe detectors have been due to improved fabrication techniques, including crystallography and segmentation, and advances in mechanical cooling. These improvements have allowed for the use of HPGe detectors for gamma ray imaging, advances in the field of in-beam gamma ray spectroscopy, and improved field detection of radiological materials.

II.A.2. Fabrication techniques

In this section, the fabrication of high-purity germanium detectors is discussed, including crystallography and contact technology for position-sensitive detectors.

II.A.2.1 Crystallography

HPGe fabrication begins with the zone refinement of polycrystalline germanium, which is based on the principle that most germanium impurities concentrate in its liquid phase. In the zone refinement process, hot RF coils move over the polycrystalline ingot, which is kept just above its freezing point, and the liquefied phase moves with coils. The impurities, now at one end of the ingot, freeze, and they are subsequently removed. Next, the zone refined ingot is precisely cut and subjected to the Czochralski technique of crystal growth (See Fig. 1). In a quartz crucible under hydrogen atmosphere, the ingot is dipped into molten germanium then withdrawn slowly. Crystal growth is controlled by temperature adjustment and withdrawal speed. As this technique developed to allow for lower impurity concentrations, larger crystals were fabricated. The HPGe fabrication

process now allows for impurity reduction by a factor of 100, according to Hall effect measurements and photothermal ionization spectroscopy [10]. The largest known HPGe crystal is a 207.6% efficiency P-type coaxial detector, 98 mm in diameter, 110 mm in length, with an active volume of 800 cc [10].

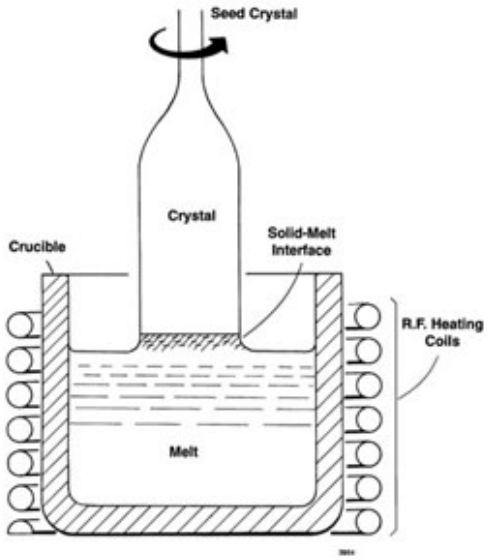

Fig. 1. Illustration of the Czochralski technique of HPGe crystal growth [10].

II.A.2.2 Contact Technology

II.A.2.2.1 Conventional blocking contacts

HPGe detectors are operated as fully depleted detectors, and blocking contacts are required to maintain low leakage currents and high electric fields for charge collection. Traditionally, blocking n-type contacts were formed by lithium diffusion or phosphorous ion implantation, and p-type contacts were formed by boron ion implantation or as metal Schottky barriers. Yet, lithium diffused contacts constitute a dead layer which is several hundred μm thick, and they cannot be used for contacts with fine pitch due to the high mobility of lithium in germanium at room temperature. Phosphorous ion implantation

requires elaborate processing, and it cannot withstand high electric fields. The other conventional technologies also require many processing steps [11].

The finest strip pitch reported for any HPGe detector with conventional blocking contacts is 50 μm pitch on a 5 x 20 mm^2 of a 5 x 5 x 20 mm^3 detector. This was done for a CERN prototype planar detector via photolithography with conventional lithium diffusion and boron ion implantation. However, high detector leakage current in the prototype resulted in excessive electronic noise, creating poor energy resolution [12]. The reason for this poor result was not reported.

II.A.2.2.2 Amorphous germanium contacts

In 1992, Luke et al. reported on sputtered amorphous germanium (a-Ge) contacts which served as both electron and hole blocking contacts. These contacts have thin dead layers, can be fine-pitched, exhibit good blocking behavior for either bias polarity, and the fabrication process is simple [13]. First, a ~0.1-μm thick layer of a-Ge is deposited on the entire detector surface. Then strip electrodes are defined by evaporating a layer of metal through a shadow mask on top of the a-Ge film. The amorphous contacts are also robust. First-generation prototype strip detectors operated successfully for over 5 years with no measurable degradation of the performance. In addition, the contacts have been shown to be stable with temperature up to 100° C for more than 12 hours, which could permit detector annealing for radiation damage repair in ACT if required. Recent design advances have made them even more robust. E. Hull and R.H. Pehl experimentally determined the physics of these contacts, and they used this assessment to increase the contact barrier height to enable detector operation at slightly elevated temperatures [14].

Note that the amorphous germanium technology can just as easily be used to create pixels (vice strips), but this has not been done because pixels are much more expensive to instrument and excessive penetrations to the cryostat are a significant design challenge. Amorphous germanium contact technology has not yet been implemented on coaxial detectors, but efforts to do so are currently underway [15]. The smallest reported pitch for a-Ge contacts with evaporated metallic strips is 200 μm [16].

D. Protic and T. Krings have recently used amorphous germanium technology on a HPGe detector for "microstructured" hole blocking strips with a pitch of 615 μm [16]. There are plasma-etched grooves between the strips which are 60 μm wide and 18 μm deep. Grooved structures are thought to provide better energy resolution because the absence of germanium ($\varepsilon_{Ge} = 16$) in the grooves reduces inter-strip capacitance and dielectric noise. The measured resolution of 0.78 keV FWHM at 60 keV is better than what was achieved with previous designs, at least for low gamma ray energies measured. Yet, the preamplifier FETs in this design are also cooled by LN_2, and the strips themselves have smaller capacitance, so the effect of the groove design alone on energy resolution is not explicitly quantified.

II.A.3. Mechanically cooled performance

Marler and Gelezunas were first to mechanically cool a HPGe detector using the Solvay cycle in 1973. In comparison to LN2 cooled HPGe, energy resolution was degraded 260% at 5.9 keV and 92% at 122 keV [17]. Other early attempts at mechanical cooling also resulted in unacceptable degradation of system performance, and altogether, they were high cost, bulky, unreliable, and required high power inputs [18]. The degradation in energy resolution results from the microphonic noise due to the vibration

of either a moving piston in the cooler's compressor or the boiling of refrigerant gas in proximity to the detector [19]. Reduction of microphonic noise has been subsequently realized through physically separating the detector from the compressor and use of software to digitally filter microphonic noise. Currently, the state-of-the-art is a miniature Stirling cooler in combination with digital filtering. This Stirling cycle cooler uses a dual-opposed piston and springs driven at very high rates to compress the refrigerant gas, helium. The cooling is sufficient for a 50 x 30 mm crystal, it allows for cooling of the preamplifier FET, and it only uses 16 W of power, making battery operation possible. No resolution degradation is detectable above 500 keV, and at energies less than 500 keV, energy resolution is within 10% of that achievable with LN2 cooling [20]. The miniature Stirling cooler has allowed for a commercially available portable HPGe detection system (~10 kg), which is of great interest for homeland security applications [21]. HPGe field detectors will become even more significant in homeland security applications if engineering advances allow reduction in device weight and cost.

II.A.4. Position sensitivity and spectral resolution in segmented HPGe

Planar HPGe detectors are segmented in either pixels or strips. Pixels on a single face allow for the two-dimensional localization of a radiation interaction. Two-dimensional localization with strips requires parallel strips on one face which are orthogonal to those on the opposite face. The size of the pixels or strips should be small enough for adequate position resolution, but large enough so that charge-sharing between segments does not pose a problem. Charge sharing between segments is affected by detector thickness,

charge cloud size, diffusion of the charge cloud, and the magnitude of the lateral electric field. Based upon the detection of a 60 keV gamma ray, R.A. Kroeger determined that the strip pitch should be no smaller than 300 μm in a 10 mm thick planar detector [22].

Traditionally, lateral position resolution was limited to the size of the strip pitch. However, it has been shown that for strip pitches of at least 2 mm, strip interpolation may be done to determine lateral position more finely than the segment pitch. This interpolation is accomplished through pulse shape analysis of the induced signals on neighboring segments. For strip detectors, two methods of strip interpolation have been documented: differential area underneath bystanders [23] and asymmetry position [24].

For planar detectors, depth determination relies upon pulse shape analysis of the signals induced on the collecting electrodes, i.e., the electrodes which collect the electrons and holes from a radiation-induced charge cloud. Knowing the mobilities of electrons and holes in germanium, the interaction depth has been determined as directly proportional to the difference between the 50% time of the electrons and holes, where the 50% time is defined as the time at which the collecting electrode pulse reaches half its final height. Depth determination can be done in either of the following ways: 1) collecting electrode signals are digitized, then software is used to determine the 50% time and the depth of interaction [13]; or 2) analog electronics, such as constant fraction discriminators or leading edge discriminators, are used to determine the 50% time [24].

Nearly all coaxial HPGe detectors are segmented on the external contact only. The external contact is pixilated both radially and longitudinally; for example, in TIGRE (Track the Interaction of Gamma Ray Events), a 24-segment detector is formed by segmenting a 6.5 cm diameter and 8 cm long HPGe crystal into six segments radially and

four segments longitudinally. For each interaction that occurs, one collecting electrode signal and eight bystander signals must be analyzed in order to localize position in 3D. For TIGRE, the average FWHM energy resolution at 1.3 MeV of the 24 segments was 2.3 keV [25].

For coaxial or planar detectors, position and spectral resolution improve as noise decreases. This noise is mainly dependent on the detector capacitance and the noise associated with the preamplifier FETs, which can be further lowered by designs allowing for the FETs to be cooled within the cryostat. In a 36-fold coaxial detector with cooled preamplifiers, energy resolution changed from an average of 1.14 and 1.93 keV at 60 and 1332 keV immediately after powering preamplifiers on to an average of 1.41 and 2.15 keV at 60 and 1332 keV after preamplifiers had been left on for a day. This degradation in energy resolution occurred because the cryostat was not able to provide sufficient cooling power to all 36 preamplifiers [26].

II.A.5. Gamma ray imaging with planar HPGe

Compton imaging can be accomplished using a single HPGe detector or an array of these detectors. In the single detector case, a minimum of two interactions are required, where all of the gamma energy is deposited in these two interactions. If the interaction positions and energies are known, a gamma ray image can be reconstructed. Of course, when strip interpolation is used, these interactions must be separated by distances larger than a strip pitch. For a planar 11 mm thick detector with 2 mm pitch, where strip interpolation was used to improve lateral position resolution, only interactions separated by 8 mm or more in each lateral dimension were able to be used [23]. Yet, Mihailescu et

al. have recently shown that detector imaging efficiency is greatly improved when charge shared and multiple events are accounted for via pulse shape spectroscopy and probabilistic methods; imaging efficiency was improved by a factor of three for a planar germanium detector in coincidence with a planar silicon detector [27].

When Compton imaging is done with a stack of planar detectors, intrinsic efficiency is improved and a greater fraction of events can be used in reconstruction, also improving efficiency. When source energy is unknown and only partial energy deposition occurs, only three interaction positions and energies must be known [28]. For any technique, the interaction order must be correctly sequenced. Based upon probability, the list-mode maximum likelihood image reconstruction algorithm most efficiently determines the interaction order, and then reconstructs the image.

The best reported energy resolution for a single planar HPGe detector is 0.47 keV at 60 keV and 0.66 keV at 667 keV. This experimental result was obtained by Lawrence Berkeley National Lab's (LBNL) Nuclear Compton Telescope group. This group also achieved a typical depth resolution of 0.18 mm in a 15 mm thick detector (~0.4 mm FWHM) with analog electronics, including the use of a constant fraction discriminator [1]. Other groups reported a best depth resolution at 0.5 mm FWHM. All groups have difficulties doing depth interpolation when interactions occur within 0.5 mm of the electrodes due to electric field irregularities near the detector surface.

The best lateral position resolution for a planar detector was obtained by the LLNL group through use of interpolation for in-strip interactions. For a 2 mm pitch detector, the lateral position resolution is 0.5 mm at 122 keV. This position resolution tends to improve with gamma energy, because the signal-to-noise ratio improves with energy.

Yet, this lateral position resolution is not constant as a function of depth, as shown by groups at Lawrence Livermore National Lab (LLNL) and Naval Research Laboratory (NRL). LLNL reported that at gamma ray energy of 200 keV, the lateral position resolution is 0.25 mm when the depth in a 11 mm thick detector is greater than 5 mm. Between 2-3 mm depth, the lateral position resolution is comparable to the strip thickness of 1.5 mm [23]. This degradation in lateral position resolution is a result of bipolar induced charge signals on bystander electrodes at this depth. Despite the difficulties with strip interpolation, one group has shown it to make a significant difference in imaging results. When imaging the 511 keV peak of a Na-22 point source with a single detector, the LLNL group showed that the point spread function improves from 25° to 10° with strip interpolation, as seen below in Fig. 2(a) and Fig. 2 (b) [23].

(a) 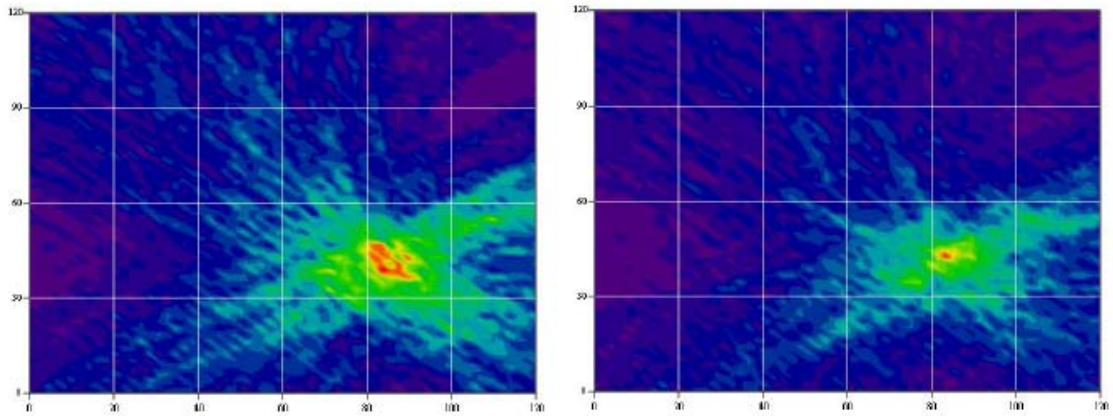 (b)

Fig. 2. (a) Compton image from a 511 keV point source with point spread function FWHM of 25°. A single 11 mm thick double-sided strip detector with 2 mm pitch was used. (b) Image from same data set as in (a), except using strip interpolation. FWHM of the point spread function is improved to 10°. [23]

II.A.6. Principal Applications

This section discusses the principal applications of position-sensitive HPGe detectors for gamma-ray astronomy and high energy physics.

II.A.6.1 Gamma-ray astronomy

Germanium detectors have long been used in gamma ray astronomy because they are able to cover the entire hard X-ray to gamma-ray line energy range with the highest achievable spectral resolution. They have been flown on HEAO-3, Mars Observer, and Wind spacecraft. Segmented germanium detectors have been flown on HEXAGONE, HIREGS, and other balloon payloads. Most recently, the Reuven Ramaty High Energy Solar Spectroscopic Imager (RHESSI) satellite was launched into orbit in 2002 [29]. It consists of nine coaxial HPGe detectors, 7 cm diameter by 8.5 cm long, each one having its inner contact segmented 1 cm from the detector front surface. This effectively creates nine 1 cm thick detectors to stop photons between energies of 3-150 keV and nine 7.5 cm thick detectors to stop photons with energies 150 keV – 20 MeV. If the instrument is oriented toward a gamma ray line flare, the intense 3-150 keV X-ray fluxes that accompany a large gamma-ray line flare are absorbed by the front segment, allowing the rear segment to count at moderate rates [30].

II.A.6.2 Nuclear and high energy physics

First generation high energy resolution arrays for in-beam gamma ray spectroscopy were constructed in the beginning of the 1980s in order to better understand nuclear structure. Following high energy bombardment of heavy ions onto a target, the nuclei

recoil at high velocity while decaying via gamma ray emission. Consequently, gamma ray energy lines are Doppler shifted. These unwanted Doppler broadening effects are reduced by decreasing the acceptance angle of gamma rays and by more closely resolving the interaction position of gammas via segmentation [31].

HERA (high energy resolution array) was the first HPGe array for in-beam gamma ray spectroscopy, consisting of twenty-one 25% efficient coaxial Ge detectors. Each detector was Compton suppressed by a BGO detector to improve the peak-to-total ratio [32]. Since then, energy resolution, efficiency, high photopeak efficiency, fine position resolution through high granularity or pulse shape analysis, stable operation, and long life have driven further evolution. Many of these factors contribute to the resolving power of an array, defined as the ability to isolate a given sequence of gamma rays from a complex spectrum (e.g. from nuclear fusion reactions) [33].

To increase efficiency, clover and cluster arrays were introduced, each array housed inside its own cryostat. The clover array is a composite of four coaxial Ge detector elements whose side surfaces have been cut to fit together. In this array, the energy of scatter between crystals could now be added back, increasing efficiency by 50% in comparison to individual crystals. Clover arrays were used in CLARION (ORNL), EXOGAM (Gamil, France), and TIGRESS (TRIUF-ISAC) [31]. A cluster is an array of 7 closely packed coaxial Ge detectors, each detector encapsulated, all surrounded by BGO. EUROBALL consists of 15 cluster arrays, 24 clover arrays, and 30 individual escape-suppressed Ge detectors. Gammasphere, the largest existing high energy resolution array, consists of 110 individually escape suppressed Ge detectors, 80 of which have two-fold segmentation of outer electrode to reduce Doppler broadening. At the time

Gammasphere was built, it was able to take advantage of larger available detectors (75% efficiency). Like HERA, EUROBALL and Gammasphere use BGO scintillators to reduce Compton background, in this case by rejecting gamma rays that Compton scatter outside a clover / cluster volume (see Fig. 3). The solid angle covered by Gammasphere and its immediate predecessors arrays is approximately 2π.

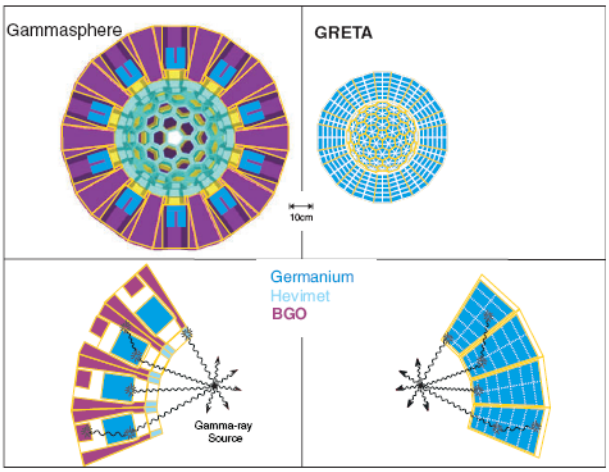

Fig. 3. Gammasphere array compared with proposed GRETA array. While Gammasphere suppresses Compton events which occur outside of a clover/cluster volume, GRETA tracks all events. [32]

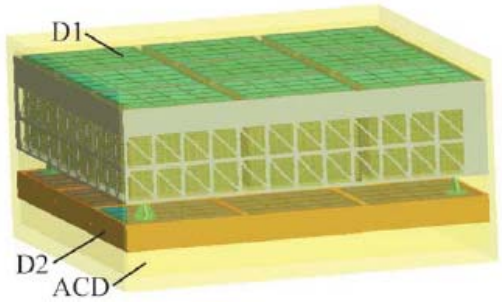

Fig. 4. The initial baseline concept of the Advanced Compton Telescope. After optimization, D1 consists of 27 layers of 2-mm thick Si detectors and D2 consists of 4 layers of 16-mm thick HPGe detectors. All layers are surrounded by BGO for anticoincidence (ACD). [1]

II.A.7. Future directions for HPGe

New applications driven by physics questions have always driven new HPGe detector designs, and new technologies have made the new designs possible. Currently, the main applications driving development are the gamma-ray astronomy community's Advanced Compton Telescope (ACT) concept and the high energy physics community's GRETA (gamma-ray energy tracking array) concept. As previously mentioned, both NRL and LBNL investigated use of segmented planar HPGe for NASA's ACT, and LBNL decided to use this detector as the base for its ACT proposal [1]. Out of 6 proposals, LBNL's proposal achieved the best narrow line sensitivities, 847 keV broad-line sensitivity, and energy resolution. It also has one of the largest fields-of-view. For these reasons, HPGe detectors have been selected as part of the initial baseline concept for ACT, as pictured in Fig. 4. The initial baseline concept consists of four layers of 16-mm thick Ge cross-strip detectors, each layer having 144 detectors, each detector 9.2 x 9.2 cm^2 in area. To reduce complexity, strips with pitch of 1 mm would be used instead of using a larger strip pitch along with strip interpolation. It is likely that a Turbo-Brayton cooler [34] would be used to cool the germanium array. This cryrocooler is currently used on a smaller scale in another NASA spacecraft, and it offers the advantage of essentially no vibration, which means that it does not degrade the excellent germanium energy resolution [1].

The high energy physics community's proposed GRETA allows for 4π gamma ray tracking. The array, shown in Fig. 3, is proposed to consist of 120-130 36-fold segmented HPGe closed-end coaxial (8 cm diameter by 9 cm long) detectors. The GRETA promises to dramatically increase efficiency and resolving power by fully utilizing Compton scattered events instead of rejecting them [33]. The resolving power is

predicted to be three orders of magnitude greater than EUROBALL and Gammasphere. The efficiency for a 10 MeV gamma ray will 20 times that of Gammasphere. Gamma ray tracking in GRETA will also allow for Doppler broadening to be reduced by as much as 10 times that capable with a Gammasphere detector [32].

II.B. Detector gap characterization of similar detectors

This section gives additional background on some of the complications inherent to detector gaps, which were outlined in I.C.2, and the approaches used by others to work around these complications. Relevant measurement and simulation results are reviewed for HPGe strip detectors with different types of contact technology, as discussed in Section A.2.2.

II.B.1. HPGe strip detectors with microstructured contacts

In Section B.1.1, past work on detector characterization is described for HPGe microstructured detectors designed before the implementation of a-Ge technology. Section B.1.2 describes characterization work after its implementation.

II.B.1.1 Charge-splitting and charge loss in HPGe microstrip detectors

Rossi et al. [35] quantified charge-splitting and charge loss in two HPGe microstrip detectors at X-ray energies from 15 to 100 keV. These 200 μm strip pitch detectors [36], designed by D. Protic, employed conventional contact fabrication technology on microstructured strips. Interactions in gaps were shown to cause charge-splitting, which seriously degraded detector performance. Yet, reconstruction of events with an energy-

sum coincidence algorithm produced artifact-free spectra with energy resolution < 2 keV, high photopeak counts, and excellent count uniformity.

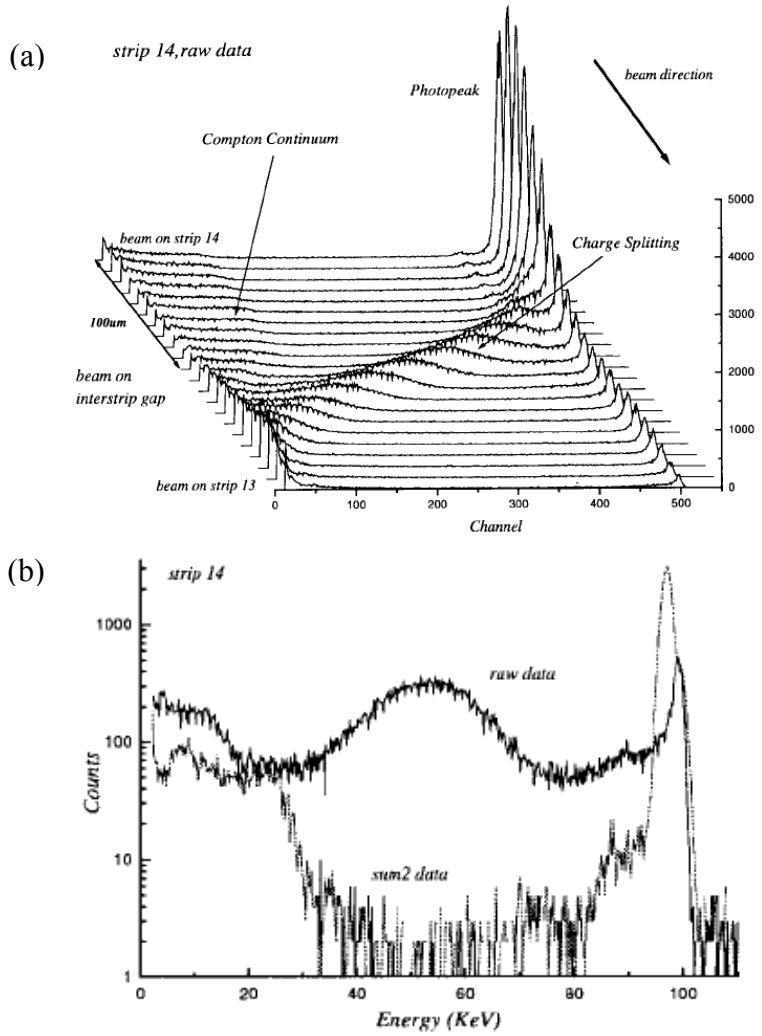

Fig. 5. (a) Energy spectra on strip 14 for a 100 keV X-ray beam with 10 μm FWHM stepped in 10 μm increments from the strip center of strip 14 to the strip center of strip 13. (b) Energy spectra on strip 14 (raw data) and from the summation of the signals on strips 13 and 14 (sum2 data) at the gap center. [35]

Charge-splitting in a detector with 50 μm gap and 150 μm strip width is shown in Fig. 5(a). The energy spectra on strip 14 are shown for a 100 keV X-ray beam (with 10 μm FWHM) stepped in 10 μm increments from the strip center of strip 14 to the strip center of strip 13. As strip 13 is approached, charge-splitting causes increased low energy

tailing and reduction in photopeak counts. A Compton continuum is present as well due to the 22% likelihood of Compton scattering at 100 keV. Fig. 5(b) shows energy spectra on strip 14 (raw data) and from the summation of the signals on strips 13 and 14 (sum2 data) at the gap center. For the spectrum on strip 14, the bump centered at ~50 keV is due to charge-splitting. When spectra are summed together, the split charge is summed as well, resulting in the shift of the bump into the photopeak. Charge loss was measured for each detector at 15 keV, where the X-ray absorption length is ≈20 μm, with a 15 keV source collimated to the gap center. A charge deficit of 4% was found for the detector with 35 μm gap size, and a deficit of 10% was found for the detector with 50 μm gap size. These deficits were attributed to charge trapping of carriers from interactions near the detector surface where electric field was weak.

II.B.1.2 Charge loss in HPGe strip detectors with microstructured a-Ge contacts

D. Protic recently fabricated HPGe detectors with microstructured a-Ge contacts. Contact fabrication was described in II.A.2.2.2. Detector depletion voltage was -1000 V. The detector was irradiated with uncollimated Cs-137, Am-241, and Cm-244 sources. These sources yield the following radiation, respectively: 662 keV γ, 59.5 keV γ, and 5.8 MeV α. Energies of events that triggered coincidently on adjacent strips were recorded. At an operating voltage of -1500 V, practically no charge loss was measured for 662 keV and 59.5 keV γ's. However, no coincidences were detected for the 5.8 MeV α, which has a range of about 23 μm (compare to 50 μm gap width). Instead, a single strip collected at most half the charge, and negative pulses were occasionally detected in coincidence on the adjacent strip. While the origin of the negative pulses was unexplained, the results

suggest that charge loss for carrier-clouds whose dimensions are smaller than that of the gap size may be to blame. [5]

II.B.2. HPGe strip detectors with a-Ge contacts

In Section B.2, past work on detector characterization is described for HPGe detectors designed using a-Ge contact technology. These detectors were fabricated using the technique pioneered by P.N. Luke, as discussed in II.A.2.2.2. Section B.2.1 describes an approach taken to address the complications of charge-sharing and multiple close interactions. Section B.2.2 describes past characterization of charge loss and approaches recommended to address this problem.

II.B.2.1. Charge-sharing and multiple close interactions

Charge-splitting, also known as charge-sharing, in HPGe strip detectors has been identified by others. In a recent study [27], which will be described in some detail here, it was found that the initial extent and diffusion of charge-carrier clouds inside the semiconductor detectors profoundly affect the fraction of interactions that deposit charge in adjacent electrodes. Consequently, the identification of charge-shared interactions was found to be a key factor in correctly reconstructing the position of interactions in the detector. In this work, charge-sharing was defined as the process by which charge-carriers produced by a single interaction are collected by two adjacent strips (see Fig. 6). It was argued that multiple interactions within the bounds of two adjacent strips may produce signals similar to those produced by charge-shared events, but the two were distinguishable based upon rise time characteristics.

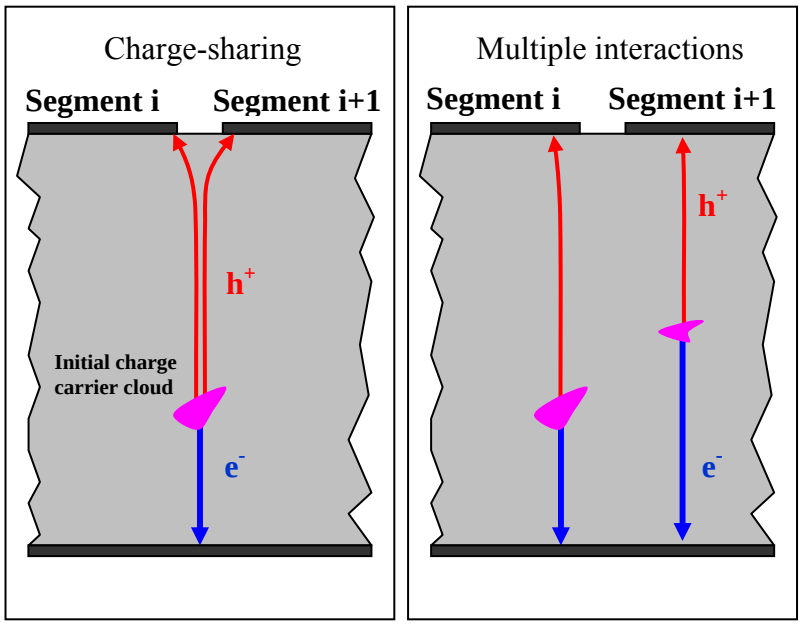

Fig. 6. Comparative representation of a single charge-shared interaction and a double interaction event [27].

Two software-based gap tests for charge-shared events were developed, one for interactions close to a collecting electrode and the other for interactions further away. In each case, a Chi-squared test was used to determine whether adjacent signals were similar enough during a fixed period of the rise. For a single interaction very close to collecting electrodes, carriers traverse a high gradient in weighting potential immediately, so the time period of comparison here was set toward the end of the rise.

Benchmarking measurements were taken on an HPGe DSSD with strip pitch of 2 mm, gap size of 500 μm, and thickness 11 mm. The strip center or the gap center (with respect to both detector sides) were irradiated with a Cs-137 source through 1 mm diameter pinhole. Monte Carlo simulation of the experiment predicted a 7% increase in charge-sharing when moving from strip center to gap center. Initial experimental results showed a factor of two increase. Use of the gap tests on experimental data showed a 20% increase in charge-sharing. Inclusion of these identified charge-shared events in

reconstruction contributed to a significant increase in efficiency for the hybrid Si-Ge Compton imager under development [27].

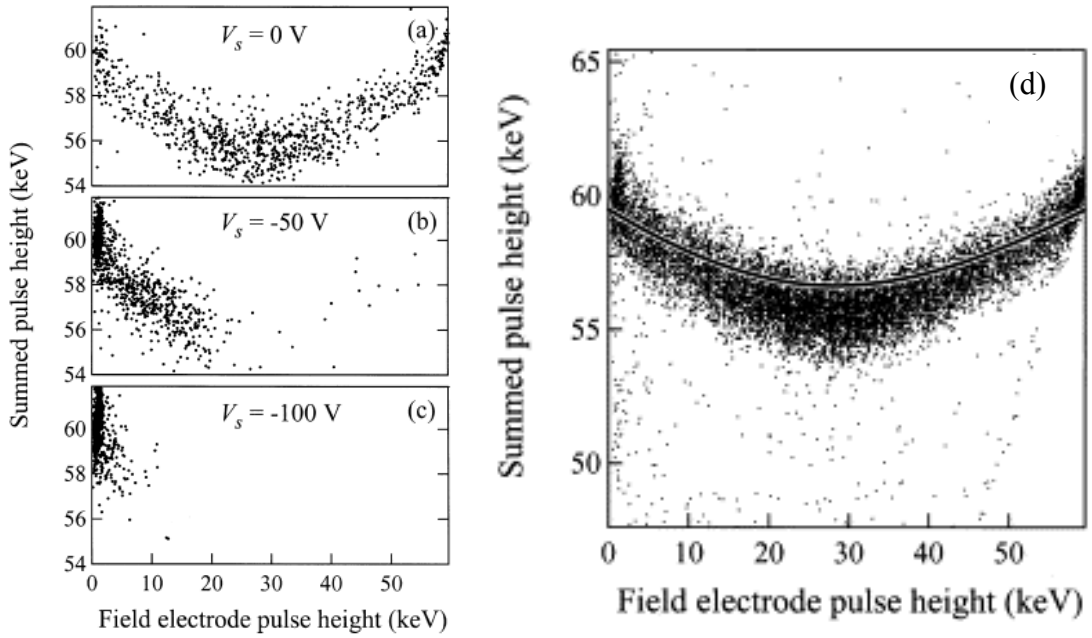

Fig. 7. An HPGe DSSD was irradiated with a 60 keV source. Scatter plots of summed pulse height from adjacent strips are plotted against the pulse height from one of the strips. In (a), no bias is applied in between the two strips. In (b) and (c), biases of -50 and -100 V are applied, respectively, resulting in reduced charge loss. The line across the data in (d) shows the simulated result. [13]

II.B.2.2. Charge loss in HPGe strip detectors with a-Ge contacts

Charge loss in HPGe strip detectors with a-Ge contact technology has been identified by others. Amman and Luke [13] characterized charge loss through simulation and measurement in a HPGe strip detector with a 500 μm gap. Fig. 7(a) is a scatter plot of the sum of adjacent strips versus the energy of one strip upon 60 keV irradiation. This distribution is parabolic in shape with a maximum of ~ 6% loss. Note that maximum charge loss is expected when the signal on a single strip is ~30 keV out of 60 keV. Fig. 7(b) and Fig. 7(c) demonstrate reduction in charge loss through biasing a field shaping strip in between two collecting strips with a potential of opposite sign, forcing charge

collection by the collecting strips. Introducing this opposite bias on field shaping strips on each side of a collecting strip resulted in improved photopeak efficiency, reduction in background, and minor improvement in energy resolution at 60 keV, as shown in Fig. 8, and at 662 keV. Although this technique degraded the position resolution of the detector by forcing all charge-carriers to collecting strip(s), it suggested that smaller inter-strip field shaping electrodes may be able to achieve similar benefits while preserving position resolution. Furthermore, the charge loss simulation shown in Fig. 7(d) was used as a starting point for the UM HPGe detector simulation of charge loss, as discussed in III.B.2.5.

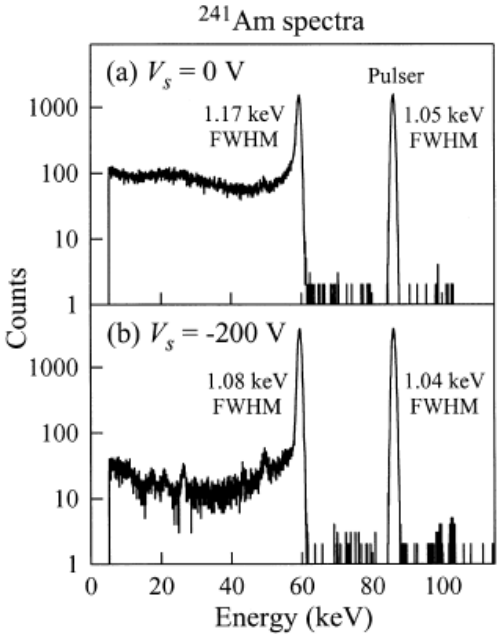

Fig. 8. Energy spectra on a single strip before (a) and after (b) reverse bias of -200 V is applied on two adjacent field shaping strips. [13]

Coburn et al. [37] studied charge loss on cathode and anode sides by measuring pulse heights of coincident signals on nearest neighbor strips. Their detector was uniformly irradiated by gamma rays with varying energies. At 60 and 122 keV, nearest neighbor

coincidences were found to constitute about 15% of all events, where 25% was expected based upon the gap-to-strip width ratio. Charge loss was measured as the photopeak shift of those pulses with nearest neighbor coincidences. At 60 keV, they found ~6% loss in the photopeak channel number on the anode side and ~1% loss on the cathode side of their detector. But at 662 keV, the photopeak shift was much less significant on the anode side. Since the fractional charge loss was lessened for carriers formed deeper in the detector, they concluded that there was a dead region of high charge loss near the anode surface. Furthermore, they suggested that: 1) a correction be made based upon the charge collected by all relevant cathode and anode strips based upon depth interpolation, and 2) the gap-to-strip width ratio be minimized to reduce the percentage of nearest neighbor events.

Based upon numerical simulation, Amrose et al. [38] suggested that incomplete charge collection may result from surface conductivities actually higher than that which was measured in the amorphous layer of their HPGe DSSD. The measured conductivities of their detector were $10^{-16}\Omega^{-1}$ at the surface and $10^{-12}\Omega^{-1}cm^{-1}$ in the bulk. But they showed that if the surface conductivity were increased by a factor of 100, the field in the gap would be barely distinguished from the field along the strips, causing charge to become stuck in the gap. Fig. 9(a) shows the simulated electric field on the detector for the measured conductivity. Fig. 9(b) shows the simulated field after the surface conductivity is increased by a factor of 100.

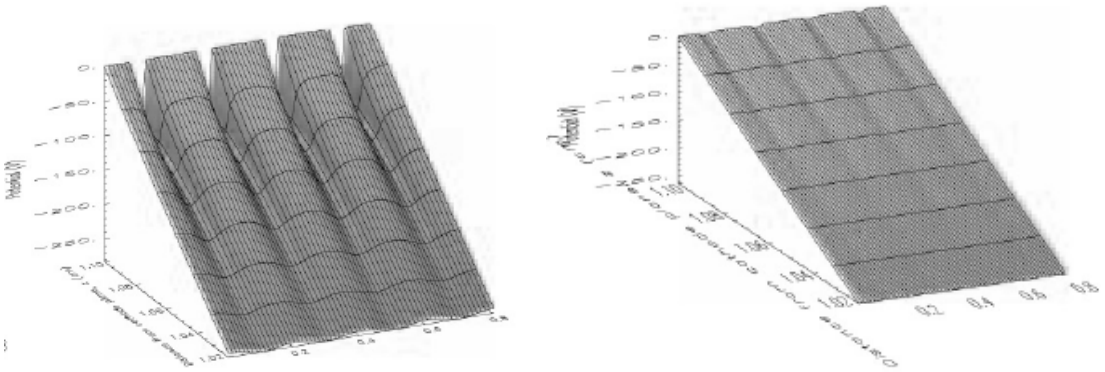

Fig. 9. Simulated electric field for measured surface conductivity (a) and when surface conductivity is increased by a factor of 100 (b). [38]

In a paper published during 2007 [6], Amman and Luke proposed a few unique ways to address the challenges that charge loss introduces. First, the amorphous layer could be optimized so that charge accumulation inhibits the collection of signal charges at the inter-contact surface. Second, the a-Ge layer could be etched away in between strips. Third, the area of inter-contact surfaces could be minimized at the cost of increased electronic noise. Lastly, as proposed in [37], it was suggested that charge loss corrections could be implemented in the signal processing step.

II.C. Detection system description

In this section, the UM HPGe double-side strip detection system, first mentioned in I.C.2, is described in more detail, including the detector itself (in Section C.1) and its electronic acquisition system (in Section C.2).

II.C.1. The UM HPGe DSSD

The UM double-sided strip detector was fabricated by Ethan Hull and Dick Pehl at PHDs Co [3]. The detector, pictured inside its cryostat in Fig. 10, is 11.2 mm thick, 81.3

mm in diameter, and its strips are fabricated with amorphous-Ge contact technology. The 23 × 23 orthogonal strips have a pitch of 3 mm, and the gap in between strips is 500 μm; so the gap-to-strip width ratio is 1/6. The active part of the crystal is surrounded by a guard ring.

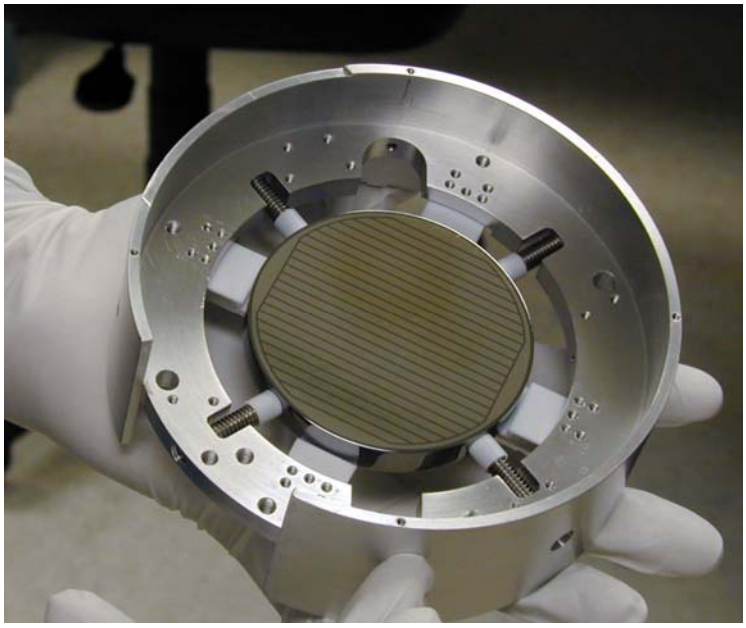

Fig. 10. Photograph of the UM DSSD positioned inside its cryostat. See text for fabrication details. [3]

The detector employs a p-type crystal with reported impurity concentration of ~$4.5 \times 10^{9} cm^{-3}$. The capacitance between strips is 27 pF, and preamplifier JFET input capacitance is 10 pF. The detector is fully depleted at -320 V, depleting from the anode side to the cathode side. The cathode side is also referred to as the AC side, while the anode is called the DC side, referring to the type of coupling connecting each strip of the crystal to its associated preamplifier. The cathode side is AC coupled because it is connected to high voltage.

The detector is biased to -700 V on the cathode side, and it is operated at a temperature of 92 K. It has a low energy threshold of ~ 40 keV due to its aluminum

housing. The unique features of this detector include a new cryostat design, proprietary contact technology that better survives temperature cycling, and low noise preamplifiers redesigned to minimize crosstalk. Energy resolution on a single strip was measured to range from 1-2 keV at 60 keV and 2-3 keV at 662 keV.

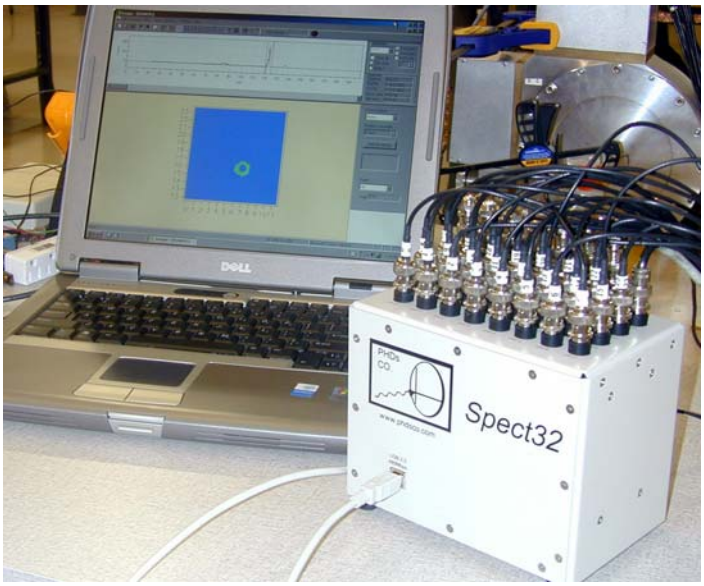

Fig. 11. Photograph of the Spect32 gamma ray spectroscopy system. In front, the 32 channel readout box is connected to a laptop via a single USB cable. In back, each channel of a fully instrumented 32 channel HPGe DSSD is connected to the readout box. [3]

II.C.2. Electronic acquisition system

The UM detector is instrumented by a developmental 32 channel readout system called Spect32, designed by PhDs Co. [3] and pictured in Fig. 11. The Spect32 is designed to output the data required to do real-time imaging with an HPGe DSSD. It has dimensions of 11 × 15.5 × 14.5 cm, and is powered by a 12V supply, only drawing 18W of power. It consists of four electronics boards, each with eight BNC inputs, eight 12-bit 50 MHz ADCs, and an Alterra Cyclone field programmable gate array (FPGA) for data processing. The FPGAs operate off of a global 50MHz clock, which corresponds to a

time of 20 ns per clock tick. A fast filter both controls triggering and determines the 50% constant fraction rise times of each triggered signal with precision ±10 ns.

Each FPGA implements fast and slow trapezoidal filters. Spect32 software allows for the adjustment of FPGA firmware settings for these filters, including signal input polarity, rise time, and flat top time. A peak-to-peak measurement of the shaped fast signal is recorded for use in lateral position interpolation for in-strip interactions. An amplitude measurement of the shaped slow signal is recorded for energy determination. Precision energy determination is aided by baseline restoration and pole zero correction features.

A separate FPGA functions as the motherboard, communicating with each of the aforementioned eight channel boards to set up a single USB 2.0 data output stream. For a trigger on any channel, the slow and fast filter measurements from each instrumented channel are passed to this output stream. Spect32 software was employed to write the output steam to a data file for offline processing. A SPARC workstation was used to further reduce the data for analysis in MATLAB, as data reduction is essential. For a single measurement described in Chapter IV, the Spect32 system digitizes ~ terabytes of data, but outputs only gigabytes of data (in ASCII form). The SPARC workstation was used to reduce these gigabytes to kilobytes, keeping only what was essential for analysis.

Chapter III

HPGe detector simulation

First, GEANT4 charge cloud simulations in germanium are described. Next, the implementation of the UM HPGe detector code is discussed. Finally, the code is used to predict detector charge-splitting and charge loss response using three surface modeling techniques.

III.A. Charge cloud simulations in germanium

In this section, the GEANT4 simulation package [39] is described, and simulation results of charge-carrier clouds in germanium are presented. As mentioned in I.C.II, charge cloud statistics are significant to detector gap response, so this discussion is relevant to the UM HPGe detector code to be described in III.B.

III.A.1. GEANT4 package

The GEANT4 (v. 4.6.1) low energy package was used to simulate charge clouds produced by energetic electrons in germanium. The package used was set up by the astrophysics group at Naval Research Laboratory to model the Advanced Compton Telescope designs they are working on. This group extensively tested the physics before

modeling was commenced. The package was conveniently setup to run on Microsoft Visual C++ 6.0 loaded onto a Windows workstation.

III.A.2. GEANT4 physics discussion

Simulated physics interactions for electrons include ionization, bremsstrahlung, and multiple scattering. The low energy package has shown to be consistent with experimental data down to 250 eV, and it includes data libraries down to 10 eV. Databases used to sample cross sections and obtain a particle's final state include the Evaluated Atomic Data Library, the Evaluated Electrons Data Library, and the Evaluated Photons Data Library. The range and stopping power of electrons in germanium was shown to be the same for all GEANT4 models, and it was consistent with NIST-ESTAR reference data (p-value of 1) [40].

The most important process in modeling an electron's energy deposition is multiple Coulomb scattering. GEANT3 and EGSnrc uses a condensed history simulation based upon Moliere theory. This simulates the global effects of collisions during a macroscopic step, but uses approximations. Angular deflection is sampled from Moliere distribution and approximate path length correction computed. GEANT4 uses a new multiple scattering model by L. Urban which does not use the Moliere formalism. This model samples the angular deflection from a semi-empirical formula, it converts the longitudinal displacement to "true" path length, and it performs a lateral displacement as well. It was determined that this implementation in GEANT4 had a step size dependence to it. This step size dependence was found to decrease with decreasing step size. Consequently, the

step size chosen for the analysis was 1 μm. Further reduction in step size resulted in increased computation time with no change in results.

III.A.3. Charge-carrier cloud statistics in germanium

According to GEANT, a charge-carrier cloud is formed in ~ 1 ps. Fig. 12 shows a 2D projection of energy deposition for 500 electrons at 400 keV in germanium. Each electron was shot from (0,0) along the + y axis. Energy deposition in units of keV was scored in 10 μm voxels, then summed along the z axis. Fig. 13. shows a 2D projection in the plane orthogonal to the one shown in Fig. 12. In this case, energy deposition was summed along the y axis. Together, the figures show the extent of an average charge-carrier cloud at 400 keV. The pixels in each projection are color coded by total energy deposition over 500 histories. The percentages beside the colorbar give the percentage of the total of 500 × 400 keV = 200,000 keV deposited in a pixel. In Fig. 12, the gap size of our detector is shown for perspective.

On average, a 400 keV electron deposits the greatest fraction of its energy along its initial direction of motion (±5 μm), yet the path of an electron is so tortuous that this fraction is a small fraction (< 5%) of the 400 keV. The straight line distance traveled by an electron ranges from about 300-500 μm, and energy is lost at a higher rate along the latter half of its path. This is consistent with theory, which suggests that multiple changes in an electron's direction during the slowing down process smear out its Bragg peak.

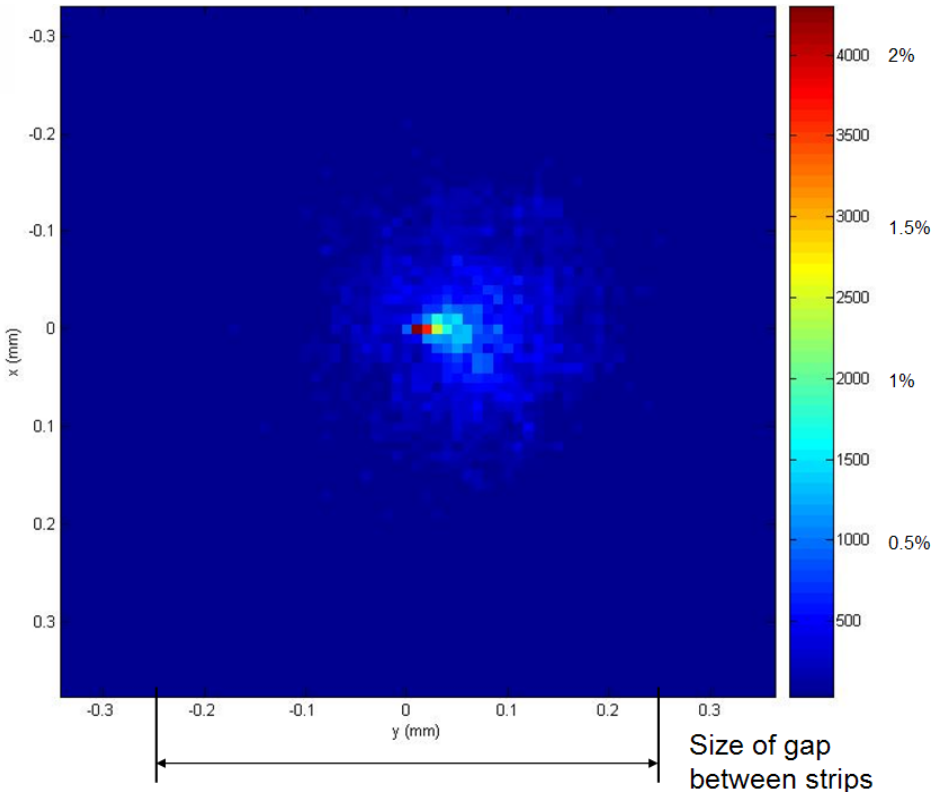

Fig. 12. xy projection of energy deposition for 500 electrons at 400 keV in germanium. Electrons are oriented along the +y axis.

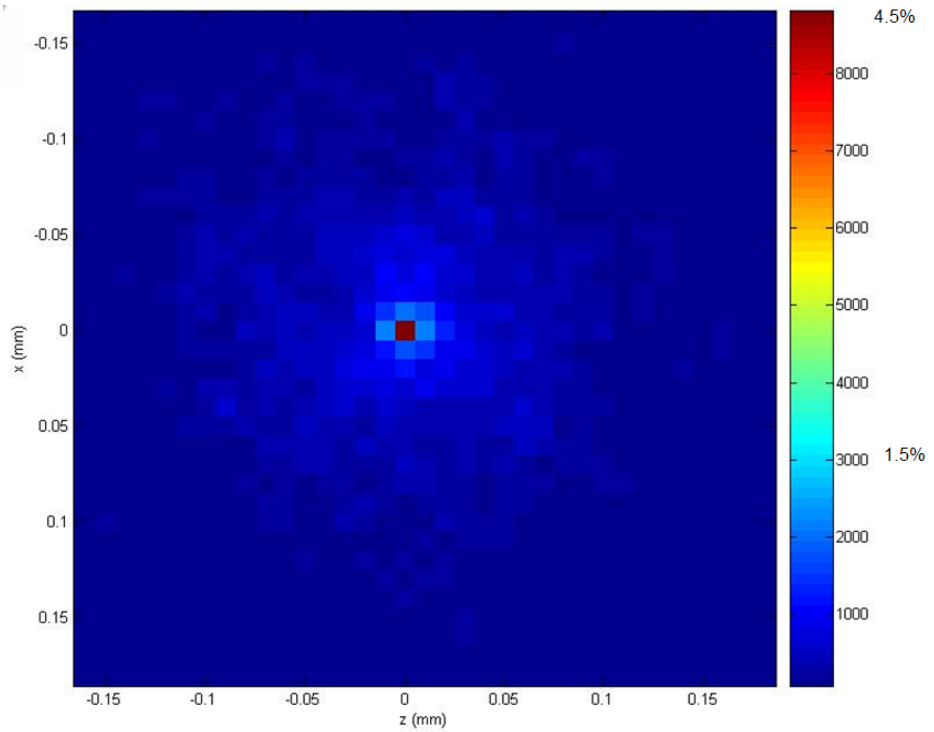

Fig. 13. xz projection of energy deposition for 500 electrons at 400 keV in germanium.

To quantify the extent of the charge-carrier cloud as a function of gamma ray energy, the distance along the y axis that electrons traveled until they first exited a cone was determined. A right cone directed along the +y axis with an opening angle of 90° was chosen, and 10,000 histories were run at energies 200, 400, 800, and 1200 keV.

(a) (b)

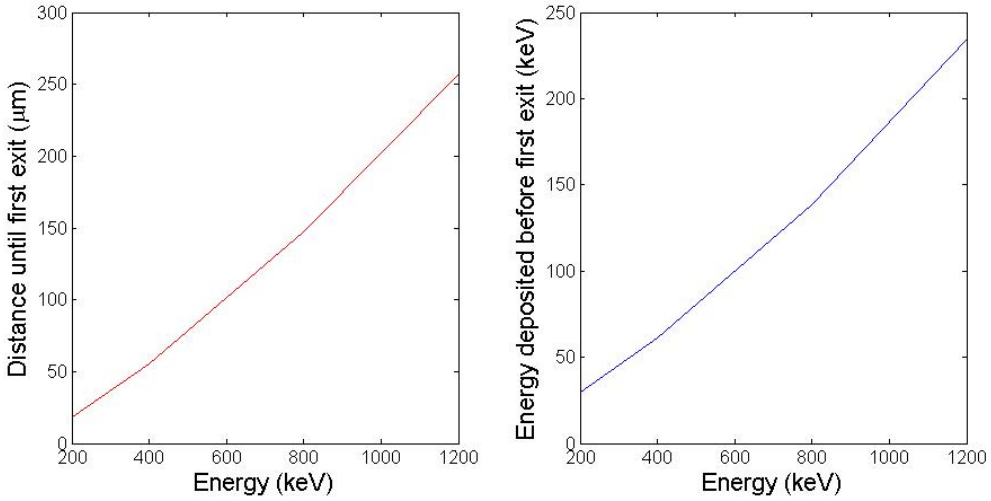

Fig. 14. (a) Mean distance until an electron first exits a right cone with opening angle 90° oriented along its initial direction. (b) The mean energy an electron deposits before first exiting the cone.

The mean distance until the electron first exits the cone is plotted in Fig. 14(a). This shows that the extent of the charge cloud is expected to increase nearly linearly with energy on average. As shown in Fig. 14(b), the mean fraction of energy deposited before first exit increases with energy as well. Thus, the fraction of energy deposited on average in the cone remains nearly constant at 15-20%. Yet, a single history can deviate significantly from average behavior. Thus, for any detector region sensitive to charge cloud extent, such as the detector gap, it is most appropriate to consider detector response on an event-by-event basis.

III.B. Detector simulation for interactions in the gap between strips

The UM HPGe detector code, first mentioned in I.D, is described in further detail in this section. This code models detector response through the drifting of individual charge clouds in 3D. The modeling of surface electric fields, which appear to significantly affect charge loss for gap interactions, is discussed as well.

III.B.1. Charge clouds for gap simulation

As mentioned in I.C.1, HPGe strip detector gaps are sensitive to the size and orientation of charge-carrier clouds. Since gap interaction measurements are performed using collimated Ba-133 and Cs-137 sources, GEANT4 was used to determine energy deposition positions in germanium for photoelectrons with 356 keV (Ba-133) and 662 keV (Cs-137). The 3D interaction positions and the energy deposited at these positions were used as the input for the UM HPGe detector code. The code converts energy deposition into electron-hole pairs (ehp) using the conversion efficiency ω of 2.96 eV/ehp in germanium, forming charge-carrier clouds for drifting. Depending upon the energy deposited at given location, a drifted element may actually be composed of multiple carriers. The initial direction of each photoelectron is randomly selected for Monte Carlo simulation. Noise from statistical fluctuations in carrier generation is not included, as its standard deviation $\sqrt{F\omega E}$ is less than 0.5 keV at $E = 662$ keV (Fano factor $F = 0.12$).

III.B.2. Calculation of induced signals

Induced signals for the drifting of a single electron and a single hole are calculated as described in LBNL's 3D GRETA code [41], but modified for our detector geometry. The UM HPGe detector code models the drifting of charge clouds through a superposition of the signals induced by all carriers in a charge cloud.

The signal induced by a single charge-carrier was calculated in $t_{step} = 1\,ns$ steps using Eqn. 1. Thus, the charge Q_i induced at a time *t* by a carrier *i* with charge q_i is given by

$$Q_i(t) = \sum_{j=0}^{t} -q_i \varphi_o(\vec{r}_i(j)) \tag{2}$$

where $\vec{r}_i(j)$ is the position of carrier i at time step j and $t \le t_{f,i}$, the time the carrier *i* reaches the detector surface, as discussed in Section B.2.5. The net charge Q_{net} induced at a time *t* by all carriers in a charge cloud is given by

$$\begin{aligned} Q_{net}(t) &= \sum_{j=0}^{t_i} \sum_{i=1}^{N_i} -q_i \varphi_o(\vec{r}_i(j)) \\ where\ t_i &= t \quad for\ t \le t_{f,i} \\ or\ t_i &= t_{f,i} \quad for\ t > t_{f,i} \end{aligned} \tag{3}$$

because carriers are assumed not to continue to induce charge once they reach the detector surface. This method requires inputs of weighting potential $\varphi_o(\vec{r})$ and charge-carrier velocities $\vec{v}_e(\vec{r})$ and $\vec{v}_h(\vec{r})$ at all positions $\vec{r}$ in the detector. These calculations are discussed next.

III.B.2.1. Weighting potential calculation

Weighting potential $\varphi_o(\vec{r})$ was calculated using Ansoft MAXWELL 3D [42] to solve Poisson's equation:

$$\nabla^2\varphi = -\frac{\rho}{\in} \tag{4}$$

where φ is electric potential, ρ is the net charge density, and $\in$ is the dielectric constant of germanium. $\varphi_o(\vec{r})$ is found by setting a single strip at unit potential, all other strips at zero potential and all charges removed [7]. A 2D cut of the calculation (perpendicular to the strip at unit potential) was output on a 100 μm Cartesian grid for the region underneath the strip at unit potential ± 2 strips away. Then the position of $\varphi_o(\vec{r})$ for one strip was applied for every strip in the simulated detector.

III.B.2.2. Carrier path calculation

The net induced signal Q_{net} of a charge cloud is determined by the paths travelled by of each of its charge carriers. The position of a charge carrier $\vec{r}_i(j)$ at any time step j is dependent on the carrier velocities $\vec{v}_e(\vec{r})$ and $\vec{v}_h(\vec{r})$, as determined by $\vec{E}(\vec{r})$ and electron and hole mobility, and charge-carrier diffusion.

III.B.2.2.1. Carrier velocity calculation

The magnitude of charge-carrier velocity $\boldsymbol{v}$ in (1) is determined using an empirical equation found by Burks et al. for use in an HPGe DSSD [23]:

$$v(E(\vec{r})) = \frac{\mu_o E(\vec{r})}{\left[1+\left(\frac{E(\vec{r})}{E_o}\right)^{\beta}\right]^{\frac{1}{\beta}}} \tag{5}$$

where $E(\vec{r})$ is electric field magnitude at position $\vec{r}$, μ_o is low field mobility, and E_o and β are empirical constants. Values for the latter three from [23] are used. They are different for electrons and holes, and they assume a temperature of 80 K.

III.B.2.2.2. Charge-carrier diffusion

To properly calculate carrier path for a charge cloud, the UM HPGe detector code models charge-carrier diffusion, the only significant mechanism of carrier spreading. The standard deviation σ for the spatial distribution of diffused carriers in a charge cloud is modeled in one lateral dimension by: [43]

$$\sigma = \sqrt{\frac{2kTz}{eE_{avg}}} \tag{6}$$

where k is Boltzmann's constant, T is the temperature in Kelvin, each carrier in the cloud travels an axial distance z from its original position $\vec{r}_i(0)$ to the detector surface $\vec{r}_i(t_{f,i})$, e is an elementary charge, and E_{avg} is the average magnitude of the electric field. In each lateral dimension, *x* and *y*, the diffusion of each carrier in a charge cloud is sampled from a Gaussian distribution given by σ. If a carrier *i* travels an axial distance

z_i from $\vec{r}_i(0)$ to $\vec{r}_i(t_{f,i})$, the lateral distance it diffuses along *x* over the same path is $\vec{r}_{diff,x}$, and the axial distance it travels until time step j is $z_{i,j}$, then it diffuses a distance $\vec{r}_{diff,x,i}\sqrt{\frac{z_{i,j}}{z_i}}$ along *x* from $\vec{r}_i(0)$ to $\vec{r}_i(j)$. Thus, at any time step *j* where $t \le t_{f,i}$, a carrier *i* has diffused a distance

$$\vec{r}_{diff,i}(j) = \left(\vec{r}_{diff,x,i} + \vec{r}_{diff,y,i}\right)\sqrt{\frac{z_{i,j}}{z_i}} \qquad (7)$$

Consistent with measurement results in [22], diffusion was calculated to be ~100 μm over 10 mm of travel in the UM HPGe detector. To determine the path of any carrier as it drifts to the detector surface, drift and diffusion are combined. Thus, the position $\vec{r}_i$ of a carrier *i* at time step j is given by

$$\vec{r}_i(j) = \vec{r}_i(0) + \vec{r}_{diff,i}(j) + \sum_{k=1}^{j}\left[\vec{v}_i(\vec{E}(\vec{r}_i(k))) \times t_{step}\right] \qquad (8)$$

where the third term is a recursive implementation of carrier drift. It depends upon the calculation of $\vec{E}(\vec{r})$, which is discussed in the next section.

III.B.2.3. Electric field calculation

A 2D version of Synopsys MEDICI [44] was used to numerically solve for the electric field. MEDICI solves Poisson's equation (Eqn 4) and the continuity equations (and current relations) for both holes and electrons in semiconductors. It also allows for use of different numerical solution techniques and physical models, which incorporate both Boltzmann and Fermi-Dirac statistics.

P-type germanium was specified along with the uniform impurity concentration, operating temperature, bias voltage, and geometry of our detector (stated in II.C.1). Boundaries included blocking contacts on top and bottom of the material. These blocking contacts simulate the blocking behavior of the ~0.1-μm thick a-Ge layer. A two carrier Newton solution method was employed because it is the most stable solution method, and it solves all relevant semiconductor equations.

III.B.2.3.1. Axial electric field

First, an analytic expression for axial electric field in the detector bulk is presented. The axial electric field magnitude E_z as a function of depth from the anode surface ***z*** is given by [43]:

$$\left|E_z(z)\right| = \frac{V_a}{T} + \frac{eN}{\varepsilon}\left(z - \frac{T}{2}\right) \tag{9}$$

where V_a is the operating voltage, T is the detector thickness, e is elementary charge, N is the dopant concentration, and ε is the dielectric constant of the medium. The depletion voltage V_d is [43]:

$$V_d = \frac{eNT^2}{2\varepsilon} \tag{10}$$

Combining (9) and (10) yields

$$\left|E_z(z)\right| = \frac{2V_d}{T^2}z + \frac{(V_d - V_a)}{T} \tag{11}$$

Numerical calculation of axial electric field in the detector bulk, as shown in Fig. 15(b) for the cathode side, agrees with this analytic expression. However, within 500 μm of the strips, electric field becomes either significantly stronger or weaker than Eqn. 11 predicts,

depending on the proximity to the gap center, and a lateral component of electric field E_ℓ becomes significant as well. This lateral electric field is described in the next section.

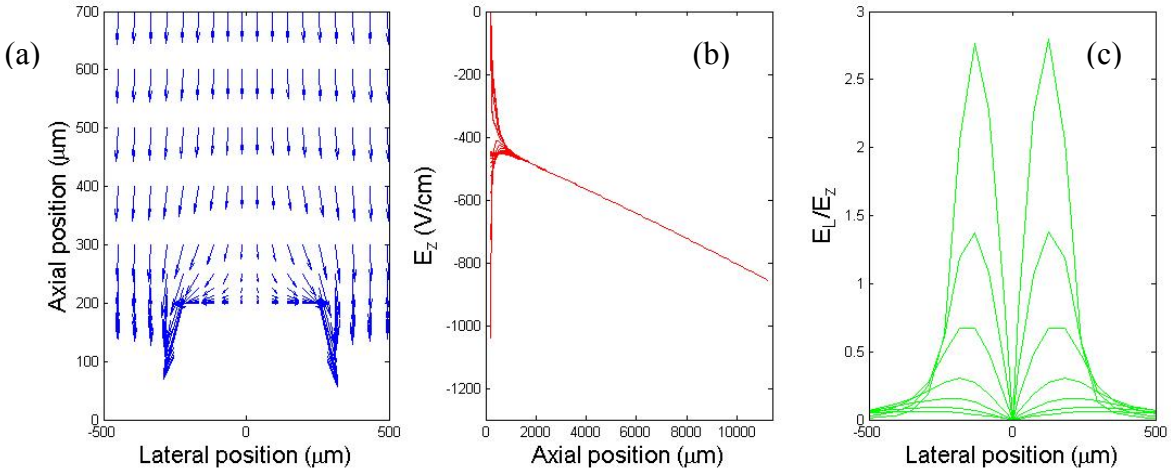

Fig. 15. (a) Electric field vectors in the vicinity of a gap are shown. (b) Axial electric field E_z is plotted for the same lateral positions. (c) The ratio of lateral-to-axial field E_ℓ / E_z is plotted as a function of depth from the cathode surface. In order from highest to lowest amplitude, the depths plotted are 25, 50, 100, 200, 300, 400, and 500 μm.

III.B.2.3.2. Lateral electric field

Electric field calculations on the cathode side are given in Fig. 15. In Fig. 15(a), electric field vectors in the vicinity of a gap are shown. The cathode surface is chosen to begin at axial position 200 μm; the gap center is at lateral position zero. In Fig. 15(b), E_z is plotted for the same lateral positions shown in Fig. 15(a). As mentioned, axial field strength calculated by MEDICI in the detector bulk is consistent with Eqn. 11. In Fig. 15(c), the ratio of lateral-to-axial field $\frac{E_\ell}{E_z}$ is plotted as a function of depth from the cathode surface. In the gap region, the relative importance of E_ℓ increases with proximity to the collecting cathode strips. The relatively weak $\frac{E_\ell}{E_z}$ near the gap center

could allow some charge-carriers to remain stranded there. As a carrier's distance from the gap center increases, this likelihood decreases due to the strengthening of $\frac{E_\ell}{E_z}$.

For a carrier *i* at a time step *j*, the UM HPGe detector code determines the electric field $\vec{E}(\vec{r}_i(j))$ analytically. In the detector bulk, the electric field is determined by Eqn. 11. When *i* is close to the gap surface, the result of Eqn. 11 is multiplied by an equation with the following form, which was fit to simulation results shown in Fig. 15:

$$\left|\frac{E_\ell(x,z)}{E_z(x,z)}\right| = C_1 e^{z'}\left|\frac{\sin^3(C_2 x)}{x}\right| \tag{12}$$

where *x* is the lateral distance from the gap center, *z* is depth, *z'* is a scaled depth, and C_1 and C_2 are fitting constants. While C_2 affects the lateral position of the peaks in $\frac{E_\ell}{E_z}$, C_1 affects their amplitude.

The shape of the electric field at the anode surface was calculated to be identical to the one at the cathode surface. However, experimental data suggest that $\frac{E_\ell}{E_z}$ may be weaker on the anode side compared to the cathode side. Further discussion of these differences is deferred for discussion with experimental results in Chapter IV.

III.B.2.4. Preamplifier simulation

A simple preamplifier response model was employed from the GRETA code [41]. The rise time $T_{rise} = 10ns$ and fall time $T_{fall} = 300\mu s$ of the preamplifier are specified to produce a shaped pulse from the application of Eqn. 3 through RC integration and differentiation. Preamplifier and other electronic noise are not included in simulations, but are estimated to be ~1 keV FWHM at 4 μs peaking time based upon energy resolution measurements at 60 keV.

III.B.2.5. Drifting of carriers to the gap surface

Charge-carrier collection for interactions in the gap was modeled using three different techniques in order to determine which technique(s) produced best agreement with data, which will be presented in Chapters IV and V. In each technique, the path carriers travelled to the surface was calculated using Eqn. 8. The starting point for these techniques is the method described in [13], where a 60 keV charge cloud was modeled as a point charge that drifted vertically, but not laterally, to the surface. Carriers that started under a strip drifted to a strip at the surface and were collected, so the calculated energy was 60 keV. For signals that drifted to the gap surface, the energy of 60 keV was multiplied by the sum of the weighting potentials for each strip at the final surface position. Their charge loss calculation is shown as the line across the data in Fig. 7(d), and, for convenience, the figure is reproduced below in Fig. 16. This idea seemed to account for measured charge loss at 60 keV [13]. It predicted a maximum charge collection deficiency of 5%.

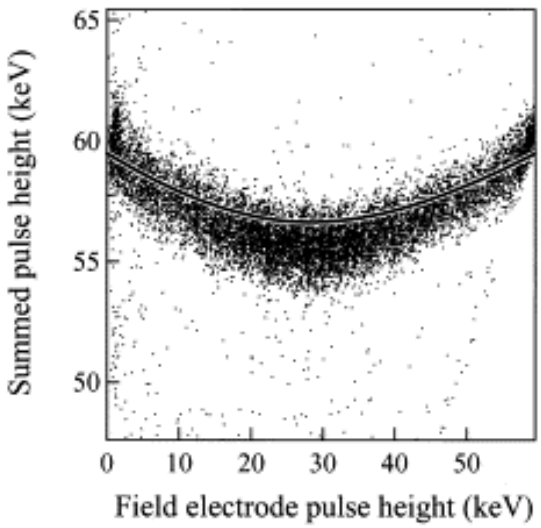

Fig. 16. An HPGe DSSD was irradiated with a 60 keV source. Scatter plots of summed pulse height from adjacent strips are plotted against the pulse height from one of the strips. The line across the data shows the simulated result using a weighting potential method described in the text. [13]

In the UM HPGe detector code, the charge cloud is not modeled as a point charge drifting straight to the surface. Instead, the path of all carriers in a cloud is calculated. Thus, the expected variance in charge loss and charge-splitting introduced by charge clouds can be calculated. For each technique, if a carrier *i* reaches a strip at time $t_{f,i}$, the final φ_o of the strip it reaches is set to 1 while the final φ_o of the adjacent strip is set to 0. The differences in the three techniques are described next. Each makes assumptions, and it is presumed that benchmarking with data will identify which assumptions are acceptable. This approach is necessary because it is very difficult to model the charge trapping and transport which occurs in the a-Ge layer.

In the first technique, if *i* does not reach a strip by $t_{f,i}$, the final φ_o for each adjacent strip is set equal to the numerically calculated surface φ_o at its lateral position. While E_ℓ affects lateral position as a carrier drifts to the surface, the carrier is not transported to

either nearby strip after it reaches the gap surface. Instead, its chance of collection by each strip over the event time period is modeled by the final φ_o on that strip.

In the second technique, E_ℓ is set to zero and carriers are drifted to the surface as before. Charge cloud size and spreading by diffusion are still taken into account in this technique. Upon arrival at the gap surface, carriers are not transported to either nearby strip. Instead, a carrier's chance of collection by each strip is modeled again by the final φ_o on that strip. This technique assumes that weighting potentials happen to model the effects of both E_ℓ and carrier transport in the a-Ge layer.

In the third technique, carriers are drifted to the detector surface as they are in the first technique. Upon arrival at the gap surface, carriers are not transported to either nearby strip. In this technique, it is assumed that none of these carriers reach a collecting strip within the event time period. For each carrier, the final φ_o on each adjacent strip is set to zero. If any carriers are collected by adjacent strips, Eqn. 3 dictates that a non-zero net signal is induced because the net signal is the superposition of the signal induced by each carrier.

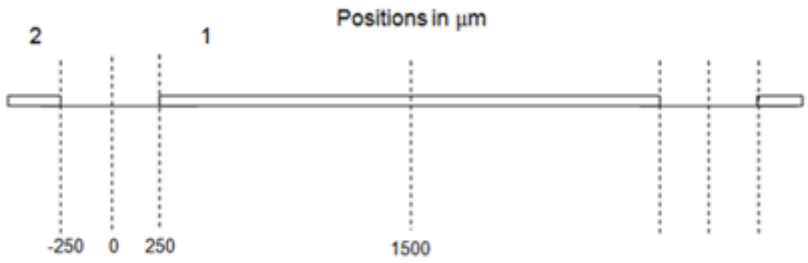

Fig. 17. Schematic of lateral position relative to a strip gap in the UM HPGe DSSD.

III.C. Simulated charge-splitting and charge loss response

Three techniques to model detector gap response using the UM HPGe detector code are discussed in this section. Each employs Monte Carlo calculations, where the photoelectron direction of any history is randomly selected. To quantify the Monte Carlo calculations, the charge loss fraction f_i for the i^{th} history is defined as

$$f_i \equiv 1 - \frac{(E_1 + E_2)_i}{E_{peak}} \tag{13}$$

where E_1 and E_2 are calculated energies on adjacent strips 1 and 2 as pictured in Fig. 17, and E_{peak} is the photopeak energy. The quantity $1 - f_i$ is called the charge collection fraction, and its maximum value is 1.0. It is a calculation of the fraction of charge-carriers from a single cloud which are collected by adjacent strips. The charge-splitting ratio

$$r_i \equiv \frac{E_{1,i}}{E_{1,i} + E_{2,i}} \tag{14}$$

and will be shown to be indicative of lateral position. This quantity extends from 0 to 1 as an interaction moves across the gap from strip 2 to strip 1. It is a calculation of the splitting of a charge cloud between the two strips. For each technique, all simulated

charge clouds have been drifted from a depth of 5.5 mm (from either surface), the axial center of the detector. Furthermore, the calculation for anode and cathode gaps is the same.

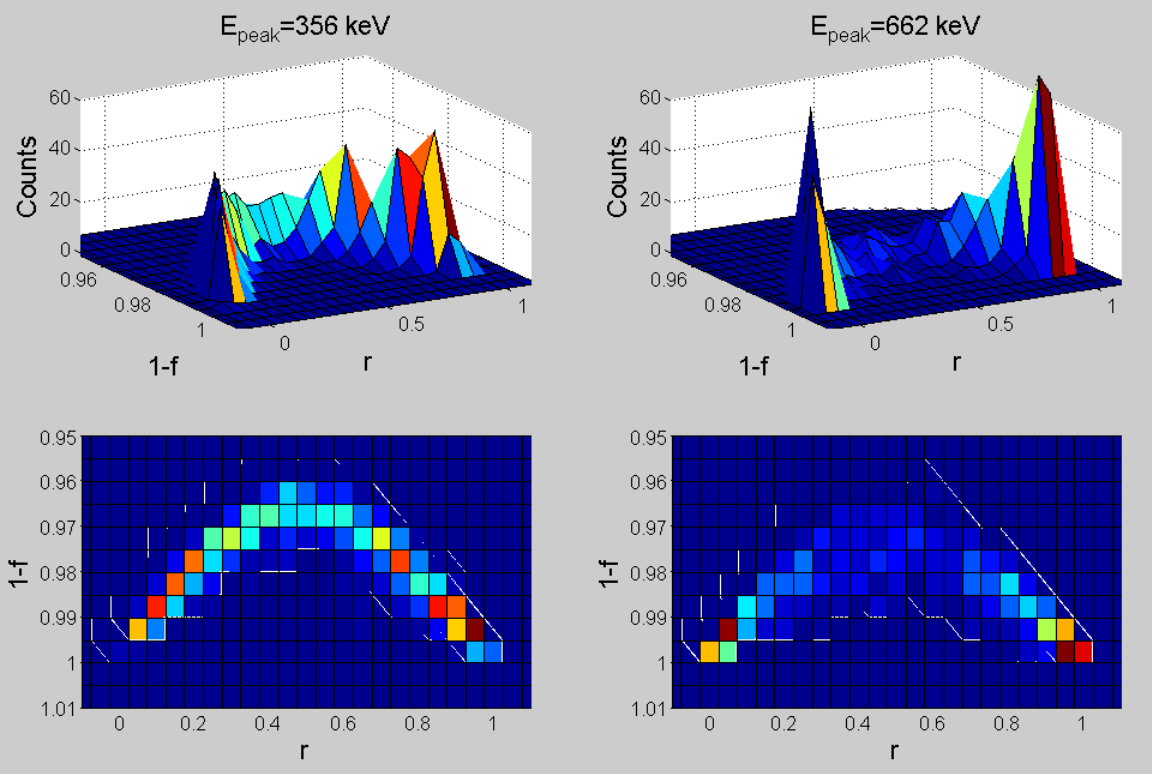

Fig. 18. Charge-splitting and charge loss response for 356 keV or 662 keV photo-interactions originating at the center of the UM HPGe detector gap. Surface modeling technique 1 was employed.

III.C.1. Surface modeling technique 1

The UM HPGe detector code was used to simulate the detector response to 356 keV or 662 keV photo-interactions in a detector gap using surface modeling technique 1. The charge-splitting and charge loss response for 1000 histories originating at the gap center are shown in Fig. 18. Photopeak energy E_{peak} is shown in each column heading. In Fig. 18, each history is binned by both charge-splitting and charge collection, and two

different views at each E_{peak} are displayed by rows. The second row shows a top view of the first row.

In Fig. 18, the calculations show that charge-carriers are more likely to be collected by either adjacent strip at 662 keV compared to 356 keV, affecting both charge-splitting and charge collection. This is due to larger cloud size at 662 keV and the increased lateral spreading of this cloud by E_{ℓ}, which is stronger toward strip edges. The lateral spreading by diffusion is the same at 356 keV and 662 keV because all histories originate at the same depth. In Fig. 18, also note that the fraction of charge-carriers collected for 356 keV or 662 keV photo-interactions is calculated to be greater than 96%.

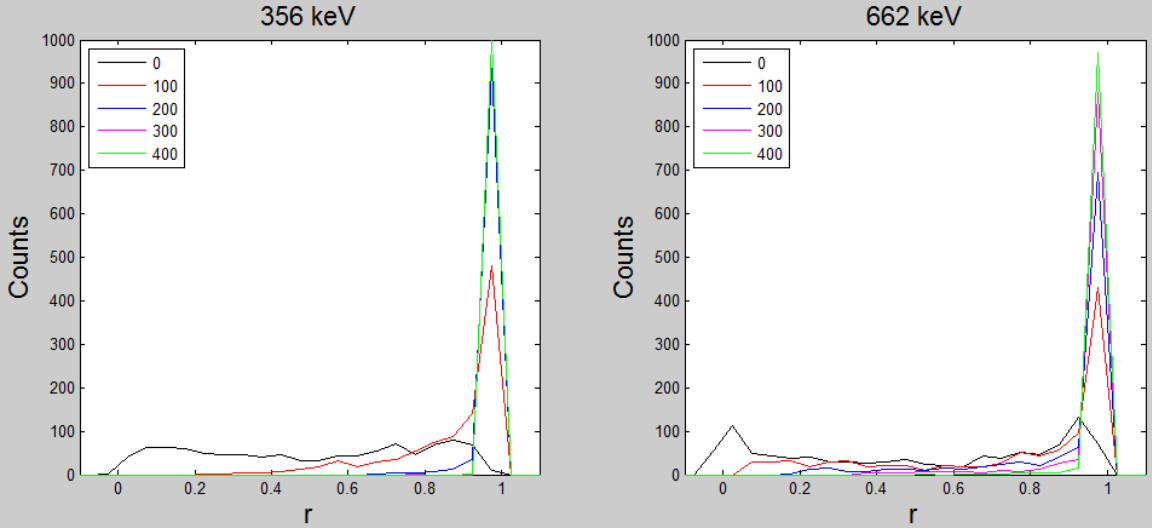

Fig. 19. Charge-splitting ratio for 356 keV or 662 keV photo-interactions as interaction position is moved in 100 μm increments toward strip 1. Surface modeling technique 1 was employed.

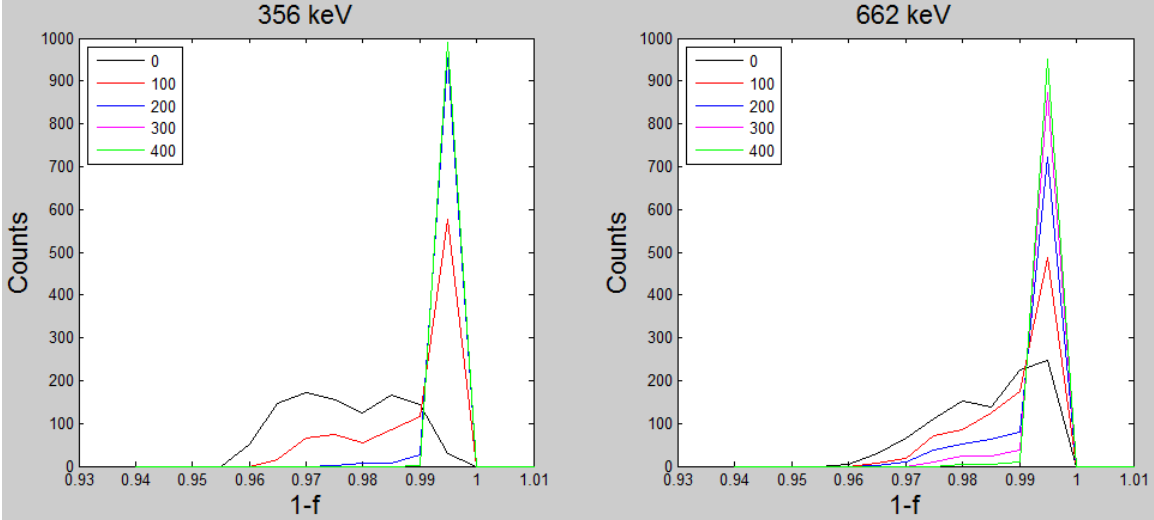

Fig. 20. Charge collection fraction for 356 keV or 662 keV photo-interactions as interaction position is moved in 100 μm increments toward strip 1. Surface modeling technique 1 was employed.

Fig. 19 and 20 show the calculated detector response as the interaction position is moved laterally toward strip 1 in 100 μm increments. Irradiation energies are given in figure headings and positions are indicated in the legends. At 200 μm, a large fraction of 356 keV and 662 keV photo-interactions are fully collected by strip 1. Although these interactions originate 50 μm from the edge of strip 1, nearly all the carriers in the simulated clouds are drawn to strip 1 by the strong E_ℓ at the detector surface, which is shown in Fig. 15.

If surface modeling technique 1 properly models detector gap response, Fig. 20 shows that a degraded photopeak (composed of $E_1 + E_2$) should be measured if a 662 keV source is collimated directly to the gap center. The photopeak should be further degraded if the source is replaced by a 356 keV source. Additionally, as the collimator position shifts in 100 μm increments toward strip 1, the response shown in Fig. 19 and Fig. 20 should be observed.

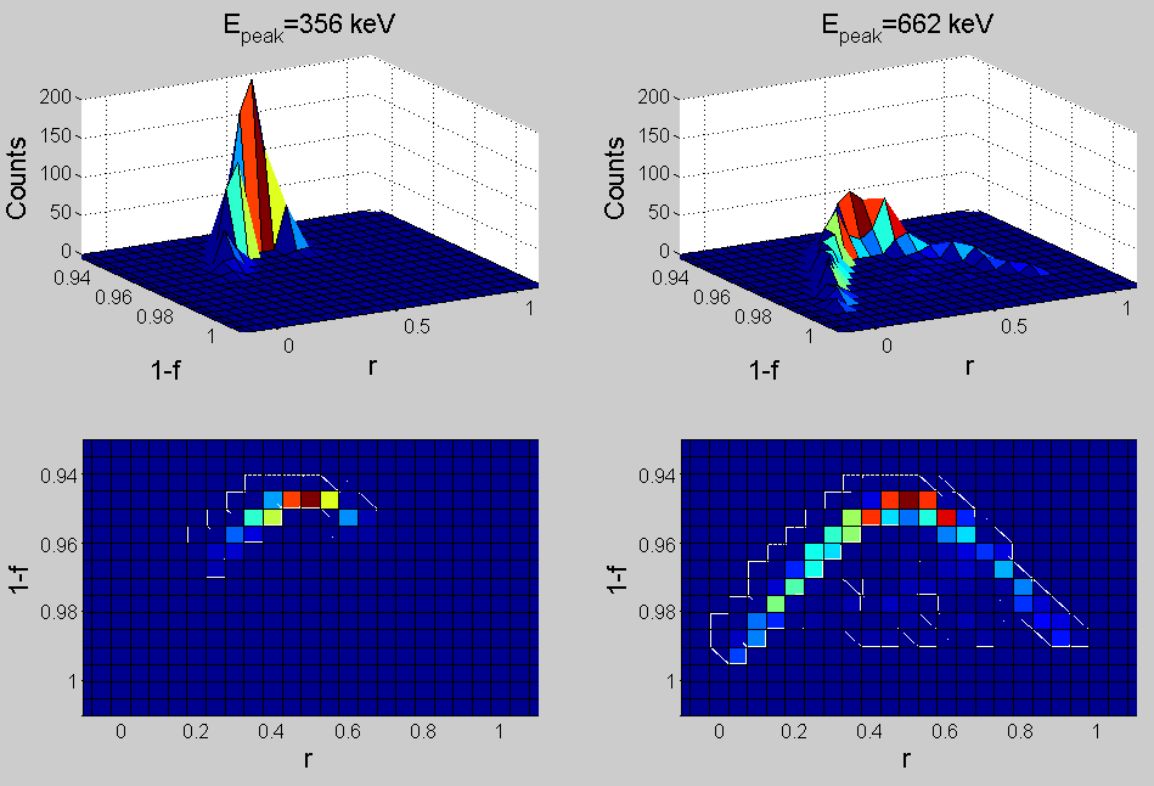

Fig. 21. Charge-splitting and charge loss response for 356 keV or 662 keV photo-interactions originating at the center of the detector gap. Surface modeling technique 2 was employed.

III.C.2. Surface modeling technique 2

Next, the calculation is repeated with $E_\ell = 0$ in the gap region. This technique assumes that the weighting potential method employed happens to model the effects of both E_ℓ and carrier transport in the a-Ge layer. The response at the gap center using this second technique is shown in Fig. 21. At 356 keV, every history is calculated to lose 3-6% of its charge carriers. As before, the collection fraction at 662 keV is higher due to larger cloud size. However, in the absence of applied lateral fields, some measureable fraction of carriers remains uncollected for the majority of 662 keV histories.

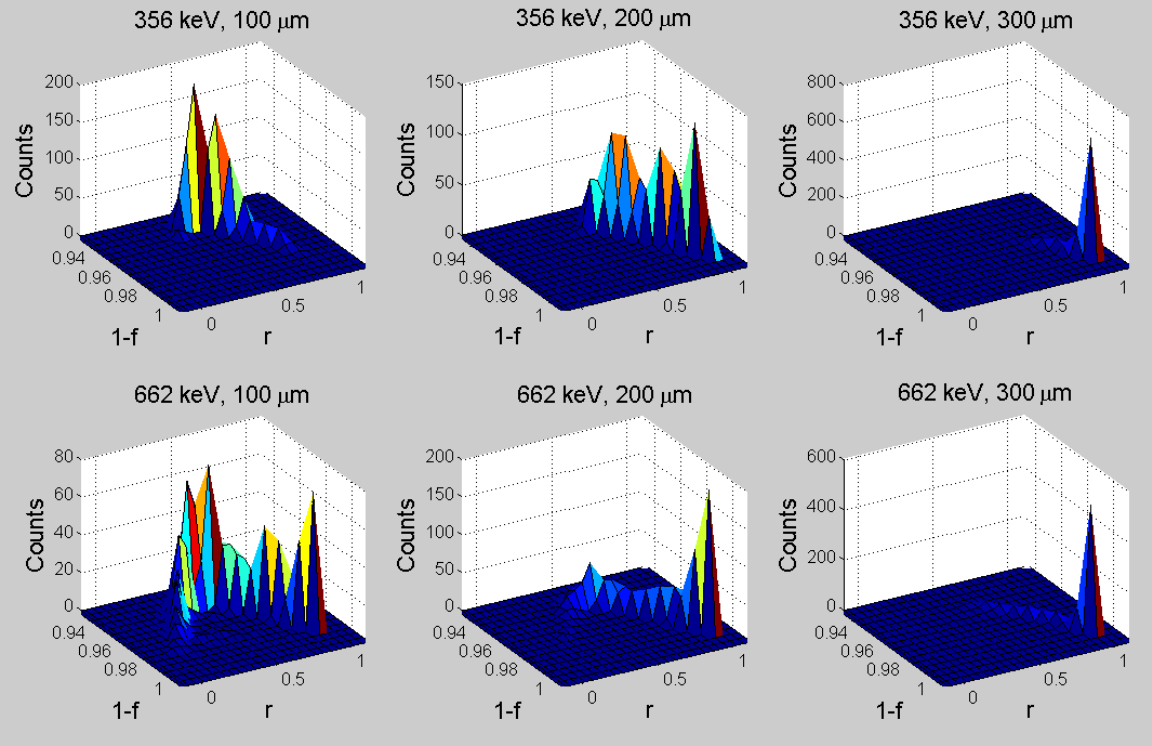

Fig. 22. Charge-splitting and charge loss response for 356 keV or 662 keV photo-interactions originating 100, 200, and 300 μm from the gap center (moving directly toward strip 1). Surface modeling technique 2 was employed. Note that different vertical scales are used.

Fig. 22 shows the calculated detector response as interaction position moves toward strip 1 in 100 μm increments. Irradiation energies and positions are indicated in figure headings. In comparison to the response calculated by the first technique (see Fig. 19), the change in r and $1-f$ is much more gradual with changing position when the second technique is employed. This can be better seen in Fig. 23 and Fig. 24, which show projections of Fig. 22. Fig. 23 shows the change in r with lateral interaction position, and Fig. 24 shows the change in $1-f$ at the same positions.

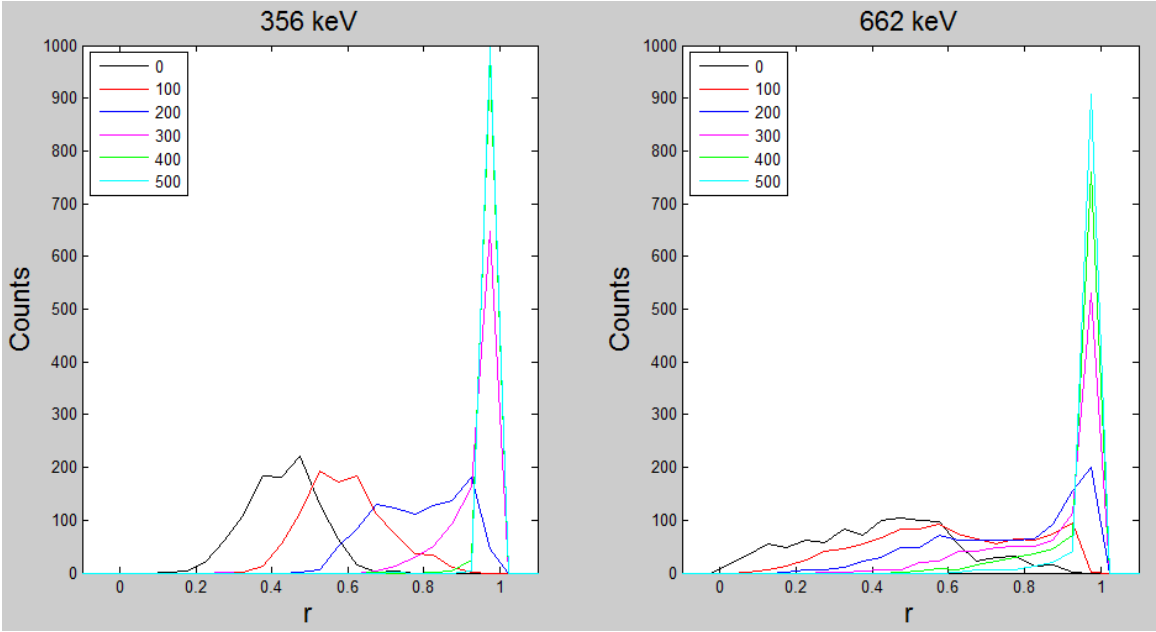

Fig. 23. Charge-splitting ratio for 356 keV or 662 keV photo-interactions originating at lateral positions shown in the legend. Surface modeling technique 2 was employed.

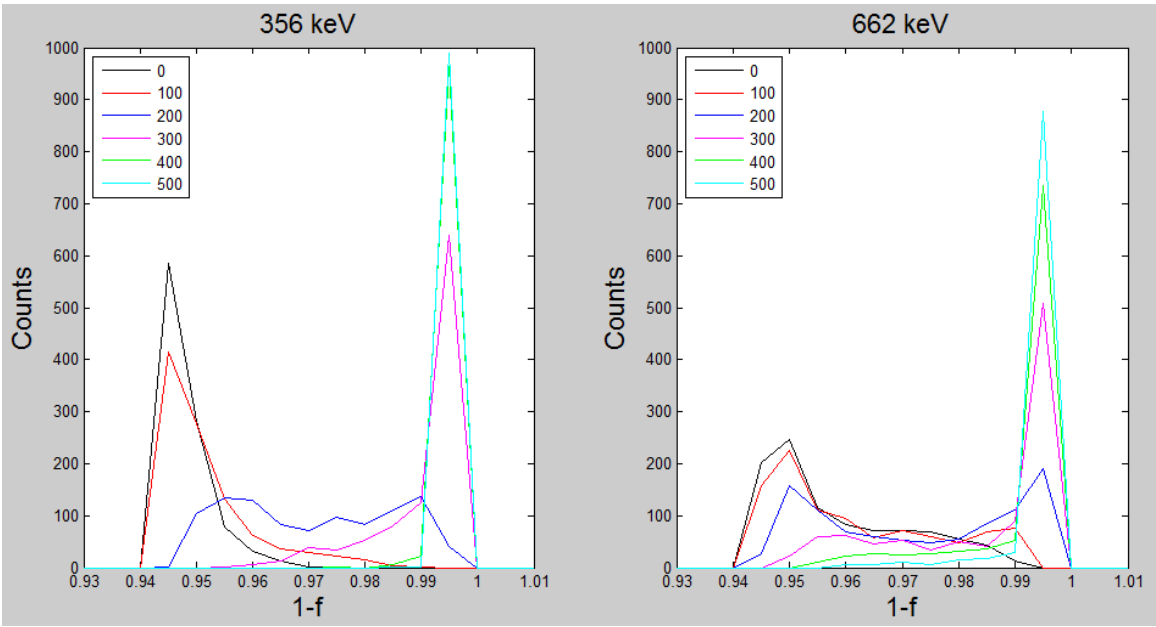

Fig. 24. Charge collection fraction for 356 keV or 662 keV photo-interactions originating at lateral positions shown in the legend. Surface modeling technique 2 was employed.

If surface modeling technique 2 properly models detector gap response, Fig. 21 suggests that a photopeak should not be observed on strip 1 or strip 2 if a 356 keV or 662 keV source is collimated directly to the gap center. However, Fig. 24 suggests that a

photopeak composed of $E_1 + E_2$ should be measured at $0.95 \times 356\ keV = 338\ keV$ if a 356 keV source is collimated directly to the gap center. Furthermore, if this source is replaced by a 662 keV source, a less prominent peak (composed of $E_1 + E_2$) should be observed at $0.95 \times 662\ keV = 629\ keV$. Additionally, as the collimator position shifts in 100 μm increments toward strip 1, the response shown in Fig. 21-23 should be observed.

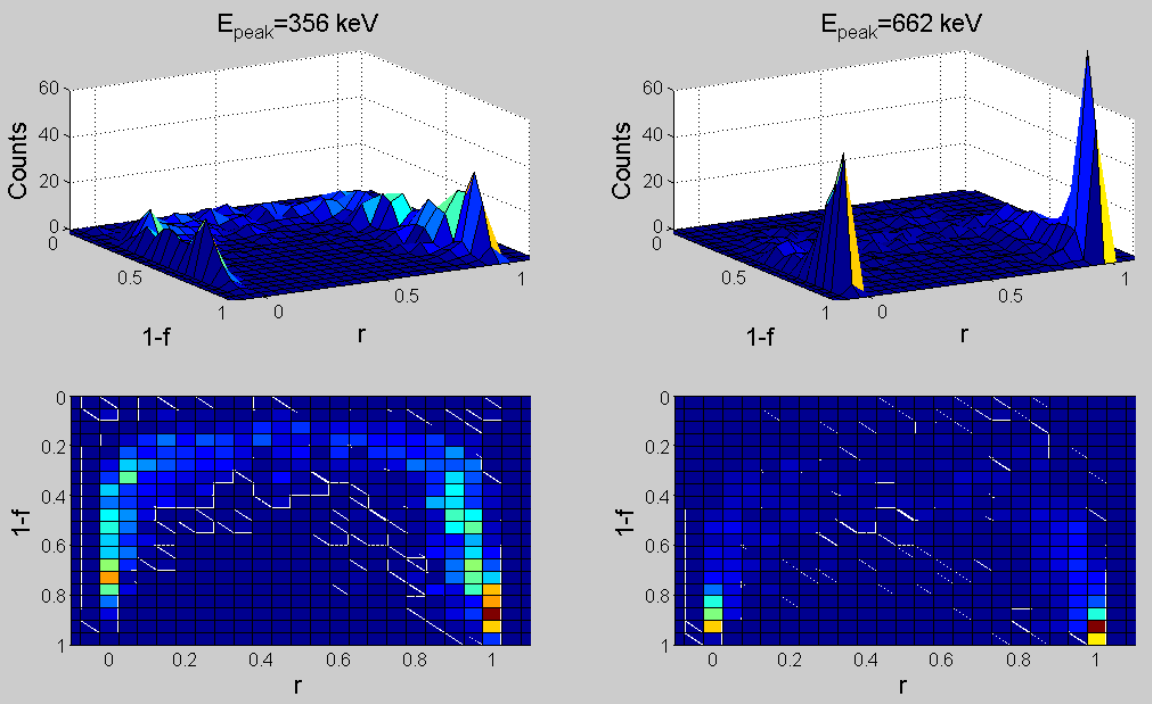

Fig. 25. Charge-splitting and charge loss response for 356 keV or 662 keV photo-interactions originating at the center of the detector gap. Surface modeling technique 3 was employed.

III.C.3. Surface modeling technique 3

Finally, the calculation was repeated employing the third technique. All methods of lateral spreading are accounted for in this technique. However, it is assumed that the a-Ge layer does not transport any carriers to be collected by either strip over a time period relevant for measurements. Fig. 25 shows the detector response for interactions at the gap center. Notice that the scale on the $1-f$ axis has been changed to show the full

range of charge collection. This technique predicts that 356 keV or 662 keV photo-interactions at the gap center may lose any fraction of charge carriers to the a-Ge layer. In contrast to the first two surface modeling techniques, less than 90% of all charge-carriers are collected for the majority of 356 and 662 keV histories.

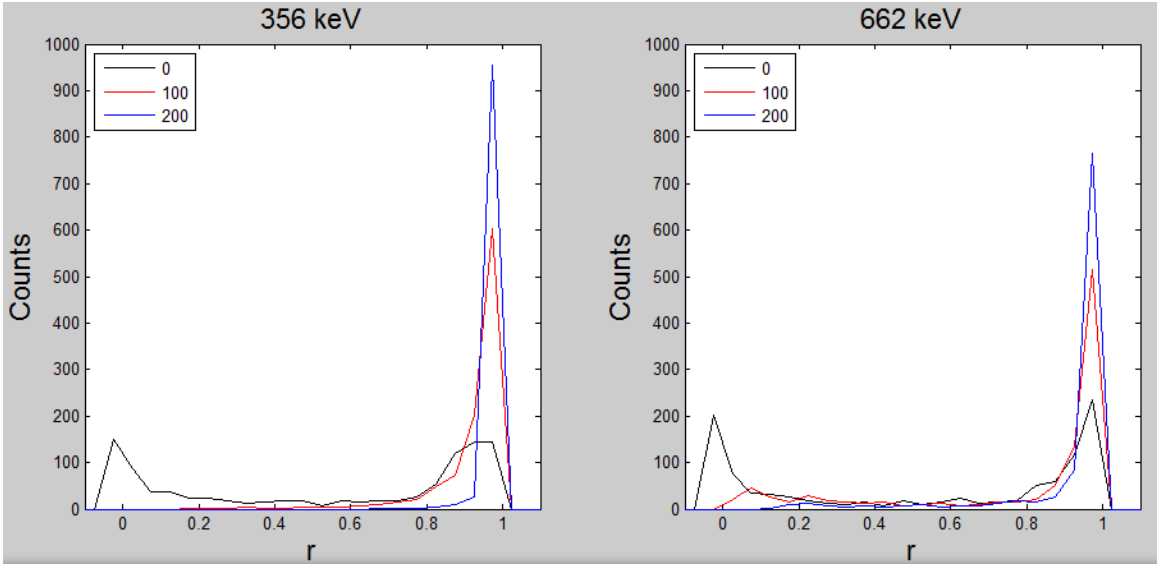

Fig. 26. Charge-splitting ratio for 356 keV or 662 keV photo-interactions originating 0, 100, and 200 μm from the gap center. Surface modeling technique 3 was employed.

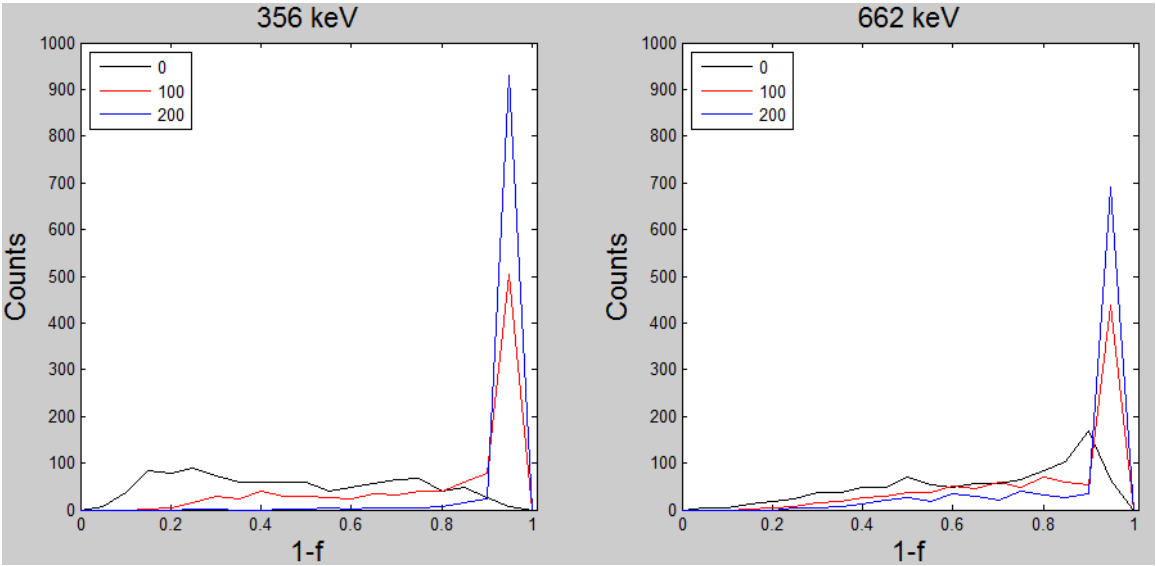

Fig. 27. Charge collection fraction for 356 keV or 662 keV photo-interactions originating 0, 100, and 200 μm from the gap center. Surface modeling technique 3 was employed.

Fig. 26 and Fig. 27 show the calculated detector response as interaction position is moved toward strip 1 in 100 μm increments. Fig. 26 shows the charge-splitting ratio, and Fig. 27 shows the charge collection fraction. If the third technique properly models the a-Ge layer, there should be no 356 keV or 662 keV photopeaks if sources of these energies are collimated directly to the gap center, i.e., photopeaks are not expected from the spectra composed of E_1, E_2, or $E_1 + E_2$. Instead, the spectra composed of $E_1 + E_2$ would resemble those shown in Fig. 26. Due to the very high charge loss expected, it would be necessary to use a technique to resolve the true spectrum from its continuum.

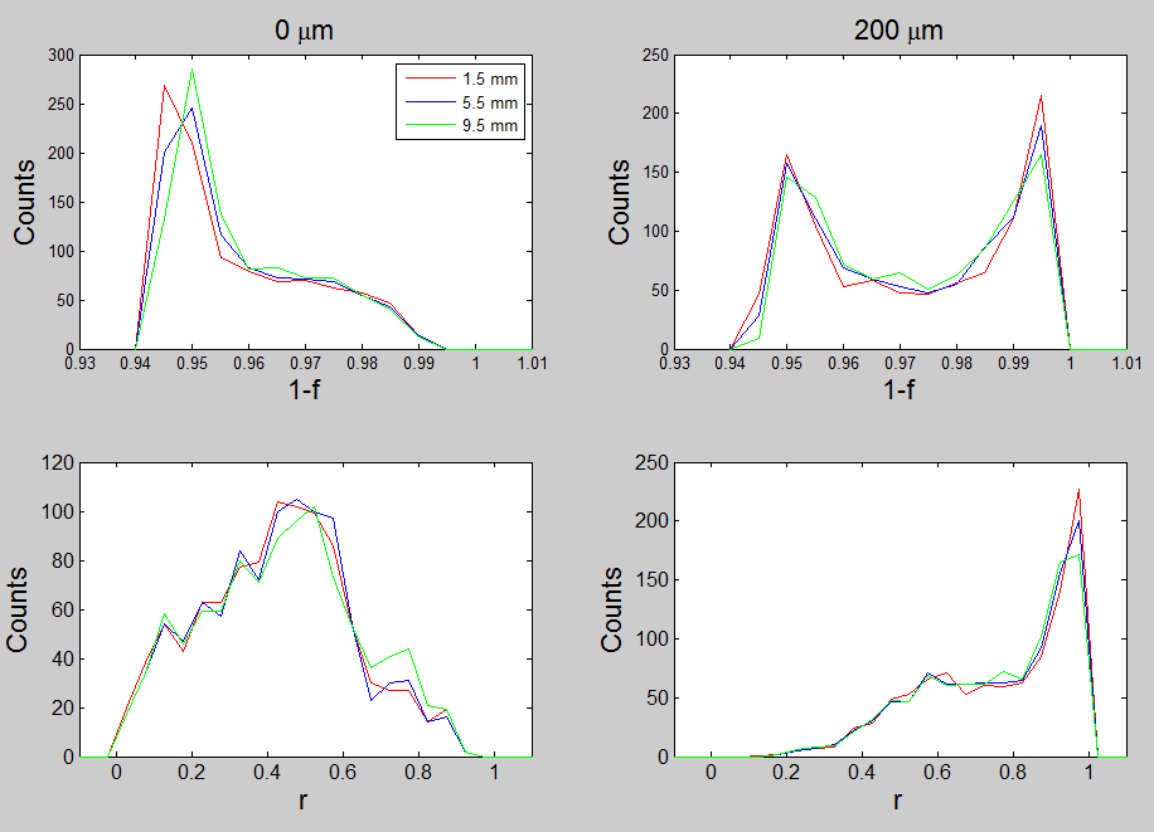

Fig. 28. Charge collection and charge loss response for two lateral interaction positions for 662 keV interactions at 1.5, 5.5 mm, and 9.5 mm depths. Lateral positions are given in column headings, and depths are indicated in the legend.

III.C.4. Change in gap response with interaction depth

It has been assumed that the depth of all simulated interactions was 5.5 mm, i.e., the axial center of the detector. In each surface modeling technique, a change in response was observed as lateral interaction position moved from the gap center toward the edge of strip 1. Fig. 28 shows the difference in response using surface modeling technique 2 at two lateral interaction positions for 662 keV interactions at 1.5, 5.5, and 9.5 mm depths. The depths are relative to the side where signals are collected. Lateral positions are indicated by column headings and depths are given in the legend. Surface modeling technique 2 was employed because it agrees best with measurements at the anode side, as the next chapter will show.

At the gap center (0 μm), charge collection becomes slightly more probable as interaction depth increases. This is attributed to the spread of carriers from the gap center toward strip edges. At 200 μm, nearer to the strip edge, charge collection becomes slightly less probable as interaction depth increases. This is attributed to the spread of carriers away from the strip edge. Overall, the change in response with interaction depth is much less significant than the change in response with lateral position. The change in diffusion from one depth to another is a small change because, according to Eqn. 7, which is dependent upon $\sqrt{\frac{1}{z_i}}$, carriers do the greatest fraction of their spreading nearer to their place of origin.

Chapter IV

Charge loss measurement and correction

This chapter presents charge loss measurements, describes the charge loss correction method, and gives results of implementing the method for Single Site Interactions. Additionally, simulations of the detector gap are discussed to provide understanding of measurement results.

IV.A. Charge loss measurement and simulation

First, some terms are defined and discussed to provide improved understanding of the methods presented in Chapters IV and V. Next, charge loss measurements are described, and simulation results are presented for understanding.

IV.A.1. Event classification

An event is defined as any interaction or interaction sequence which causes at least one strip on each detector side to trigger in the Spect32 system. This system was briefly described in II.C.2. An interaction sequence always begins with a Compton scatter as its first interaction. If the final interaction of the sequence is photoelectric, it results in full energy deposition in the detector. An event lasts at most 120 ns in duration, as determined by the mobility of carriers in the HPGe crystal.

A loss event is defined as any interaction or interaction sequence where one interaction falls close enough to a gap that some measurable fraction of its carriers remain uncollected by either adjacent strip over the event time period. A Close Compton Event (CCE) is defined as any event where more than one interaction from the same sequence falls within the lateral bounds of two adjacent strips with respect to either detector side. Any other event is classified as a Single Site Interaction (SSI). CCEs and SSIs may also be loss events. The charge loss correction method described in IV.B and V.C is applied to loss events only. CCEs and SSIs require different charge loss correction methods.

A gap event is defined as any interaction or interaction sequence where one interaction falls close enough to a gap that: 1) some measurable fraction of its carriers remain uncollected by either adjacent strip, or 2) both adjacent strips are triggered by a Single Site Interaction. According to this definition, gap events include loss events. The inter-strip interpolation method described in Chapter V is applied to all gap events. CCEs and SSIs may also be gap events. CCEs and SSIs require different approaches to inter-strip interpolation.

For an in-strip SSI, the depth of an interaction is determined by the difference in 50% constant fraction times between anode and cathode signals. The depth resolution of the Spect32 system was determined to be ± 20 ns using the method described in [45], which corresponds to ±1 mm. According to this method, the depth resolution can be determined from separate irradiations of anode and cathode sides with a 60 keV source.

A 1-1 event is defined as an event which causes a single strip to trigger on each detector side. A 2-1 event is defined as an event which causes two triggers on one side and a single trigger on the opposite side. All 1-1 events and any 2-1 or 2-2 events where

signals trigger adjacent strips within 20 ns of each other are presumed to be SSIs. In the UM detector, 20 ns equates to a distance travelled by a carrier of about 1 mm. All other 2-1, 2-2, and 2-3 events where two adjacent strips fire on a detector side at different times are categorized as CCEs.

For example, measured CCE statistics are given at two gamma ray energies. At 356 keV, 43% of events which cause adjacent triggers in the UM detector were identified as CCEs based upon trigger type and timing. Comparing triggers on opposite detector sides, three interactions fall within the lateral bounds of two adjacent strips for nearly 6% of these events. At 662 keV, 56% of events which cause adjacent triggers in our detector were identified as CCEs. Over 8% of these events consisted of 3 interactions. Thus, CCEs account for roughly half of adjacent triggers in the 300-800 keV range. Further discussion of the fraction of measured CCEs is deferred to V.C.3.1.

IV.A.2. Description of apparatus

A 4 mCi Cs-137 source or a 2 mCi Ba-133 source can be collimated in two dimensions, each adjustable by micrometer heads with 1 μm precision, as shown in Fig. 16. In each of the two collimation layers, the machined smooth hevimet used is 8 cm thick in order to adequately attenuate 662 keV gamma rays, and slits as small as 25 μm can be produced. The collimated radiation source is capable of 2.5 μm precision positioning in 2D by means of a precision positioning system. While the detector is secured to the frame of this system, a mounted laser level and a digital protractor system (with precision 0.01°) are used for external detector-beam alignment.

Referring to Fig. 29, the radiation beam is collimated to the side of the detector such that its dimensions are constrained along the detector depth and one lateral dimension. The detector cryostat sits atop a 30 liter liquid nitrogen (LN_2) dewar. The detector is oriented inside its cryostat (as pictured in Fig. 10) so that the cathode strips run perpendicular to the floor, and the anode strips run parallel to the floor. Accordingly, the box on top of the detector houses the cathode preamplifiers, and the box on the side houses the anode preamplifiers. Power is supplied to each preamplifier box from a NIM bin power supply. The detector itself was described in greater detail in II.C.1.

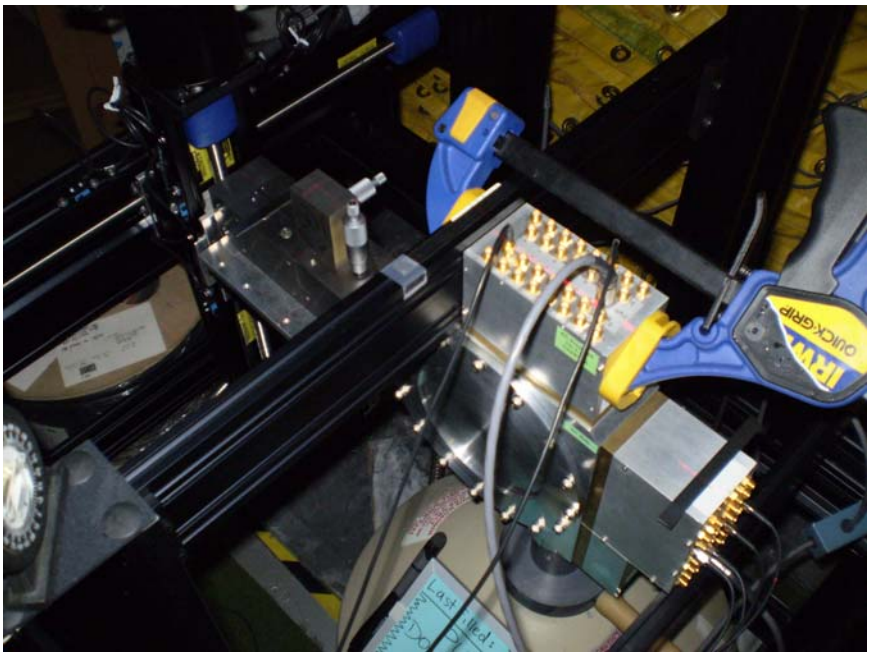

Fig. 29. Photograph of experimental apparatus. From back left to front right side, 2D precision positioning system, shielded radiation source, adjustable 2D collimator, and radiation detector inside its cryostat.

IV.A.3. Charge loss experimental setup

To measure charge loss, the detector was mounted perpendicular to the direction shown in Fig. 29 such that radiation was incident normal to a detector face. At 356 keV or 662 keV, the radiation penetrates through the entire depth of the detector so that the

side of irradiation is inconsequential for this experiment. For examination of charge loss at the anode surface, the 2 mCi Ba-133 source was collimated between two adjacent anode strips. The spot size of the beam from the 50 μm slit was calculated using a ray tracing technique. Given the setup geometry and the attenuation coefficient of the collimator, the incident beam was determined to have FWHM=68 μm at 662 keV. At 356 keV, FWHM=56 μm. The beam was collimated perpendicular to the anode strips using a 1 cm slit in order to minimize the misalignment concerns that a fan beam poses across the entire detector diameter (of ~8 cm). While all strips on the cathode side were instrumented, only eight adjacent channels on the anode side were instrumented. For examination of charge loss at the cathode surface, the setup was reversed: the source was collimated to 50 μm between two adjacent cathode strips and 1 cm perpendicular to the cathode strips, eight adjacent cathode strips were instrumented, and the entire anode side was instrumented.

IV.A.4. Charge loss measurements

To quantify the charge loss in the UM detector, the charge loss fraction f_i for the i^{th} event is defined as

$$f_i = 1 - \frac{(E_1 + E_2)_i}{E_{peak}}$$

where E_1 and E_2 are measured energies on adjacent strips 1 and 2 as pictured in Fig. 1(c), and E_{peak} is the expected peak energy. The average charge loss fraction $\overline{f}_j$ observed at lateral position j is thus

$$\overline{f}_j = \frac{\sum_{i=1}^{N_j} f_i}{N_j}$$

with an *rms* of

$$f_{j\,rms} = \sqrt{\frac{\sum_{i=1}^{N_j} f_i^2}{N_j}}$$

where N_j is the number of measured events at position j. Other metrics are the maximum charge loss fraction $f_{j\,\max}$ and the most probable charge loss fraction $f_{j\,p}$.

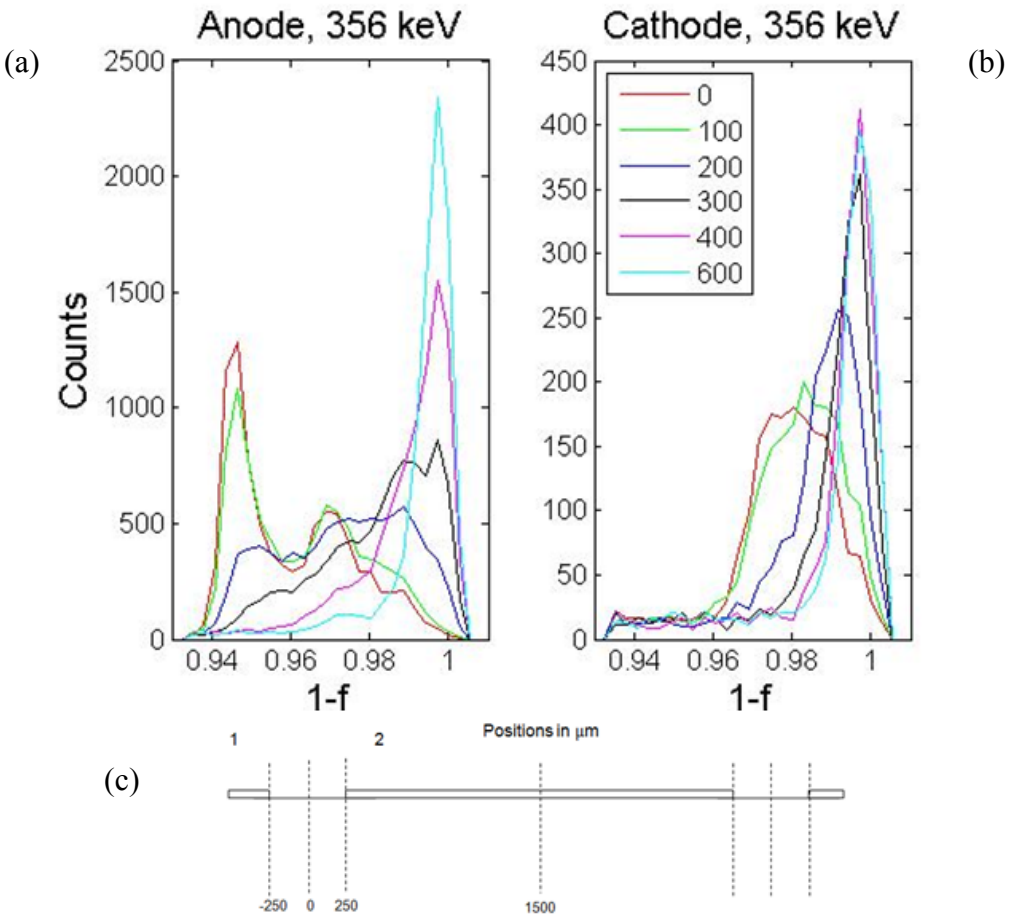

Fig. 30. Measured SSI distributions $S_j(E)$ for a 356 keV source collimated between (a) two adjacent anode strips, or (b) two adjacent cathode strips. The legend shows lateral positions in µm from the gap center, as shown in the reference 1D coordinate system (c).

To measure charge loss, a Ba-133 source was collimated between two adjacent strips, as described in IV.A.3. Consider strips 1 and 2 depicted in Fig. 30(c). The 1D coordinate system used here has its origin at the gap center, and positions are given in μm. The amplitudes, or energies, of adjacent strips 1 and 2 are summed together since each strip may collect charge carriers from a gap interaction. The energy distribution formed from binning this sum for a number of events at collimator position j is referred to as distribution $S_j(E)$, where E refers to energy. Fig. 30(a) shows measured SSI distributions $S_j^{anode}(E)$ when this 356 keV source is collimated between two adjacent anode strips. Fig. 30(b) shows SSI distributions $S_j^{cathode}(E)$ for collimation between two adjacent cathode strips. Event energies have been divided by E_{peak} so that each photoelectric event i is binned according to its collection fraction $1-f_i$. Figure legends give collimator positions in μm with respect to the origin. Considering normal statistical fluctuations over a fixed counting time, N_j is the same at each position.

As the gap center is approached on either detector side, charge loss increases. In fact, the gap center is identified as the position j where $\overline{f}_j$ is at its maximum. At the gap center, $f_{\max} = 0.07$ and $f_p = 0.055$. Fig. 31 gives values of $\overline{f}_j$ and $f_{j\,rms}$ for the distributions $S_j(E)$ shown in Fig. 30. The behavior of $\overline{f}_j$ and $f_{j\,rms}$ are symmetric about the gap center, so only the half between the gap center and strip 2 is shown. As the edge of strip 2 is approached, $\overline{f}_j$ and $f_{j\,rms}$ decrease because charge collection probability increases. Within strip bounds, $f_{j\,rms}$ is still non-zero due to noise. The quantity $\overline{f}_j$ is usually non-zero due to carrier loss, which is seen when adjacent strips are summed

together. Alternatively, $\overline{f}_j$ may be non-zero because the energy calibration of strip 1 and strip 2 together is slightly different than that of 1 or 2 alone.

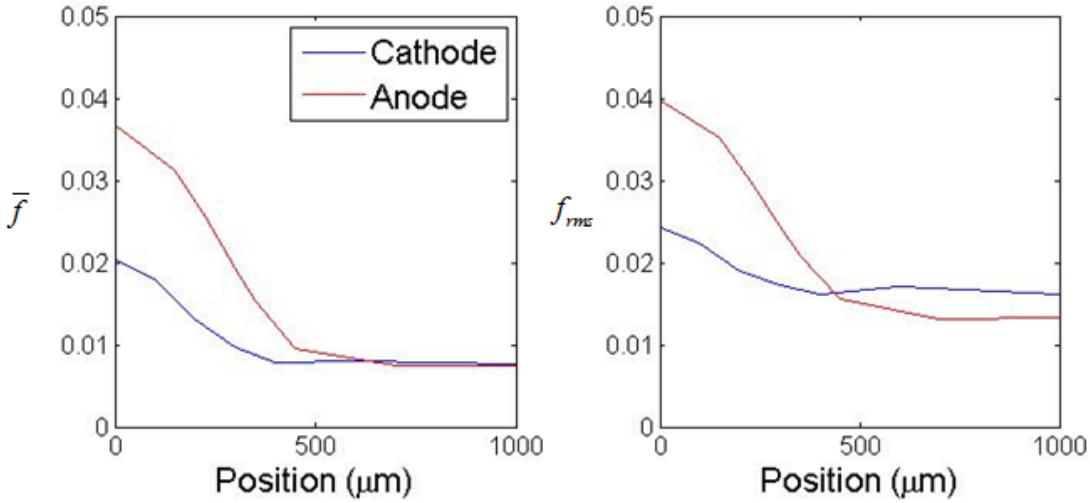

Fig. 31. (a) Average charge loss fraction $\overline{f}$ for the distributions $S_j(E)$ shown in Fig. 30. (b) Root mean squared of charge loss fraction f_{rms} for the distributions $S_j(E)$ shown in Fig. 30.

IV.A.5. Difference in charge loss between anode and cathode sides

Charge loss on the cathode side of the UM detector is significantly lower compared to the anode side, i.e., the charge loss response is asymmetric. While the dominant mechanism of charge cloud spreading in the detector bulk is diffusion, it cannot account for the difference in measured charge loss between the anode and the cathode side. We presume a hole cloud drifting from the anode to cathode side should undergo a similar spreading as an electron cloud drifting from the cathode to anode side. Furthermore, a high charge loss region near the anode gap surface, as suggested in [37], is inconsistent with our measurement results: collimated measurements at 356 and 662 keV show significant charge loss on both the anode and cathode sides for interactions at all depths.

Although there is no fabrication difference between the opposing sides [14], the difference in charge loss between anode and cathode sides likely results from a difference

in the surface electric field at the anode relative to the cathode. The difference in surface electric field may be introduced by the presence of fixed surface charge from traps at the a-Ge layer. Depending on the nature of the traps, the surface charge can be positive or negative in polarity [46]. Since anode and cathode sides collect carriers which are opposite in polarity, the effect of the fixed charge may be asymmetric.

IV.A.5.1. Validation of surface modeling techniques

Testing this idea requires the validation of at least one of the simulation surface modeling techniques described in III.C for proper charge loss response. It is clear that surface modeling technique 3 does not model charge loss response for either detector side appropriately, so it is excluded from consideration. In Fig. 32, charge loss response from anode side measurements and surface modeling technique 2 are compared. Irradiation energies are shown in column headings. Agreement is excellent for $1-f<0.955$. Above this point, agreement is good, but one main discrepancy is noticeable. There appears to be a peak in the 356 keV data at $1-f\sim0.97$ and in the 662 keV data at $1-f\sim0.965$, but these peaks are not present in simulations. These peaks are attributed to both beam spreading and CCEs which were not properly separated as SSIs. While the first Compton scatter is constrained to the gap center due to collimation, it is unlikely that the next interaction also occurs in the gap. Thus, the amount of charge loss is proportional to this first energy deposition while the full scattered photon energy can be recorded under a neighboring strip. These CCEs, called unresolved CCEs, are not properly separated through timing methods because the two interactions occur at similar depths.

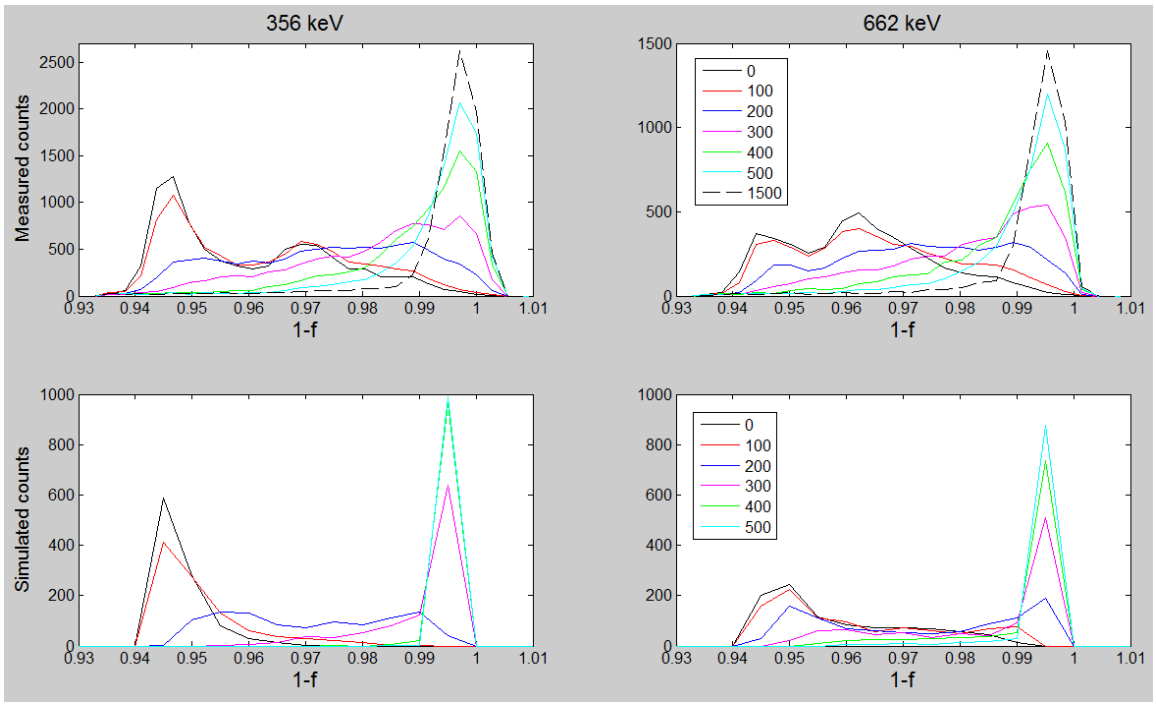

Fig. 32. Comparison of charge loss between anode side measurements (top row) and surface modeling technique 2 (bottom row) at 356 keV and 662 keV.

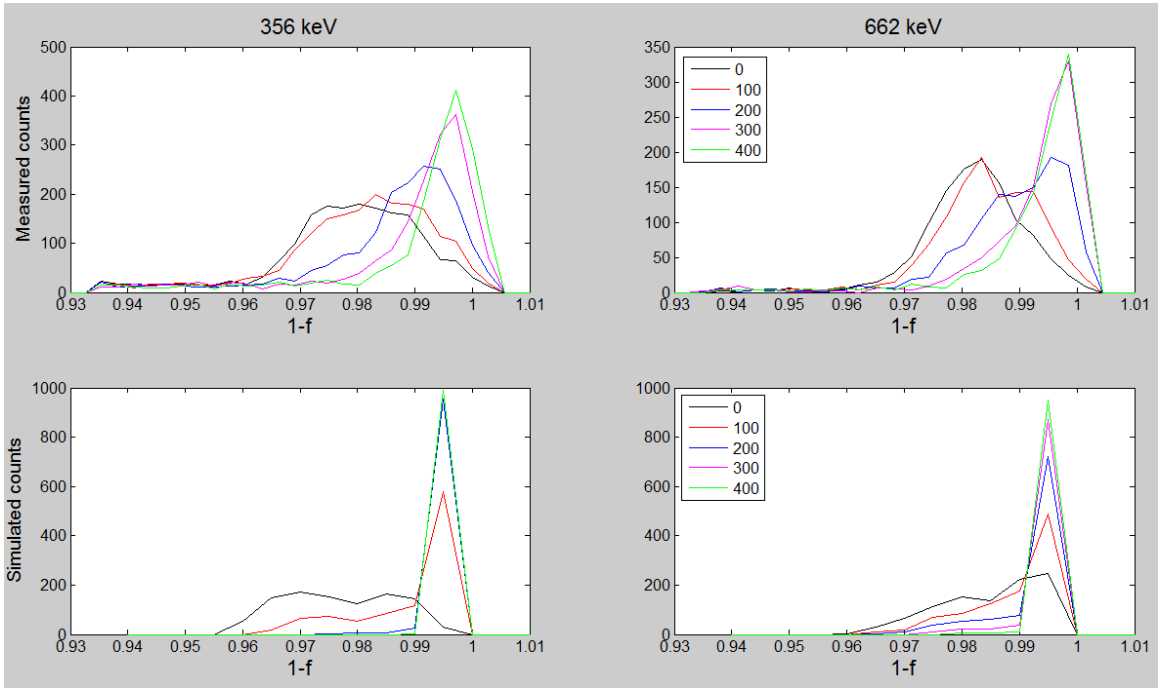

Fig. 33. Comparison of charge loss between cathode side measurements (top row) and surface modeling technique 1 (bottom row) at 356 keV and 662 keV.

In Fig. 33, charge loss response from cathode side measurements and surface modeling technique 1 are compared. Surface modeling technique 2 was not compared to cathode charge loss measurements because agreement is very poor. While the agreement is not good for surface modeling technique 1, there is one main similarity between simulation and measurement. The simulation correctly predicts that the bulk of charge loss occurs at $1-f>0.955$ at 356 and 662 keV for any interaction position. Surface modeling technique 2 predicts a much lower limit at $1-f>0.94$. At 662 keV, this is a difference of 10 keV.

Thus, surface modeling technique 2 has been validated for proper charge loss response at the anode side. On this side, weighting potentials happen to model the combined effects of E_ℓ and carrier transport in the a-Ge layer. Yet, Fig. 33 shows that the response at the cathode surface is consistent with a stronger $\frac{E_\ell}{E_z}$ compared to the anode surface. Furthermore, the disagreement between cathode data and surface modeling technique 1 shows that the effects of both E_ℓ and carrier transport in the a-Ge layer have not been properly modeled at the cathode surface.

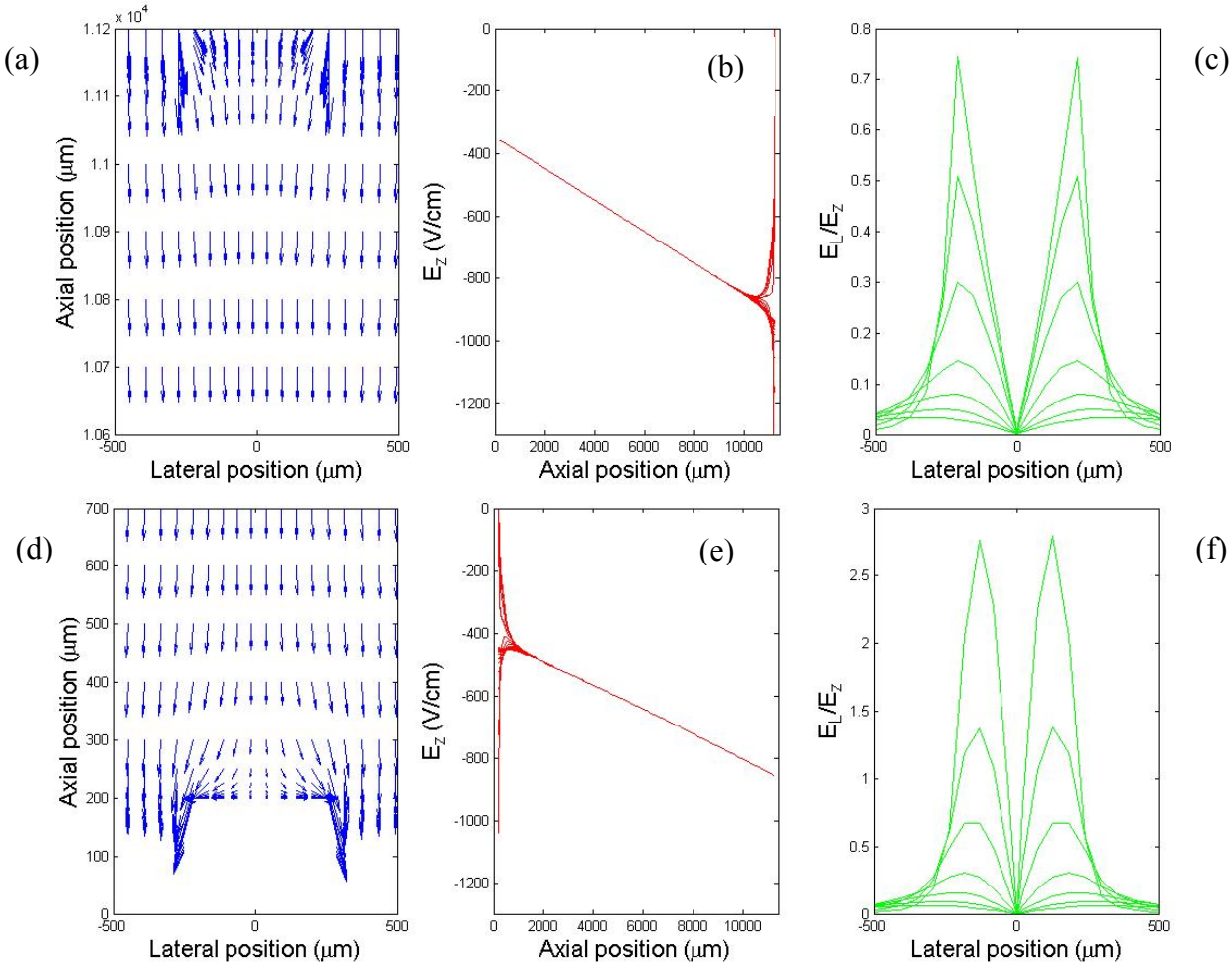

Fig. 34. Anode side electric field simulation. A fixed plane of positive charge is assumed at the surface. For explanation of (a), (b), and (c), refer to Fig. 15. For comparison, Fig. 15 has been reproduced in (d-f). Note that (c) and (f) have different vertical scales.

IV.A.5.2. Simulation of fixed surface charge

Now that a surface modeling technique has been validated, the idea proposed for the difference in charge loss between anode and cathode sides will be explored. It is proposed that there is a difference in $\frac{E_\ell}{E_z}$ between anode and cathode sides which is introduced by the presence of fixed surface charge from traps at the a-Ge layer. In Fig. 34 (a-c), a plane of positive charge has been introduced at the anode surface. The ratio of

fixed surface charge to the space charge in the detector bulk is 1.0. For comparison, Fig. 15 has been reproduced in Fig. 34 (d-f).

Comparing Fig. 34(a) to Fig. 34(d), the electric field vectors in the gap now tend to direct charge-carriers more toward the surface. Comparing Fig. 34(c) to Fig. 34(f), the amplitude of the $\frac{E_\ell}{E_z}$ distribution has been significantly reduced, and further reduction (to zero amplitude) occurs with an increase in surface charge density. Furthermore, the peaks in the distribution shift out from the gap center toward the edges. These changes may result in an increase in incomplete charge collection at the anode surface.

At the cathode surface, negative fixed charge must be introduced to have the same effect on $\frac{E_\ell}{E_z}$. However, the magnitude of fixed charge for the same effect on $\frac{E_\ell}{E_z}$ is smaller because $|E_z|$ is much weaker at the cathode surface compared to the anode surface, as observed in Fig. 34(b) and Fig. 34(e). If the same magnitude of fixed charge (i.e., a ratio of 1.0) is introduced at the cathode side, then $\frac{E_\ell}{E_z}$ becomes negligibly small. If positive fixed charge is introduced instead, the effect is reversed, increasing $\frac{E_\ell}{E_z}$ and charge collection probability.

The difference in charge loss at anode and cathode sides may be attributed to the presence of fixed positive charge at the anode surface. As described above, this results in $\left(\frac{E_\ell}{E_z}\right)_{anode} < \left(\frac{E_\ell}{E_z}\right)_{cathode}$. In this scenario, surface modeling technique 2 happens to model the combined effects of a weakened E_ℓ and carrier transport in the a-Ge layer at the

anode surface. Alternatively, a smaller magnitude of positive fixed charge may be introduced at the cathode surface. In this alternative scenario, surface modeling technique 2 happens to model the combined effects of E_ℓ and carrier transport in the a-Ge layer at the anode surface. At the cathode surface, $\frac{E_\ell}{E_z}$ is strengthened by the presence of positive fixed charge. Thus, $\left(\frac{E_\ell}{E_z}\right)_{anode} < \left(\frac{E_\ell}{E_z}\right)_{cathode}$, as before. In either scenario, the difference in $\frac{E_\ell}{E_z}$ between anode and cathode sides is consistent with the observed difference in charge collection between these sides.

IV.B. Charge loss correction method and results

The difference in detector response between sides necessitates separate anode and cathode corrections. Additionally, SSIs must be handled differently than CCEs. In any case, the first step is to identify events that require correction. Charge loss could be identified in an absolute sense if the expected photopeak energy is known. But it is more useful to identify charge loss on one side relative to the other because: 1) no *a priori* knowledge of E_{peak} is assumed, and 2) this allows for correction of events which do not deposit the full energy of the incident gamma ray in the detector. It is reasonable to identify charge loss this way in the UM detector because charge loss observed at both sides is improbable: while the chance that an interaction will fall in a gap on one side is 1/6, the chance that it will fall within a gap with respect to both sides is 1/36. Lateral electric fields in the gap reduce charge loss even further, reducing the chance of charge

loss on both sides to less than 1%. Thus, the measured energies on one side are used to correct the loss on the opposite side.

IV.B.1. Correction method for Single Site Interactions

The following empirical equation was utilized to correct for incomplete charge collection in Single Site Interactions:

$$E_{new}(E_1, E_2) = (E_1 + E_2) + k_1 E_{\min} - \frac{k_2 E_{\min}^{\ 2}}{E_1 + E_2} \qquad (15)$$

$$k_1 = k_2 = 0.21 \qquad (Anode)$$
$$k_1 = 0.11 \quad k_2 = 0.16 \quad (Cathode)$$

where E_1 and E_2 are adjacent strip energies before correction, E_{new} is the corrected energy, k_1 and k_2 are fitting constants, and $E_{\min}$ is the minimum of E_1 and E_2. The fitting constants were empirically determined to give the best correction for loss events acquired from collimated measurements at 356 and 662 keV (as shown in Fig. 32 and Fig. 33). Section B.3 defines what constitutes the best correction.

IV.B.2. Correction method for Close Compton Events

Consider a CCE consisting of two interactions. For a 2-2 event that is a CCE, if measured energies on the anode and cathode sides are the same, it is likely that each of the two interactions is directly underneath each of the two adjacent strips. Some additional lateral position information may be inferred for each interaction by considering only the fast signal adjacent to it [47]. Alternatively, signal decomposition algorithms might be used to precisely determine interaction locations [48].

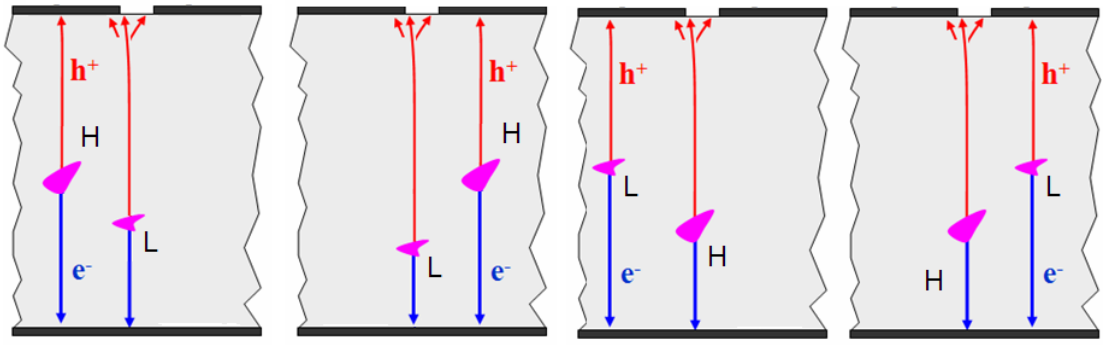

Fig. 35. For a CCE with 2 interactions, where one interaction loses charge to a gap, there are four possible scenarios for the relative positions of two higher (H) and lower (L) energy interactions.

However, if there if a deficit in energy on one side of up to $f_{\max} = 0.07$, it is likely that the CCE is also a loss event. Because the charge carriers from a gap interaction may be collected by both adjacent strips, this introduces a challenge in determining the position of each interaction. Fig. 35 depicts four possible scenarios for the relative positions of two higher (H) and lower (L) energy interactions when two adjacent strips trigger. Peak-to-peak measurements of fast signals adjacent to the strips pictured do not provide enough information to identify the correct scenario. Without identifying the scenario, an energy correction cannot be performed. Thus, energy correction for CCEs will be further discussed along with inter-strip interpolation in Chapter V.

IV.B.3. Correction results for Single Site Interactions

Although charge loss corrections are designed to work on an event-by-event basis, the result is evaluated for sets of data by examining:

(1) The shift of $f_{j\,p}$ toward zero for all j

(2) The shift of $\overline{f}_j$ toward zero for all j

(3) The decrease of $f_{j\,rms}$ for all j

(4) The increase in photopeak counts

As discussed, noise provides a lower limit for $f_{j\,rms}$. Additionally, the increase in photopeak counts is limited to the gap-to-strip width ratio, which is 1/6, in the case where $\frac{E_\ell}{E_z} = 0$. As $\frac{E_\ell}{E_z}$ increases, carrier collection probability increases, so the maximum possible change in photopeak counts decreases from 1/6.

Next, these 4 criteria are employed to test the effectiveness of charge loss correction for SSIs. Correction results are shown for collimated beam and flood field measurements.

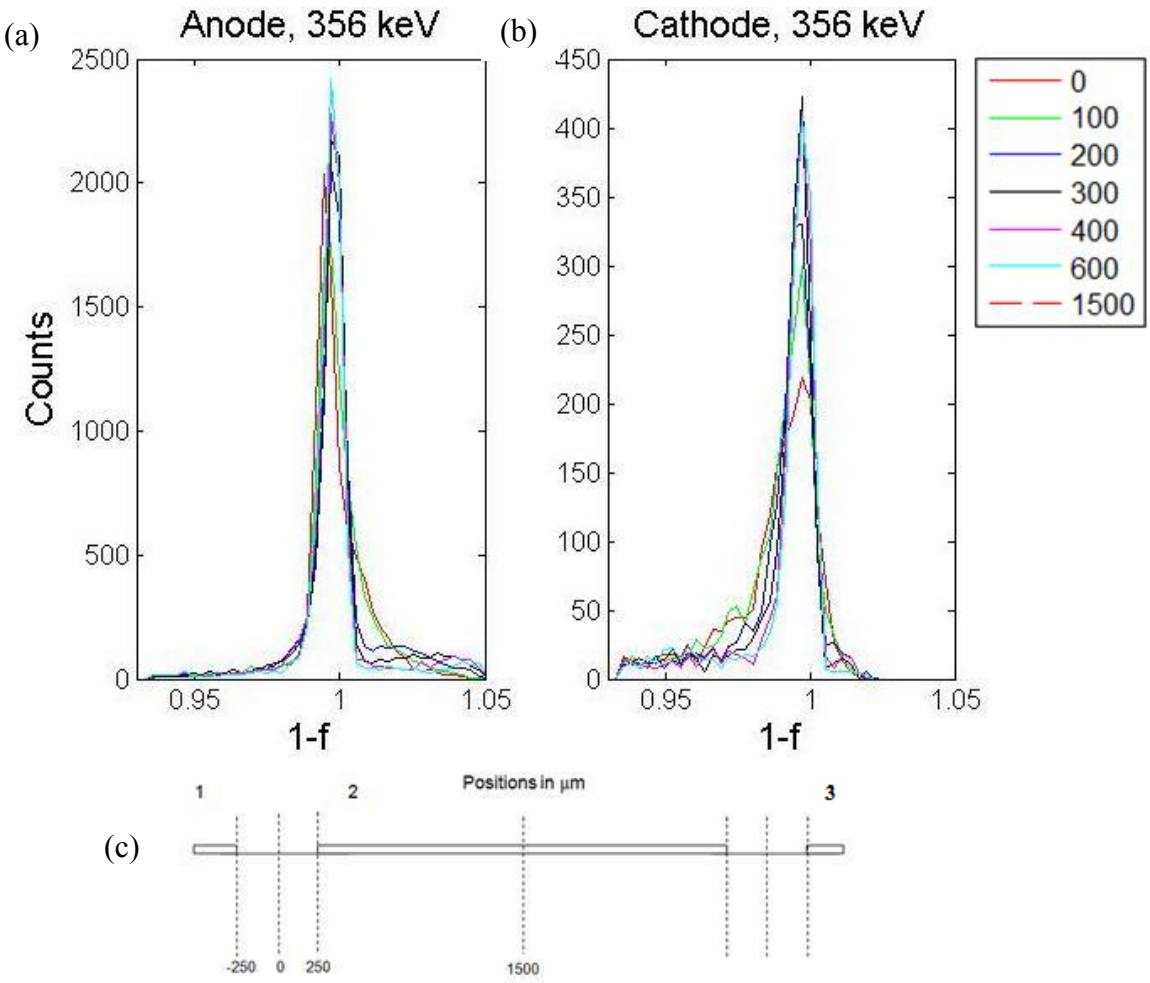

Fig. 36. Charge loss distributions after energy correction (Eqn. 15) is applied to collimated measurements shown in Fig. 30. Refer to caption for Fig. 30 for explanations of (a), (b), and (c).

IV.B.3.1. Collimated beam results

When Eqn. 15 is applied to the data shown in Fig. 30, the result is shown in Fig. 36. As in Fig. 30, Fig. 36(a) and Fig. 36(b) correspond to anode and cathode sides, respectively. Charge loss correction causes $f_{j\,p}$ of each distribution $S_j(E)$ to shift into $S^{anode}_{j=1500\,\mu m}(E)$ on the anode side and $S^{cathode}_{j=1500\,\mu m}(E)$ on the cathode side. After corrections are applied, note in Fig. 36 that $f_{j\,p} \sim 1$ for all j on anode and cathode sides.

To quantify the results, Fig. 37 and Fig. 38 give values of $\overline{f}_j$ and f_{rms} before and after correction, as indicated in figure legends. Gamma ray energy and detector side are given in figure headings. Referring to Fig. 37, it is evident that charge loss correction brings $\overline{f}_j$ closer to zero for all j. The greatest change in the average is visible on the anode side, where $\overline{f}_j$ is highest before correction. Referring to Fig. 38, charge loss correction always reduces f_{rms} for all j in the gap. Again, the change is most significant on the anode side. However, there is some tradeoff when j is in-strip on the anode side, where f_{rms} is slightly higher after correction. And, although f_{rms} is improved at the gap center, the base of some peaks is still broader than desired, as seen in Fig. 36. On the cathode side, the base of the peak broadens in the opposite direction compared to the anode side. On either side, the broadening increases as the gap center is approached. This undesired effect may result from the increased sensitivity as the gap center is approached to fluctuations in the charge cloud geometries.

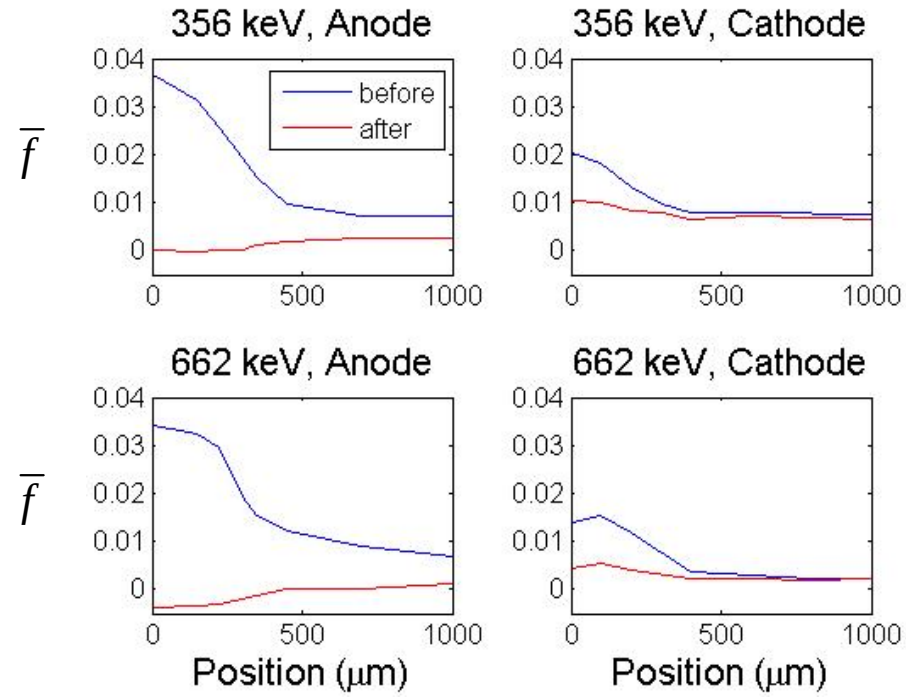

Fig. 37. Average charge loss fraction $\overline{f}$ before and after energy correction is applied to collimated measurements. Gamma ray energy and detector side are given in figure headings.

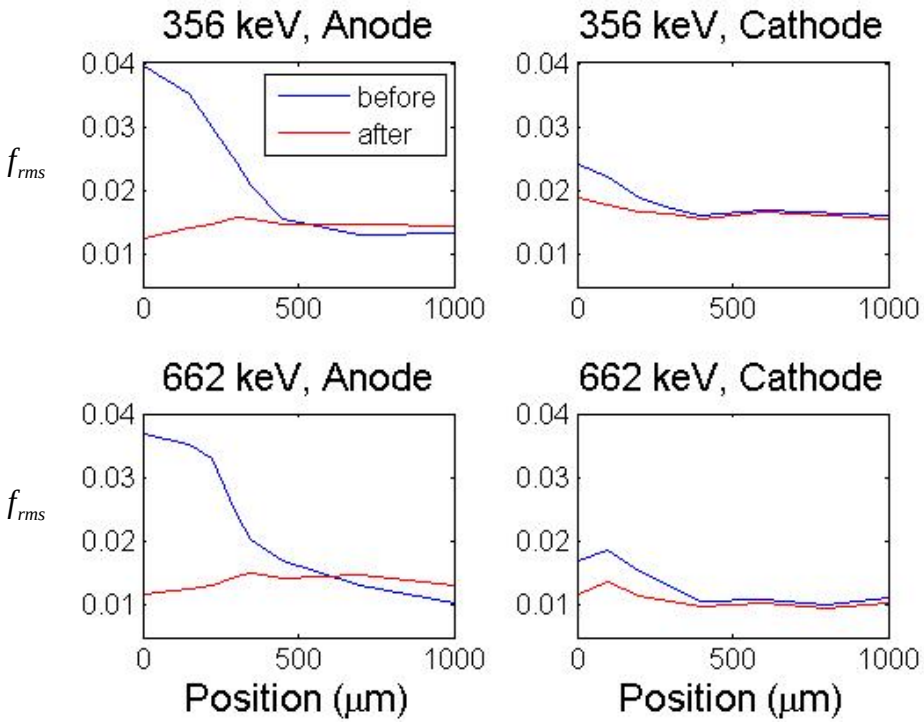

Fig. 38. RMS charge loss fraction f_{rms} before and after energy correction is applied to collimated measurements. Gamma ray energy and detector side are given in figure headings.

IV.B. 3.2.Flood field results

To best measure the effectiveness of charge loss corrections over a wide range of gamma ray energies, flood field measurements were collected from 6 sources. Charge loss corrections were performed at 60, 122, 356, 662, 835, and 1274 keV on the anode side. A subset of these measurements was also performed on the cathode side, where less charge loss is expected.

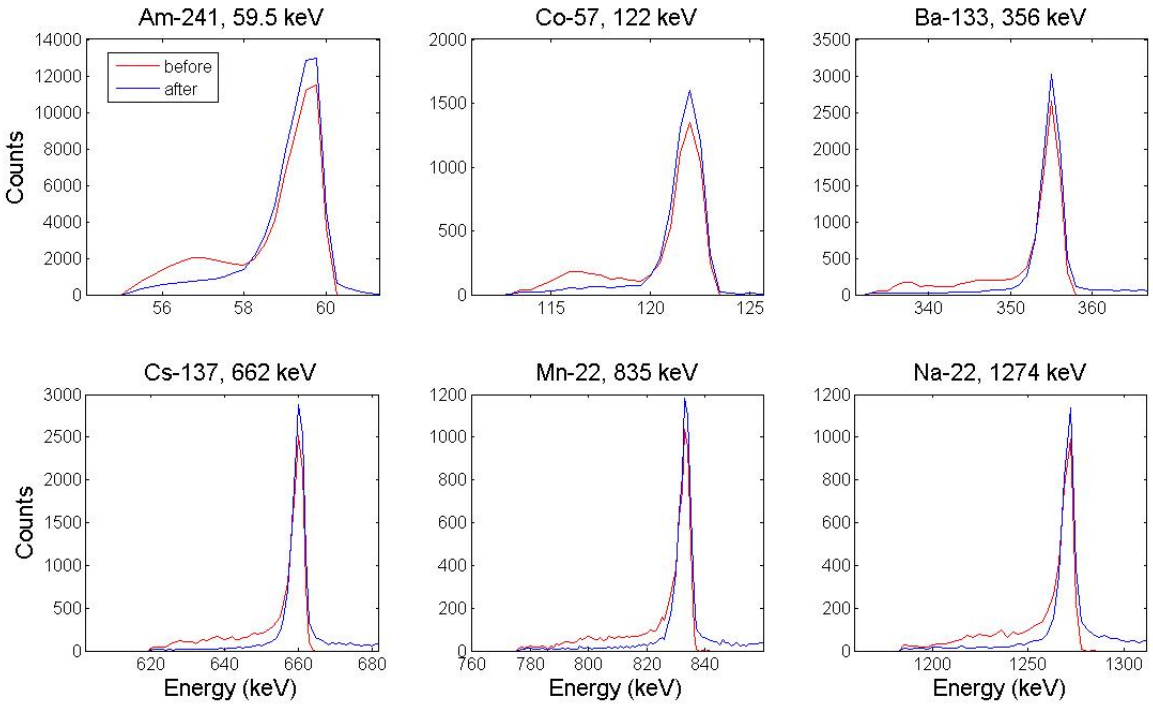

Fig. 39. Upon flood field irradiation by six gamma ray sources, as specified in figure headings, measurements of FWHM and peak counts before and after energy correction for SSIs on the anode side.

Anode side spectra from SSIs are shown in Fig. 39. As before, the spectra from two adjacent strips are summed together. To measure the increase in photopeak efficiency for a single strip, results are shown for a single gap correction. Thus, if a correction is performed for the gap in between strips 2 and strip 3, as in Fig. 36(c), data are collected only for a trigger on strip 2 or for coincidence triggers on 2 and 3. This restriction

eliminates those interactions that lose charge to the gap between strips 1 and 2, but do not cause triggers on both strips. To avoid overestimating the increase in photopeak efficiency due to charge loss correction, this charge loss is not corrected. This explains why the low energy tail, which is due to charge loss, doesn't completely vanish after the correction is applied. This effect is more significant at lower gamma ray energies, where a gap interaction is less likely to cause triggers on adjacent strips.

The FWHM and counts within each peak in Fig. 39 were measured before and after correction. While there is no appreciable change in FWHM, there is a significant increase in photopeak counts across all energies. The ratios of corrected-to-uncorrected photopeak counts for anode and cathode sides are given in Table I. The uncertainty in the ratio is estimated to be ± 0.02 due to the non-Gaussian form of some peaks.

Table I.
The ratios of corrected-to-uncorrected peak counts for anode and cathode sides. Only SSIs are selected.

	59.5 keV	*122 keV*	*356 keV*	*662 keV*	*835 keV*	*1274 keV*
Anode	1.17	1.18	1.12	1.14	1.10	1.14
Cathode	1.04		1.05	1.04		1.05

The increase in measured anode counts is nearly 1/6, which, as discussed, is the best that can be expected. There is little change in the energy resolution since the net effect is to move counts already below the full energy peak into the photopeak. Meanwhile, background due to partial energy deposition on each adjacent strip is reduced. The difference in the improvement between anode and cathode is likely the result of the

previously reported difference in charge loss between anode and cathode sides. As $\frac{E_\ell}{E_z}$ increases, carrier collection probability increases, so the maximum possible change in peak counts decreases from 1/6.

Referring to Fig. 39, the counts beyond any peak result from an overcorrection for certain events. This overcorrection may be due to increased sensitivity to charge cloud geometries at the gap center. The magnitude of the overcorrection increases with gamma ray gamma, as does charge cloud size. Alternatively, the overcorrection might be attributed to the presence of unresolved CCEs, which are indistinguishable from SSIs. CCEs require a smaller correction that SSIs because they lose less charge, as discussed in IV.A.5.1, so it is feasible that treating them like SSIs may result in overcorrection.

Chapter V

Inter-strip position interpolation

In this chapter, a novel measurement-based method for inter-strip interpolation is described. Emphasis is placed on interpolation of gap events on the anode side, where a greater fraction of events require this method due to higher charge loss to the gap. Since position determination is necessary for charge loss correction of CCEs, this method is discussed as well. Additionally, inter-strip interpolation results are compared with simulation.

V.A. Inter-strip interpolation method

The measurement-based method to determine inter-strip position employs Bayes' Theorem. For a set A, $S \equiv \bigcup_{i=1}^{N} A_i$, and $A_i \cap A_j = \varnothing$ for $i \neq j$, Bayes' Theorem states that the probability P that an event A_i has occurred given the occurrence of A is given by

$$P\left(A_i \middle| A\right) = \frac{P(A_i)P\left(A \middle| A_i\right)}{\sum_{j=1}^{N} P(A_j)P\left(A \middle| A_j\right)} \tag{16}$$

Thus, the parameters of an underlying distribution A_i can be estimated based on an observed distribution A.

The desired parameter to be estimated is the inter-strip position x_i of a gamma ray SSI event i of energy E_i when that interaction falls in between adjacent strips. A SSI falls between adjacent strips when 1) some measurable fraction of its charge carriers remain uncollected by the adjacent strips, or 2) it causes triggers on both adjacent strips. The observed distribution for i consists of measurements of $E_{1,i}$, $E_{2,i}$, and E_i. The measured quantities on adjacent strips 1 and 2 are $E_{1,i}$ and $E_{2,i}$. Assuming charge loss on only one detector side, the measured energy on the opposite side is E_i, where $E_i > (E_{1,i} + E_{2,i})$. Next, techniques to infer position from these observations are discussed.

V.A.1. Position inference from charge-splitting

One technique of inferring inter-strip position for a SSI event i is based upon the phenomenon of charge-splitting. Charge-splitting occurs when a charge cloud is close enough to a gap center that some fraction of its carriers is collected by both adjacent strips 1 and 2. For an event i, the charge-splitting ratio $r_i \equiv \frac{E_{1,i}}{E_{1,i} + E_{2,i}}$. This quantity extends from 0 to 1 as an interaction moves across the gap from strip 2 to strip 1, as shown in Fig. 8(c).

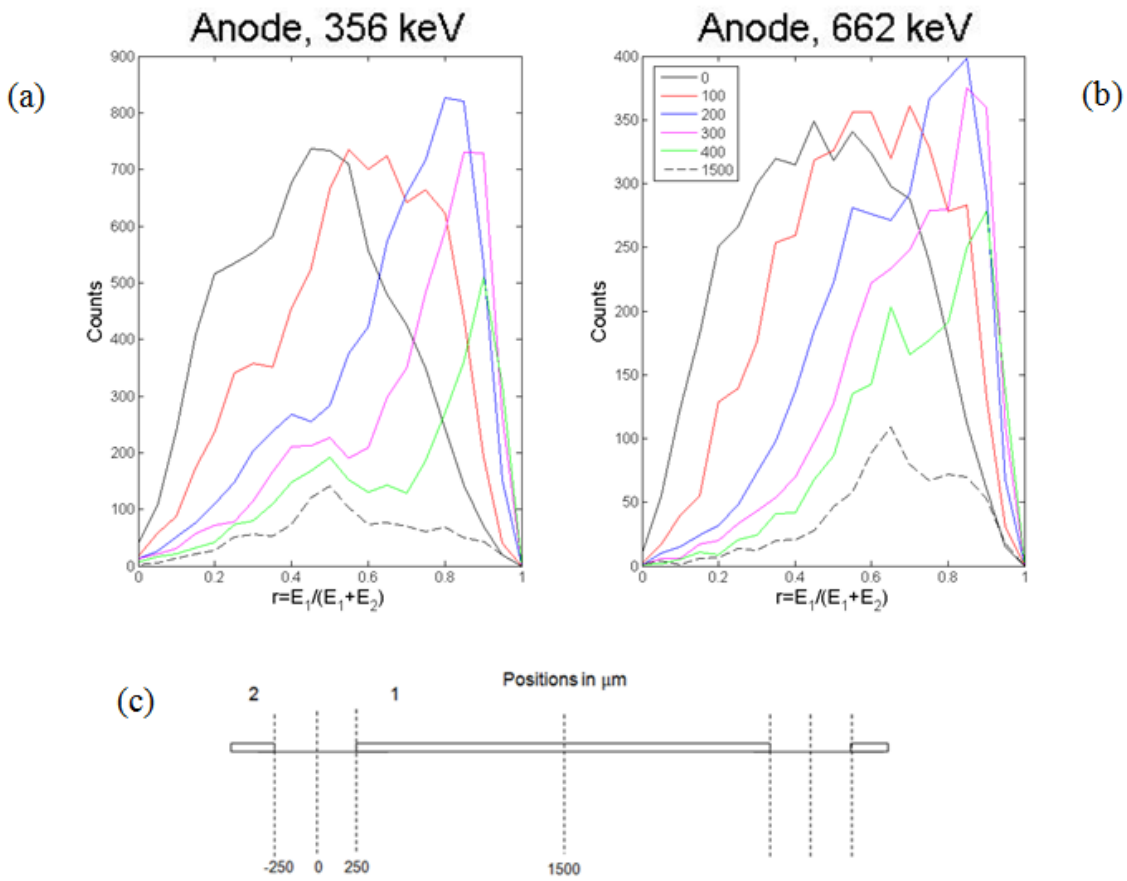

Fig. 40. Charge-splitting ratio r as a function of collimator position on the anode side for all SSI gap events.

Fig. 40 shows the charge-splitting ratio as a function of collimator position on the anode side for all SSI gap events. Fig. 40(a) shows the ratio at 356 keV. Fig. 40(b) shows the ratio at 662 keV. At the gap center, the most probable $r = 0.5$ because it is equally probable for carriers to be collected by either adjacent strip. The width of this distribution suggests that there is substantial position uncertainty. At a given energy, this uncertainty is due to variance in cloud size, orientation, and lateral spreading. As energy increases from 356 keV to 662 keV, the FWHM of each distribution increases due to an increase in cloud size. Each distribution shifts in the expected direction as the collimator

moves from the gap center into strip 1. As the collimator position shifts toward strip 1, counts decrease because the number of gap events decrease.

At the center of strip 1 (i.e., at 1500 μm), it appears that there are still SSIs that are also gap events, but this is not possible. The distribution at 1500 μm is due to a small fraction of CCEs that are not distinguishable from SSIs, called unresolved CCEs. As mentioned in IV.A.5.1, the separate interactions of these CCEs are close enough in depth that they trigger adjacent strips within 20 ns of each other. It is expected that the fraction of unresolved CCEs in an SSI data set is constant as lateral position changes. Thus, the distributions shown in Fig. 40 can be corrected by subtracting the distribution at 1500 μm from all the others. However, this was not done for the data shown in Fig. 40.

Comparing Fig. 40(a) and Fig. 40(b), notice that the distributions from unresolved CCEs peak at different values of r. This is because a 662 keV gamma ray which Compton scatters at 1500 μm deposits a greater fraction of its initial energy on average compared to a 356 keV gamma ray. At 356 keV, the Compton edge lies at 207 keV, which corresponds to an expected $r = 0.58$. At 662 keV, the Compton edge lies at 478 keV, which corresponds to an expected $r = 0.72$. The peaks in the distributions measured at 1500 μm are consistent with these calculated Compton edges.

V.A.2. Position inference from charge loss fraction

A second technique of inferring inter-strip position for a SSI event i is based upon measured charge loss. It is possible to correlate the charge loss fraction f_i for a gap event i with its inter-strip position. For example, referring to the anode distribution $S^{anode}_{j=0\,\mu m}(E)$ at 356 keV in Fig. 41(a), it is possible to correlate the distribution of f with three gap

regions. In Fig. 41(a), event energies have been divided by E_{peak} = 356 keV so that each photoelectric event i is binned according to its collection fraction $1-f_i$. Three charge collection regions are shown. Fig. 41(c) shows the three gap regions that roughly correspond to these three charge collection regions. Region 1 is in the gap center, Region 3 is near the strip edges, and Region 2 is in between.

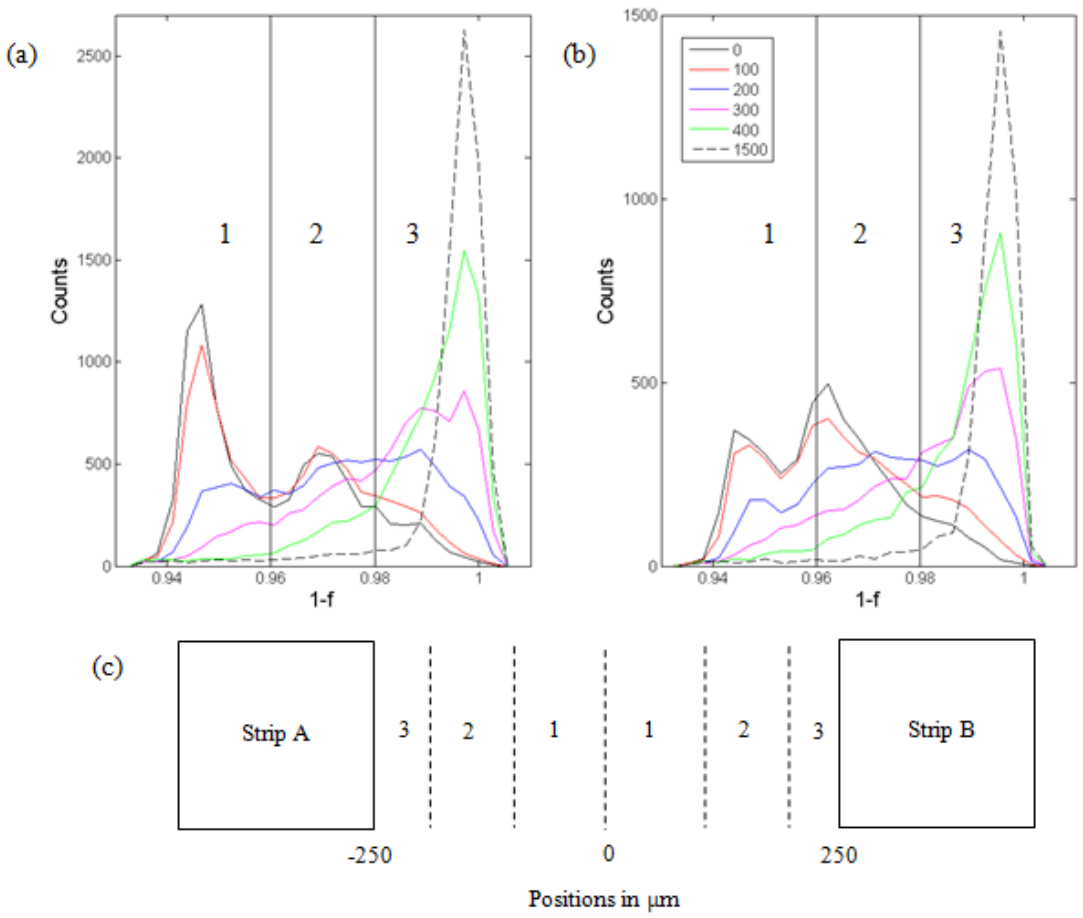

Fig. 41. (a) Anode distributions $S_j^{anode}(E)$ at 356 keV. Event energies have been divided by 356 keV so that each event i is binned according to its collection fraction $1-f_i$. (b) Cathode distributions $S_j^{cathode}(E)$ at 356 keV. Three charge collections are designated in (a) and (b). In (c), three gap regions are designated that roughly correspond to these three charge collection regions.

A gap event i which falls within the peak centered at $1-f = 0.945$ is likely to have originated in the gap center (Region 1), where charge loss is at a maximum. In this first region, $\frac{E_\ell}{E_z}$ is relatively weak, making charge collection by either adjacent strip less probable. Simulation results shown in Fig. 32 and discussed in IV.A.5.1 support this idea. In Fig. 41(a), the line separating Region 1 from Region 2 corresponds to the local minimum in the $S^{anode}_{j=0\,\mu m}(E)$ distribution.

Region 2 is centered at a second peak in $S^{anode}_{j=0\,\mu m}(E)$ at $1-f = 0.97$. An event may fall within this peak for one or more of the following reasons: (1) the photo-interaction was caused by a gamma ray originating toward the outer edge of the collimated beam, (2) the photoelectron happened to be directed more toward a strip, (3) a significant fraction of carriers in its charge cloud reached a region of higher $\frac{E_\ell}{E_z}$.

Fig. 41(b) shows the $S^{anode}_{j}(E)$ distributions at 662 keV. A greater fraction of events fall into Region 2 at 662 keV due to increased charge cloud spreading, as shown by simulation results in Fig. 32. While the size of the collimated beam is about the same, photoelectron range increases, as seen in Fig. 14, which may cause a higher fraction of carriers to reach a region of higher $\frac{E_\ell}{E_z}$, as shown in Fig. 15(c). This leads to improved collection efficiency at 662 keV compared to 356 keV.

The lower bound of Region 3 may be defined at the intersection of $S^{anode}_{j=400\,\mu m}(E)$ and $S^{anode}_{j=0\,\mu m}(E)$. Due to collimation, the events in the $S^{anode}_{j=400\,\mu m}(E)$ distribution which lose charge are likely to originate near a strip edge. The upper bound of the third region is not

well defined in Fig. 41. On an event-by-event basis, this upper bound is where the anode and cathode energies are equal. Above this upper bound, there is no charge loss, which means that f can no longer be used to infer inter-strip position.

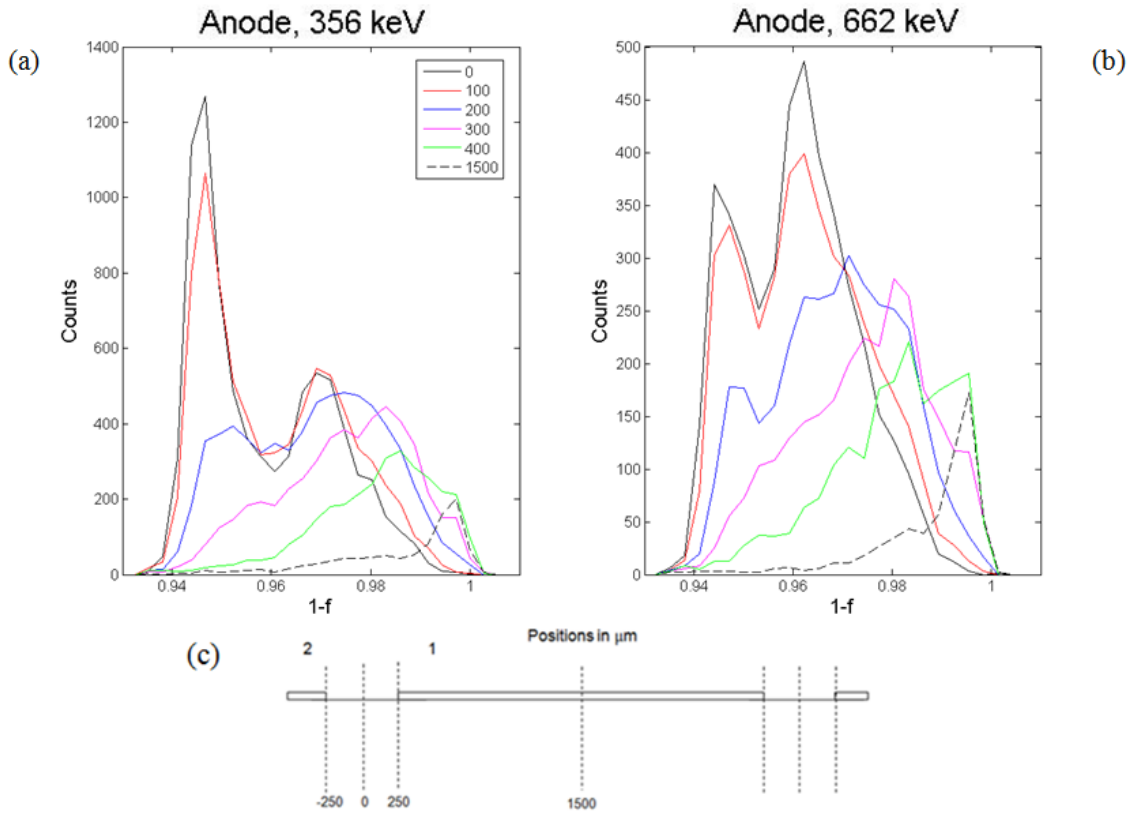

Fig. 42. Charge collection fraction $1-f$ as a function of collimator position on the anode side for all SSI gap events.

Fig. 42 shows the charge collection fraction $1-f$ as a function of collimator position on the anode side for all SSI gap events. Fig. 42(a) shows results at 356 keV. Fig. 42(b) shows results at 662 keV. Fig. 42(c) gives a 1D reference for the collimator positions indicated in figure legends. The upper bound on charge loss has been applied, and the event selection is the same as in Fig. 41. As in Fig. 41, when the collimator is at the center of strip 1 (i.e., at 1500 μm), it appears in Fig. 42 that there are SSIs which are also

gap events. However, these are unresolved CCEs. As before, the distributions in Fig. 42 can be corrected by subtracting the distribution at 1500 μm from all the others.

Consider unresolved CCEs which have 2 or 3 interactions, where all of these interactions do not occur in a gap. Compared to gap SSIs, these events are characterized by both higher collection fractions and *r* values consistent with the calculated Compton edge. Thus, they may be separated from SSIs on an event-by-event basis. However, if any interaction occurs in a gap, then separation from SSIs is not possible. Thus, charge loss enables the discrimination of some unresolved CCEs in post-processing.

V.A.3. Effect of gamma ray energy on position inference using f

Consider the use of 60, 356, or 662 keV gamma rays to deduce inter-strip position in a detector gap using the charge loss fraction f. Referring to the 356 keV distribution in Fig. 41, the maximum charge loss fraction for a SSI is $f_{\max} = 0.07$. Thus, the energy range sensitive to inter-strip position at 356 keV is $f_{\max} E_{peak} = 24.9\ keV$ while the FWHM of the peak (composed of $E_1 + E_2$) at 356 keV is ~2.4 keV. The inter-strip interpolation ratio $ISIR$ is defined as the ratio of the two quantities

$$ISIR = \frac{f_{\max} E_{peak}}{FWHM_{E_1+E_2}} \tag{17}$$

where $FWHM_{E_1+E_2}$ is the FWHM of a peak composed of $E_1 + E_2$. It is expected that

$$FWHM_{E_1+E_2} = \sqrt{2}\left(FWHM_{E_1}\right) = \sqrt{2}\left(FWHM_{E_2}\right)$$

At 356 keV, Eqn. 17 is used to find $ISIR = 10.4$. For comparison, the $ISIR$ at 60 keV and 662 keV are calculated and shown in Table II. The quantity $f_{\max}$ is a function of

detector geometry, so it remains the same. This idea is supported by the cathode measurements shown in the top row of Fig. 33, where counts are visible down to $1 - f_{\max} = 0.93$. Thus, the energy bands for which inter-strip interpolation are effective are 4.2 at 60 keV and 46.3 keV at 662 keV. The FWHM of a peak is ~1.5 keV at 60 keV and ~3.2 keV at 662 keV. So the calculated *ISIR* is 2.8 at 60 keV and 14.5 at 662 keV.

Table II.
Inter-strip Interpolation Ratios at 3 gamma ray energies

	60 keV	*356 keV*	*662 keV*
$f_{\max}$	0.07	0.07	0.07
$f_{\max} E_{peak}$	4.2 keV	24.9 keV	46.3 keV
$FWHM_{E_1+E_2}$	1.5 keV	2.4 keV	3.2 keV
ISIR	2.8	10.4	14.5

From the standpoint of *ISIR*, 662 keV seems like the optimal choice to deduce inter-strip position. However, gamma ray energy affects charge cloud size, as observed in Fig. 14, which also has an effect on inter-strip position inference. This effect is further explored in subsequent sections.

V.A.4. Bayesian method for inter-strip interpolation of SSIs

Two techniques to infer inter-strip position for a SSI gap event *i* have been discussed. For each event in a data set, let the measured charge-splitting ratio r_i and the measured

charge collection fraction $1-f_i=\frac{E_{1,i}+E_{2,i}}{E_i}$ be random variables. These random variables are observed for each *i* of the data sets taken at 356 keV and 662 keV. For either data set, the mode and probability interval of the inter-strip position x_i for *i* is given by

$$P\left(x_i\middle|r,1-f\right)=\frac{P(x_i)P\left(r,1-f\middle|x_i\right)}{\sum_{j=1}^{N}P(x_j)P\left(r,1-f\middle|x_j\right)} \tag{18}$$

where x_j from $j=1,2,...N$ are the collimated positions. Each of these collimated positions is 100 μm apart. Considering that the collimated beam has FWHM=56 μm at 356 keV and FWHM=68 μm at 662 keV (from IV.A.3), it was estimated that $P(x_j)=1.0$ at the collimated position and zero elsewhere.

On the anode side, measurements of the condition probability $P\left(r,1-f\middle|x_j\right)$ at the gap center are shown in Fig. 43. The irradiation energies are indicated by figure headings. The bottom row shows a top view of the same information presented in the top row. At each energy, the most probable measurements are $1-f=0.945$ and $r=0.5$. At 662 keV, the variance from these most probable measurements is greater due to larger charge cloud size. In the top row, this causes the observed reduction in peak height at 662 keV compared to 356 keV. In the bottom row, the variance about the most probable measurements is best observed.

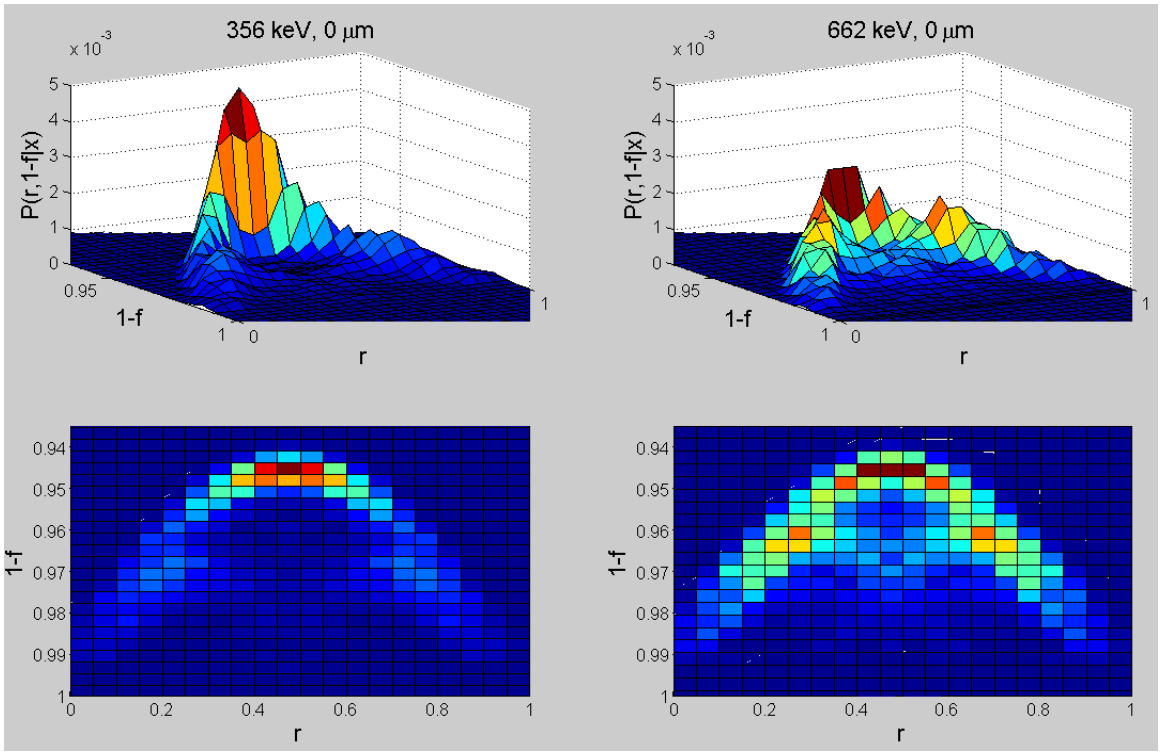

Fig. 43. Measurements of the condition probability $P\left(r,1-f\left|x_j\right.\right)$ at the gap center. Irradiation energies are indicated by column headings. The bottom row is a top view of the top row, where dark blue indicates a region of lowest counts and brown indicates a region of highest counts.

Fig. 44 shows $P\left(r,1-f\left|x_j\right.\right)$ at 356 keV on the anode side at collimated positions from 100 μm to 600 μm. The conditional probability at 662 keV looks similar. In each case, the results on the opposite side of the gap are symmetric. As the collimated source approaches strip 1, both r and $1-f$ increase toward 1, as they do in Fig. 40 and Fig. 42. Additionally, the distribution due to unresolved CCEs shifts out toward $r=0.58$ and $1-f=1$. Although true gap counts decrease toward zero at 600 μm, the counts due to unresolved CCEs remain because they are independent of lateral position. As mentioned in Section A.2, this phenomenon can allow for the separation of some unresolved CCEs on an event-by-event basis at both 356 keV and 662 keV on the anode side. However, the probability distributions shown in Fig. 44 were not altered to exclude unresolved

CCEs. The use of Eqn. 18 for inter-strip interpolation of SSIs is addressed in C.2 and C.3.

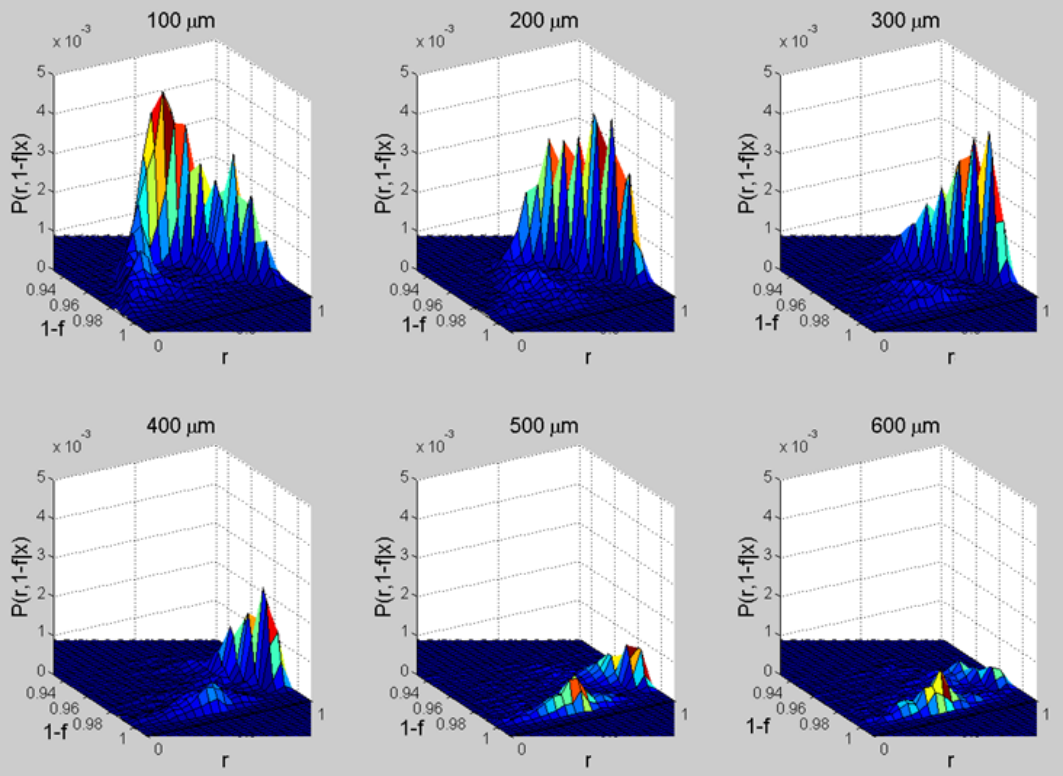

Fig. 44. Conditional probability at 356 keV on the anode side at collimated positions given by plot headings.

V.A.5. Ideal detector response for inter-strip position interpolation

For a detector that was ideal for inter-strip position interpolation, there would be a 1-to-1 relationship between gap position x and the measured set $\{r_i, 1-f_i\}$. Thus, if SSI event i were to interact at lateral position x_j in the gap, then $P\left(r_j, 1-f_j \middle| x_i\right)$ would be equal to 1 when $x_i = x_j$ and zero for every other value of x, i.e., $P\left(r_j, 1-f_j \middle| x_i\right) = \delta(x_i - x_j)$. Referring back to the bottom row in Fig. 43, the detector response is shown for 356 keV or 662 keV interactions near the gap center. Comparing these two energies, a larger cloud size is one factor that removes the UM detector from

the ideal case. In the ideal case, envisioned in Fig. 45, there would be a single brown pixel (top left corner), corresponding to a delta function, which would move from left to right along a semi-circle as x_j moved laterally from the gap center to strip 1. Every other pixel would be shaded dark blue. This effect would be symmetric about the gap center. In this ideal case, charge loss is not undesirable: if the measured set $\{r_i, 1-f_i\}$ is unique at each x_j, then it is possible to implement an ideal charge loss correction such that detector energy resolution and efficiency is unaffected by charge loss. However, the probability of a single interaction losing charge on both detector sides must be improbable. Furthermore, since the pixel size along each axis in Fig. 45 is determined by energy resolution, a detector with ideal energy resolution is required in order to obtain ideal inter-strip position resolution.

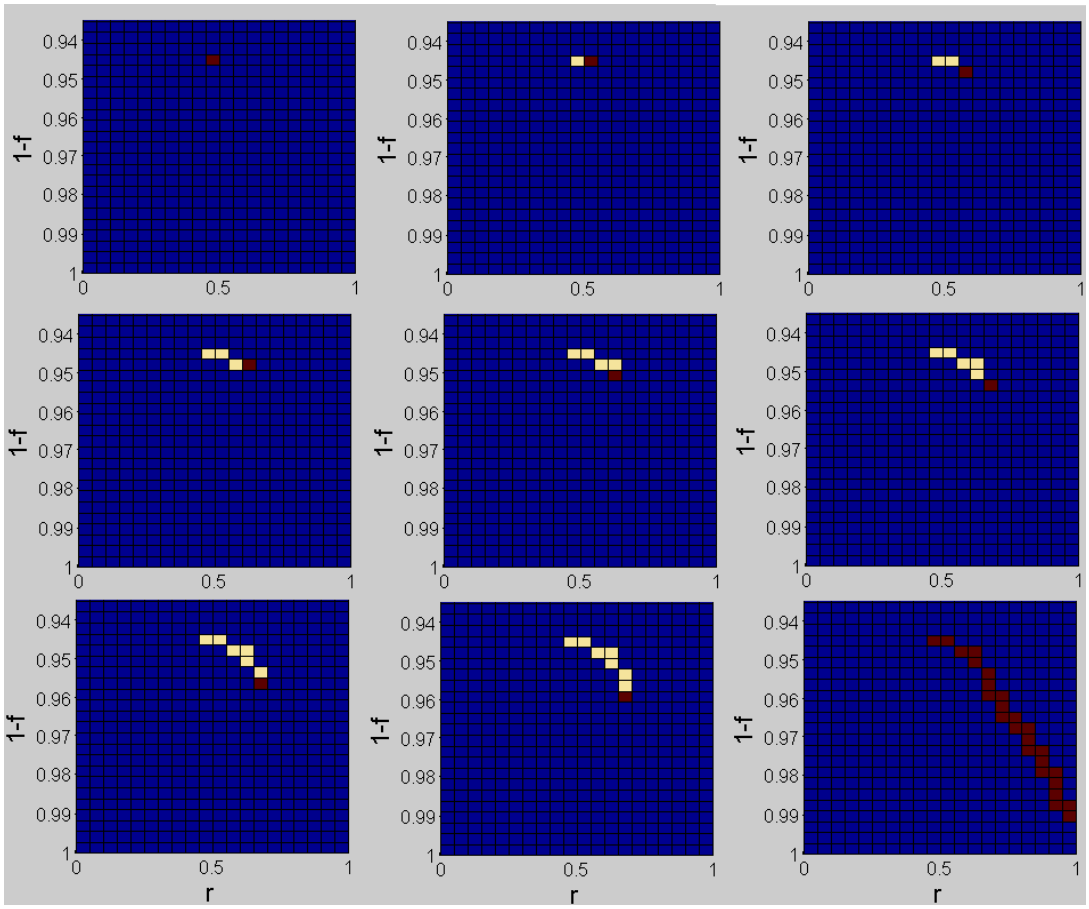

Fig. 45. In the ideal case, there would be a single brown pixel (upper left corner) which would move from left to right along a semi-circle as inter-strip position moved from the gap center to strip 1. The brown pixel represents a delta function, the dark blue pixels show the region where $P(r,1-f|x)=0$, and the light pixels are for perspective. At the lower right, the response for every lateral position is shown.

V.B. Inter-strip interpolation results for SSIs

In the following sections, inter-strip interpolation results for are discussed for SSIs that fall in the gap with respect to the anode side (Section B.1) or the cathode side (Section B.2).

V.B.1. Anode side interpolation of SSIs

Fig. 46 gives $P(x|r,1-f)$ for a SSI gap event i where the measured $1-f_i$ is given in the figure heading and the measured r_i is selected from the figure as well. Results are shown from the anode data set at 356 keV. As the measured charge collection fraction

$1-f_i$ increases from $1-f_{\max}=0.93$ toward 1, the mode of $P(x\,|\,r,1-f)$ moves from the gap center toward strip edges. As discussed in A.2, this response is expected. The probability interval, measured as the FWHM of $P(x\,|\,r,1-f)$, appears to increase as well. As r increases from 0.5 toward 1 or 0, the mode of $P(x\,|\,r,1-f)$ moves from the gap center toward strip edges. This behavior is also expected, as discussed in A.1. For the anode data set at 662 keV (not pictured), the detector response appears similar to that shown in Fig. 46, although at slightly higher values of $1-f_i$. This difference is expected: for the same gap position, the charge collection fraction is higher due to larger cloud size.

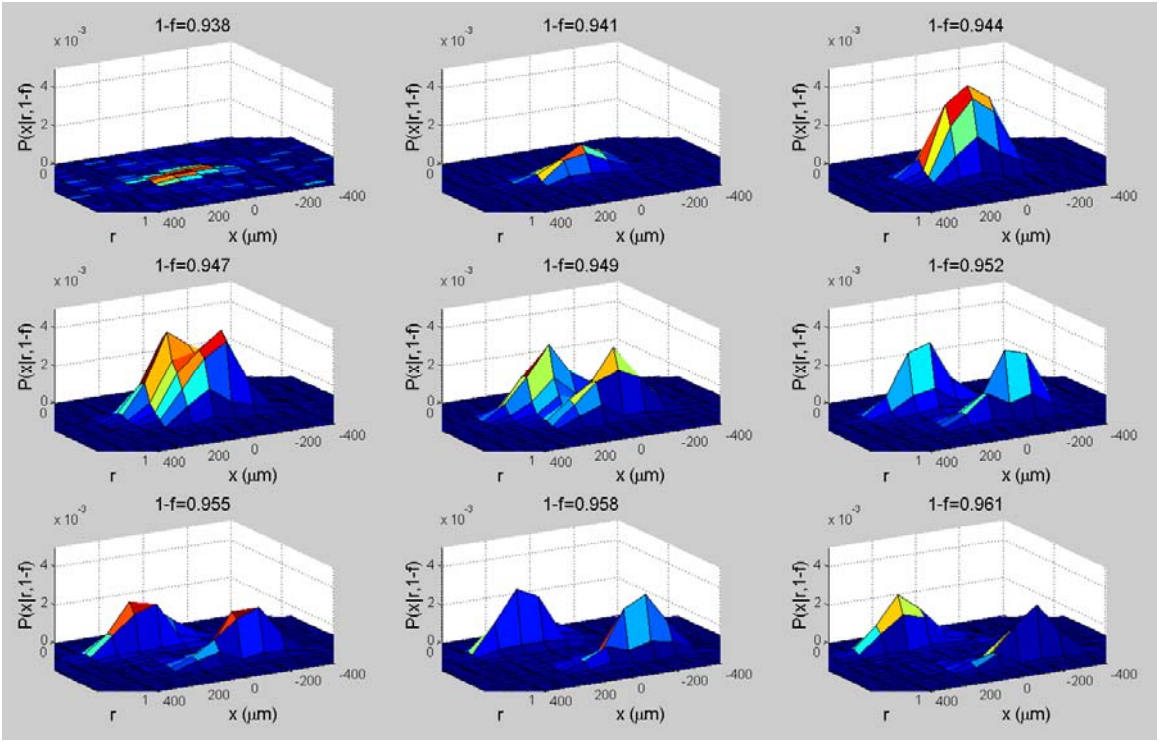

Fig. 46. The conditional probability $P(x\,|\,r,1-f)$ for a SSI event i where the measured $1-f_i$ is given in the figure heading and the measured r_i is selected from the figure. The anode data set at 356 keV was used.

In Bayesian analysis, the mode of the distribution is used as the parameter estimate. Here, the parameter to be estimated is the inter-strip position. Thus, Eqn. 18 was used to determine the mode, now referred to as the inter-strip position x, for each measured event at every collimator position j in the gap vicinity. For each collimator position, x was binned for all events. The result at 356 keV and 662 keV is shown in Fig. 47, where energies are indicated by figure headings. Collimator positions are given in each legend. At each energy, the most probable value of x for distributions at 0, 100, and 200 μm agrees with these collimator positions. As the strip edge, located at 250 μm, is approached, counts decrease and the asymmetry of each distribution increases because a greater fraction of events are fully collected by the adjacent strip.

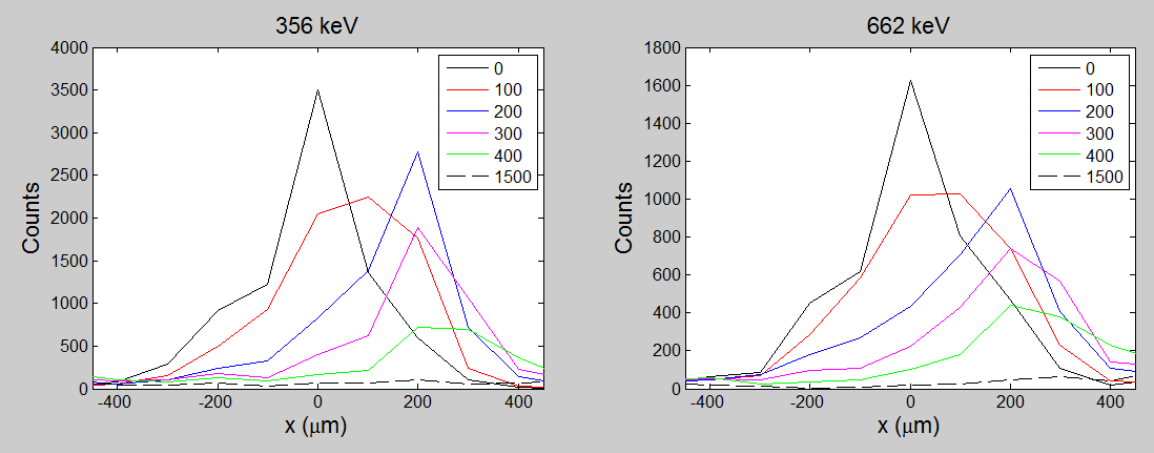

Fig. 47. The inter-strip position x binned for all events at each collimator position given in figure legends. The analysis was performed on the anode data set at 356 keV and 662 keV.

In Fig. 47, the counts at collimator position 1500 μm are due to unresolved CCEs. At 1500 μm, this effect is relatively insignificant because SSI loss events where the difference in charge collection between sides is less than 1% have been excluded, excluding many unresolved CCEs. As discussed in Sections A.1 and A.2, it is presumed

that more sophisticated techniques to exclude unresolved CCEs will exclude events based on correlation between measured charge loss and charge-splitting, but this been not been done for the results shown in Fig. 47.

The measured $FWHM_{meas,j,E}$ of a distribution at a given collimated position j is indicative of both the spreading of the incident beam and the position resolution at j. Thus, the position resolution $FWHM_{j,E}$ at j for a measured energy E at collimated position j is given by

$$FWHM_{j,E} = \sqrt{FWHM^2_{meas,j,E} - FWHM^2_{beam,E}} \tag{19}$$

where $FWHM_{beam,E}$ is the FWHM due to the spreading of the incident beam. All terms are dependent upon the gamma ray energy.

The calculation of the terms in Eqn. 19 is shown in Table III for all positions j in the gap. The calculated values for $FWHM_{beam,E}$ were given in IV.A.3. To calculate $FWHM_{meas,j,E}$, Lorentzian distributions of the following form were fit to the distributions shown in Fig. 47

$$L(x) = \frac{1}{\pi} C \frac{\frac{1}{2}\Gamma}{\left(x - x_o\right)^2 + \left(\frac{1}{2}\Gamma\right)^2} \tag{20}$$

where x_o is the center, Γ is the FWHM, and C is a constant allowing for amplitude scaling. This function was selected over a Gaussian distribution because it tended to produce a better fit to data at the gap center. The fits at 356 keV and 662 keV are shown by the solid lines in Fig. 48. The calculated $FWHM^{Lorentzian}_{meas,j,E}$ of each distribution is given

in Table III along with the 95% confidence interval in parentheses below. Each distribution was also fit with a cubic spline for comparison, and the calculated $FWHM_{meas,j,E}^{Spline}$ for each is given in Table III as well. In the last row, position resolution was tabulated from Eqn. 19 using the higher value of $FWHM_{meas,j,E}$.

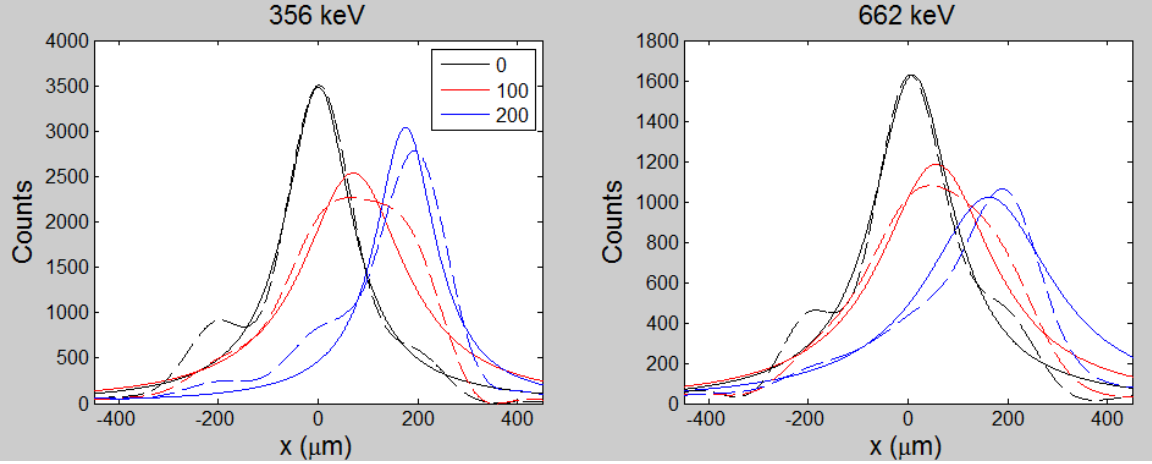

Fig. 48. Lorentzian (solid lines) and cubic spline (dashed lines) fits to the distributions in Fig. 47. Collimator positions are indicated in the figure legend.

Referring to Table III, position resolution may be degraded on the anode side due to the presence of unresolved CCEs. For these CCEs, the first interaction is constrained to occur in a gap, but the subsequent interaction is recorded underneath an adjacent strip. Referring back to Fig. 32, these CCEs are not confused with SSIs at 0 μm because CCEs at the gap center always have higher values of $1-f$ compared to SSIs at the gap center. Instead, these CCEs are incorrectly interpolated as SSIs that lie closer than they should to the strip which recorded the second interaction. While it is possible to distinguish in-strip unresolved CCEs from SSI gap events, as discussed previously, it is not possible to discriminate unresolved CCE gap events from SSI gap events because both lose charge.

Based upon the calculated position resolution at 356 keV, this inter-strip interpolation method allows interactions nearer to the gap edges to be distinguished from interactions occurring at the gap center. Thus, the 500 μm gap is roughly divisible into three separate position bins at 356 keV. At 662 keV, the gap is roughly divisible into only two position bins. This degraded inter-strip position resolution at 662 keV compared to 356 keV is attributed to increased charge cloud size and spreading at 662 keV. In the UM detector, it appears that charge cloud size more significantly affects inter-strip position resolution than *ISIR* (cf. Eqn 17) for electron energies in the hundreds of keV.

Table III.
Determination of position resolution for SSIs on the anode side

	356 keV			*662 keV*		
	0 μm	100 μm	200 μm	0 μm	100 μm	200 μm
$FWHM_{j,E,meas}^{Lorentzian}$	162	251	148	196	279	312
	(137,188)	(169,333)	(109,188)	(162,230)	(214,345)	(209,414)
$FWHM_{j,E,meas}^{Spline}$	160	321	169	179	349	233
$FWHM_{E,beam}$	56	56	56	68	68	68
$FWHM_{j,E}$	152	316	159	183	342	305

V.B.2. Cathode side interpolation of SSIs

Next, inter-strip interpolation was implemented using the data set on the cathode side at 356 keV. Fig. 49 shows $P(x \mid r, 1-f)$ for a SSI event i where measured $1-f_i$ is given in the figure heading and the measured r_i is selected from the figure as well. Only the

results for selected measurements of $1-f_i$ are shown. The detector response is similar to that described for the anode side (cf. Fig. 46) in Section B.1. The main difference is that the charge collection fraction $1-f_i$ is higher at the cathode side compared to the anode side. The collection fraction is higher still for the data set on the cathode side at 662 keV compared to 356 keV.

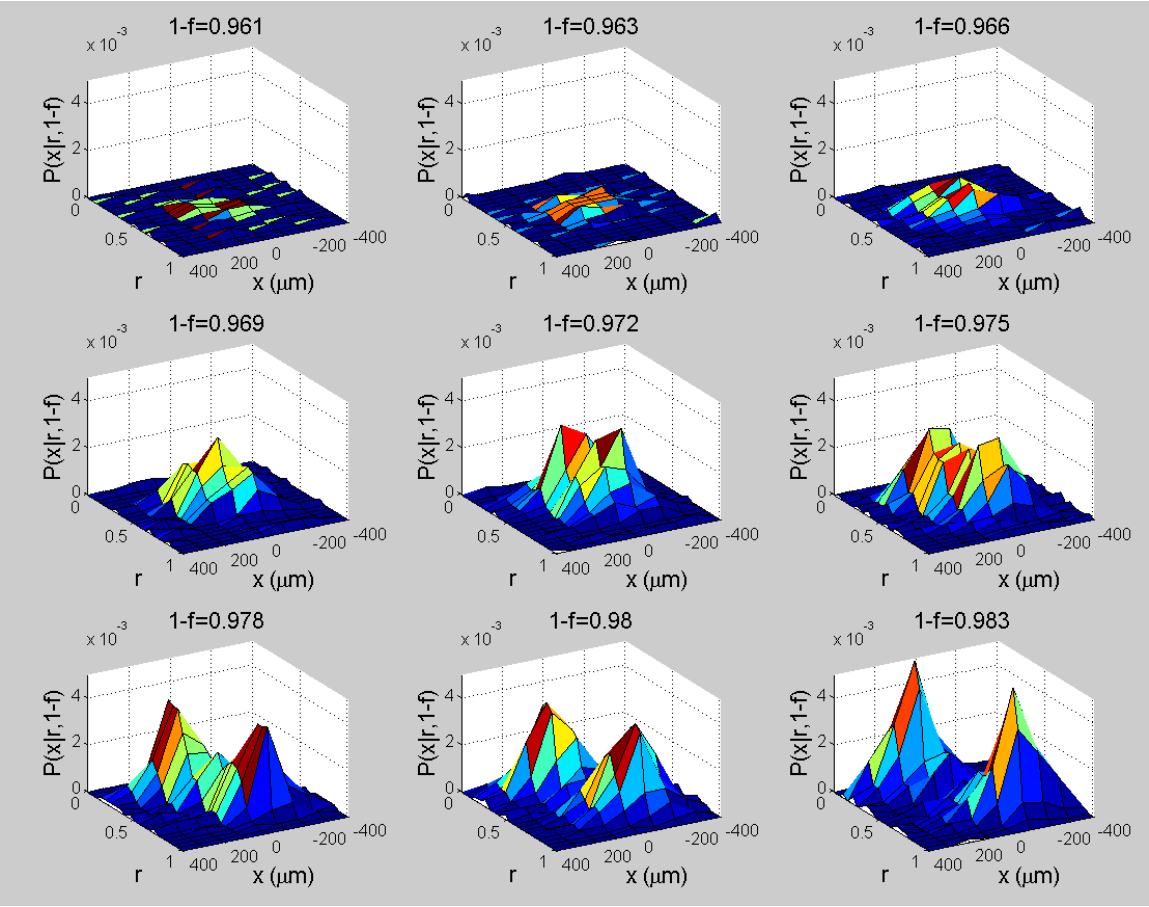

Fig. 49. The conditional probability $P(x \mid r, 1-f)$ for a SSI event i where the measured $1-f_i$ is given in the figure heading and the measured r_i is selected from the figure. The cathode data set at 356 keV was used.

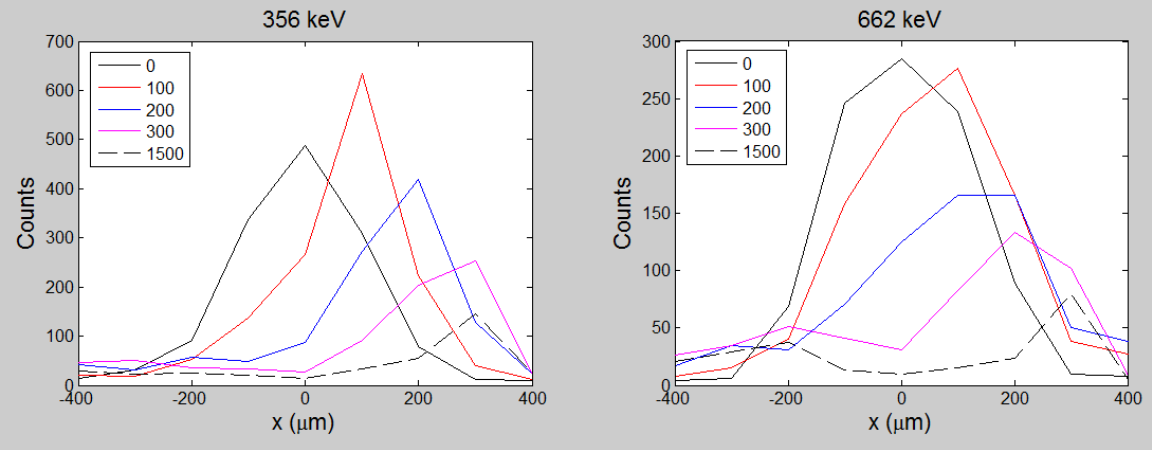

Fig. 50. The inter-strip position x binned for all events at each collimator position given in figure legends. The analysis was performed on the cathode data set at 356 keV and 662 keV.

Next, Eqn. 18 was used to determine the inter-strip position x for each measured event at every position j in the gap vicinity. The histograms at 356 keV and 662 keV are shown in Fig. 50. Collimator positions are given in figure legends. At both energies, the most probable value of x for distributions at 0, 100 and 200 μm agrees with these collimator positions. As the strip edge, located at 250 μm, is approached, counts decrease because a greater fraction of events are fully collected by the adjacent strip. The counts at collimator position 1500 μm are due to unresolved CCEs. These events are more significant at the cathode side compared to the anode side because a smaller fraction of unresolved CCEs have been excluded. A smaller fraction has been excluded because the charge collection fraction is higher for all events at the cathode side, making discrimination less effective. In the UM detector, increased charge loss provides an advantage here.

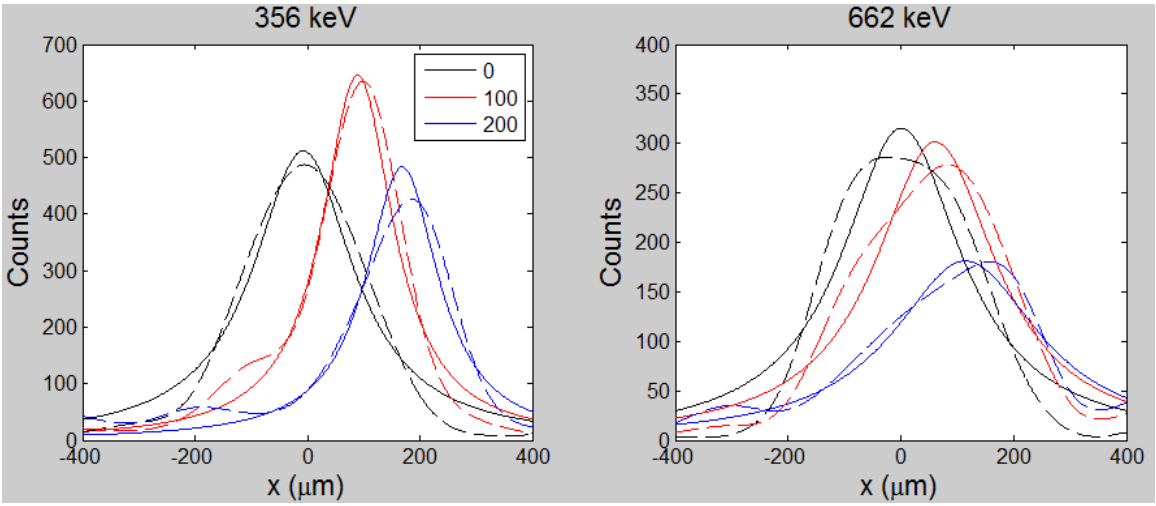

Fig. 51. Lorentzian (solid lines) and cubic spline (dashed lines) fits to the distributions in Fig. 50. Collimator positions are indicated in the figure legend.

To calculate $FWHM_{meas,j,E}$, Eqn. 20 was fit to the distributions shown in Fig. 50. The fits at 356 keV and 662 keV are shown by solid lines in Fig. 51. The calculated $FWHM_{meas,j,E}^{Lorentzian}$ of each distribution is given in Table IV along with the 95% confidence interval in parentheses below. Since some of the fits are poor, each distribution was also fit with a cubic spline, which yielded excellent agreement with data in every instance. These fits are shown by dashed lines in Fig. 51. The $FWHM_{meas,j,E}^{Spline}$ of the spline fits have been calculated and are shown in Table IV. Position resolution was calculated from Eqn. 19 using this latter measurement. As on the anode side, some degradation of position resolution is attributed to unresolved CCEs.

Table IV.
Determination of position resolution for SSIs on the cathode side

	356 keV			*662 keV*		
	0 μm	100 μm	200 μm	0 μm	100 μm	200 μm
$FWHM_{meas,j,E}^{Lorentzian}$	218	155	158	237	214	488
	(155,281)	(128,182)	(108,209)	(129,345)	(130,298)	(302,674)
$FWHM_{meas,j,E}^{Spline}$	259	167	197	322	332	328
$FWHM_{beam,E}$	56	56	56	68	68	68
$FWHM_{j,E}$	253	157	189	315	290	330

Based upon the calculated position resolution at 356 keV, this method allows interactions on one side of the gap to be distinguished from interactions occurring toward the opposite side. Thus, the 500 μm gap is roughly divisible into two separate position bins at 356 keV. At 662 keV, the calculated position resolution is not much less than the effective gap size. Thus, inter-strip position resolution is not possible at 662 keV on the cathode side. It is only possible to determine that an interaction occurred in the gap region. The tradeoff of this reduced dynamic range for inter-strip interpolation is improved charge collection efficiency resulting in greater intrinsic photopeak efficiency at 662 keV.

V.C. Inter-strip interpolation and energy correction for CCEs

Energy correction for CCEs that are also gap events was briefly discussed in IV.B.2 and the ability to resolve their positions shall be investigated in this section. In short, an energy correction cannot be performed until the relative positions of interactions are identified. The four possibilities for high and low energy interactions were depicted in Fig. 35, and are reproduced below in Fig. 52(a) for convenience.

In Section C.1, the energy-position dependence of Eqn. 15 will be exploited to select the most probable scenario. This selection will yield the information necessary to perform inter-strip position interpolation for the gap interaction, which is discussed in Section C.2. Finally, the results are checked against measurements using a collimated source in Section C.3.

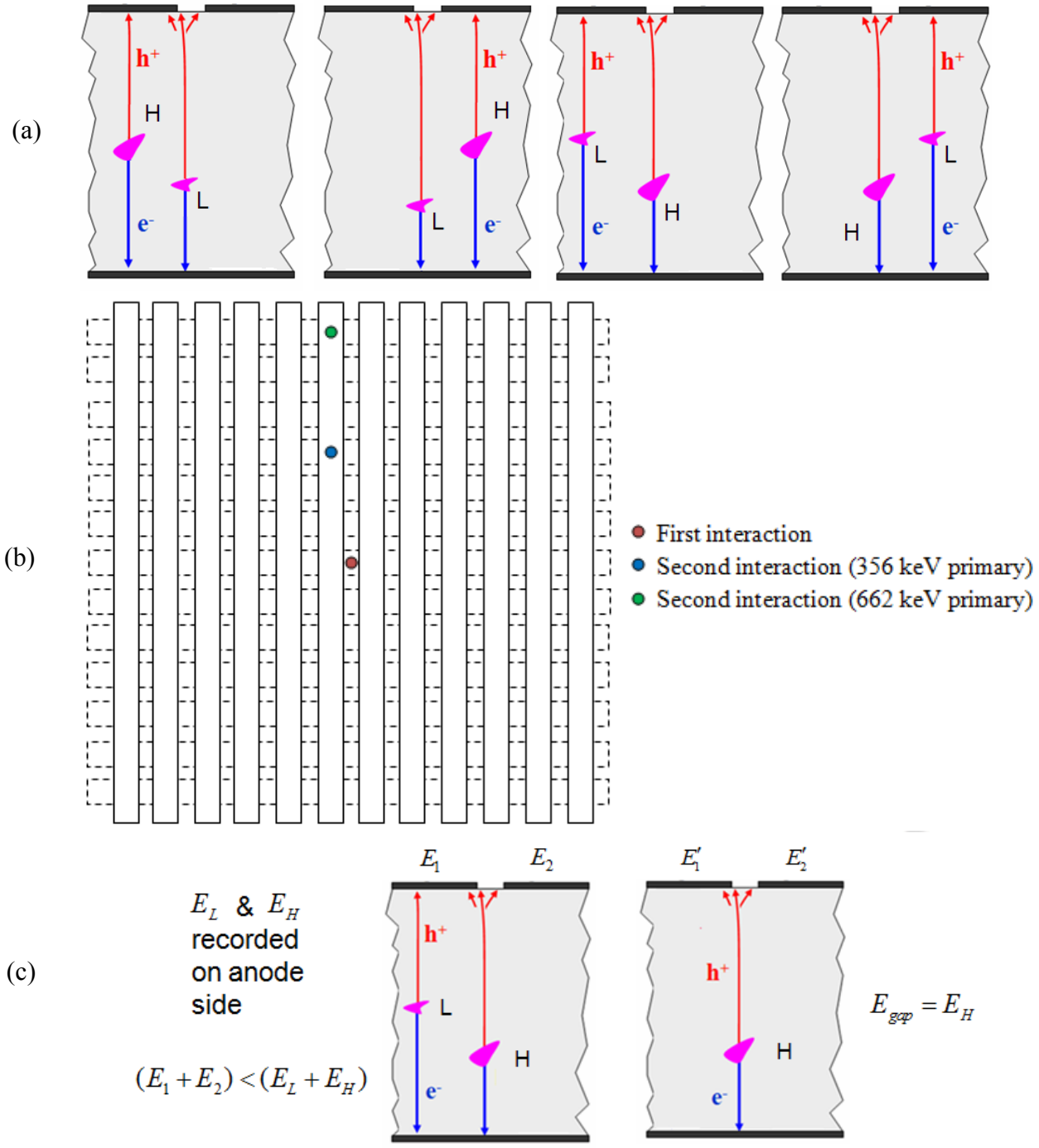

Fig. 52. For a CCE with 2 interactions, where one interaction loses charge to a gap in between cathode strips, (a) there are four possible scenarios for the relative positions of two higher (H) and lower (L) energy interactions. (b) A top view of the detector showing that interactions which are close together with respect to the cathode strips (oriented vertically) are unlikely to be close in proximity with respect to anode strips (oriented horizontally), especially as gamma ray energy increases. An example is shown in (c) where the higher energy interaction occurs in a gap and the lower energy interaction occurs beneath an adjacent strip. When the correct scenario from (a) is selected, $E_1' = E_1 - E_L$, $E_2' = E_2$, and $E_{gap} = E_H$. This scenario is chosen because $E_1' + E_2' + \Psi \approx E_{gap}$.

V.C.1. Scenario identification of CCEs through energy-position dependence

For the CCE method, charge loss on only one detector side is assumed, as discussed in IV.B for SSIs. Each possible scenario consists of a gap interaction and an in-strip interaction. Referring to Fig. 52(a), for example, it is presumed that for any scenario, one interaction loses charge to a gap on the cathode side and no other charge is lost on either detector side. Fig. 52(b) shows that interactions which are close together with respect to the cathode strips (oriented vertically) are unlikely to be in close proximity with respect to anode strips (oriented horizontally), especially as gamma ray energy increases. Based upon Compton kinematics and attenuation data in germanium [49], the mean free path for the average scattered gamma ray until phototelectric absorption is 13.7 mm when the primary gamma ray energy is 356 keV and 20.4 mm when the primary gamma ray energy is 662 keV.

Referring back to Fig. 52(a), the energies of the higher and lower energy interactions, E_L and E_H, must be recorded on two separate anode strips. On the cathode side, energies E_1 and E_2 are measured, where $(E_1 + E_2) < (E_L + E_H)$. It is presumed that E_L and E_H represent the true energies of the two interactions, where one of these is the in-strip interaction and the other is the gap interaction (with respect to the cathode side).

For each of the four possibilities, the energy of the assumed in-strip interaction (E_L or E_H) is subtracted from the measured energy of an assumed cathode strip that collects it (E_1 or E_2), yielding energies E_1' and E_2'. In any case, either $E_1' = E_1$ or $E_2' = E_2$. A proposed sequence is eliminated if the final energy on either strip (E_1' and E_2') is negative

or if the sum is over 7% less than expected, which indicates that charge loss is unable to account for the difference.

Next, Eqn. 15 is utilized, substituting E_1' and E_2' for E_1 and E_2, to determine the energy correction Ψ for the gap interaction

$$\Psi = k_1 E'_{\min} - \frac{k_2 E'^{\,2}_{\min}}{E_1' + E_2'}$$

for each remaining case, where $E'_{\min}$ is the minimum of E_1' and E_2'. For an ideal correction Ψ, the quantity $E_1' + E_2'$ should be less than E_{gap}, the energy of the gap interaction (E_H or E_L), by Ψ if the correct scenario is selected. Thus, the case with the lowest Δ is selected, where

$$\Delta = \left| E_{gap} - \left(E_1' + E_2' + \Psi \right) \right| \tag{21}$$

To illustrate, Fig. 52(c) shows an example where the higher energy interaction occurs in a gap and the lower energy interaction occurs beneath an adjacent strip. When the correct scenario from Fig. 52(a) is selected, $E_1' = E_1 - E_L$, $E_2' = E_2$, and $E_{gap} = E_H$. Effectively, the CCE event is altered such that it can now be treated like a SSI. Assuming an ideal charge loss correction Ψ, the correct scenario is chosen because $E_1' + E_2' + \Psi \approx E_{gap}$. Altogether, about 99% of 2-2 gap events avoid elimination, allowing for CCE charge loss correction and inter-strip interpolation, which are described in the next section.

V.C.2. Inter-strip interpolation method for CCE

For the CCE scenario selected for an event i in Section C.1, energies E'_{1i}, E'_{2i}, and $E_{gap\,i}$ are used to determine r_i and $1-f_i$, where

$$r_i = \frac{E'_{1i}}{E'_{1i} + E'_{2i}}$$

$$f_i = 1 - \frac{E'_{1i} + E'_{2i}}{E_{gap\,i}}$$

Inter-strip interpolation is then performed as before using Eqn. 18. Some results are presented and compared with those for SSIs in the next section.

V.C.3. Verification of CCE energy correction and position interpolation method

The CCE methods will be verified by showing: (1) the gap energy correction is consistent for SSIs and CCEs (in Section C.3.1), (2) measured fast signal behavior adjacent to firing strips is consistent with prediction of where high and low energy interactions are located (in Section C.3.2), and (3) the inter-strip interpolation method is consistent for SSIs and CCEs (in Section C.3.3).

Table V.
The ratios of corrected-to-uncorrected peak counts for anode and cathode sides. Only CCEs are selected.

	59.5 keV	*122 keV*	*356 keV*	*662 keV*	*835 keV*	*1274 keV*
Anode	1.05	1.08	1.17	1.15	1.15	1.16
Cathode	1.00		1.05	1.05		1.05

V.C.3.1. CCE gap energy correction results

Section IV.B.3.2 showed that the gap energy correction increased peak efficiency for detection of SSIs produced in flood field measurements. Now an energy correction is applied to the CCEs selected from the same data set. Anode results are shown in Fig. 53. The ratio of peak counts before and after correction is shown in Table V. As in Table I, the uncertainty in the ratio is estimated to be ±0.02.

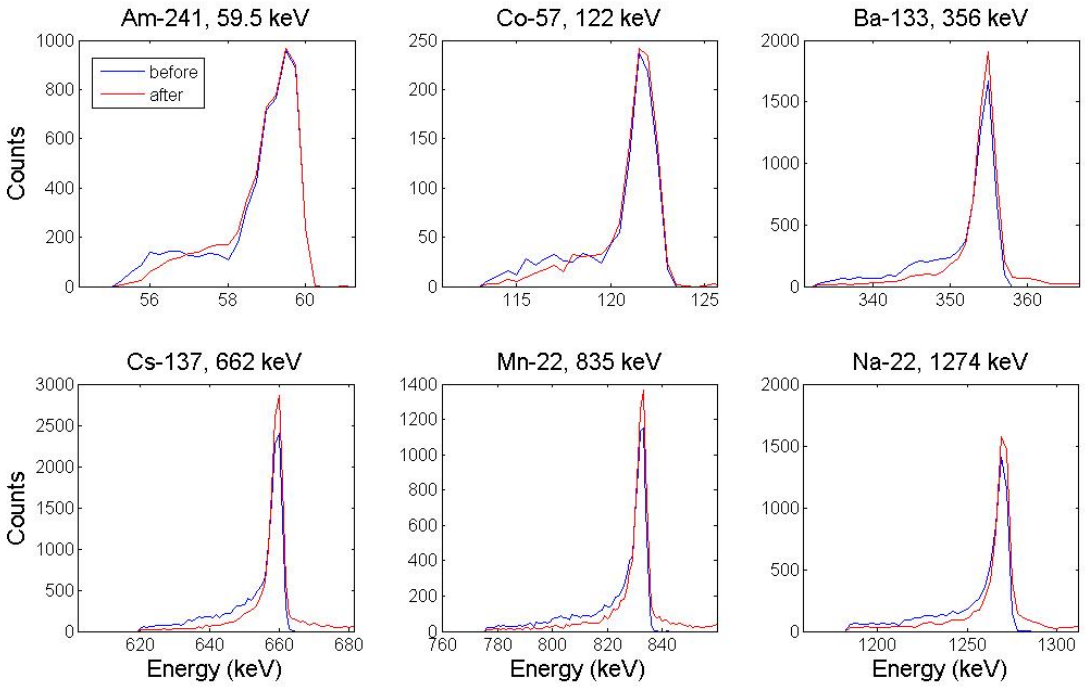

Figure 53. Upon flood field irradiation by six gamma ray sources, as specified in figure headings, measured spectra before and after energy correction for CCEs on the anode side.

The CCE and SSI corrections yield the same fractional improvement in peak counts at 356 keV and above. However, the correction makes less difference for CCEs compared to SSIs at 59.5 and 122 keV. This difference is attributed to lower signal-to-noise at these energies. Taking CCEs in Am-241, for example, the sum of the energies of each interaction adds to 59.5 keV. Low signal-to-noise results in some imprecision in

measuring the energy of the in-strip interaction and, consequently, in calculating E_1' and E_2'. Thus, the energy correction is adversely affected.

However, the measured fraction of CCEs, as shown in Fig. 54(a), is lower at 59.5 keV and 122 keV. This is mainly because the attenuation coefficient for Compton scattering $\mu_{Compton}$ in germanium [49], as shown in Fig. 54(b), is relatively low at these energies. At 60 keV, $\mu_{Compton}$ makes up only 6.6% of the total attenuation coefficient μ_{Total}, whereas at 122 keV, it makes up 35.5% of the total.

(a)

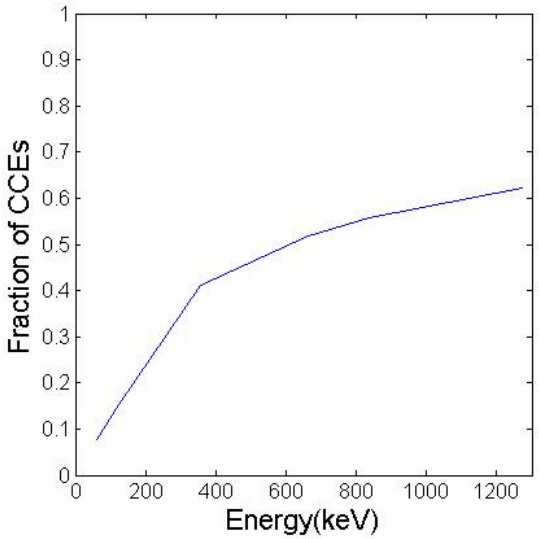

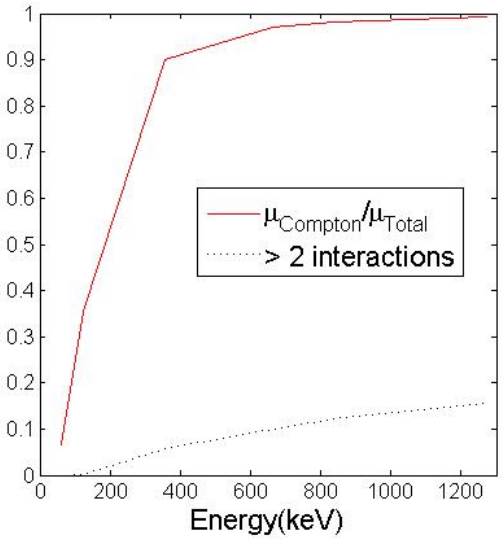

(b)

Fig. 54. (a) The measured fraction of CCEs as a function of gamma ray energy. (b) As indicated by the legend, the curves depict the ratio of the attenuation coefficents for Compton scattering to the total $\mu_{Compton}/\mu_{Total}$, and the measured fraction of CCEs consisting of more than two interactions.

The measured fraction of CCEs differs from $\frac{\mu_{Compton}}{\mu_{Total}}$ due to mean free path and strip pitch considerations. At low gamma ray energies, the total mean free path $\lambda_{Total} = \frac{1}{\mu_{Total}}$ of scattered gamma rays is low as well. Thus, the chance of two interactions within the

lateral bounds of one strip with respect to both detector sides increases. These Close Compton Events go undetected because they only trigger one strip on each detector side. At higher gamma ray energies, mean free path increases, and the chance of two interactions within the lateral bounds of two adjacent strips with respect to either detector side (i.e., a CCE) decreases. Thus, at high energies, the measured CCE fraction decreases, explaining why it is significantly less than $\frac{\mu_{Compton}}{\mu_{Total}}$.

Fig. 54(b) also shows the fraction of CCEs consisting of more than two interactions. Although $\frac{\mu_{Compton}}{\mu_{Total}}$ rises only gradually after about 600 keV, the CCE fraction increases more quickly due to the increase in the number of interactions. At 1274 keV, 15% of CCEs are composed of 3 interactions.

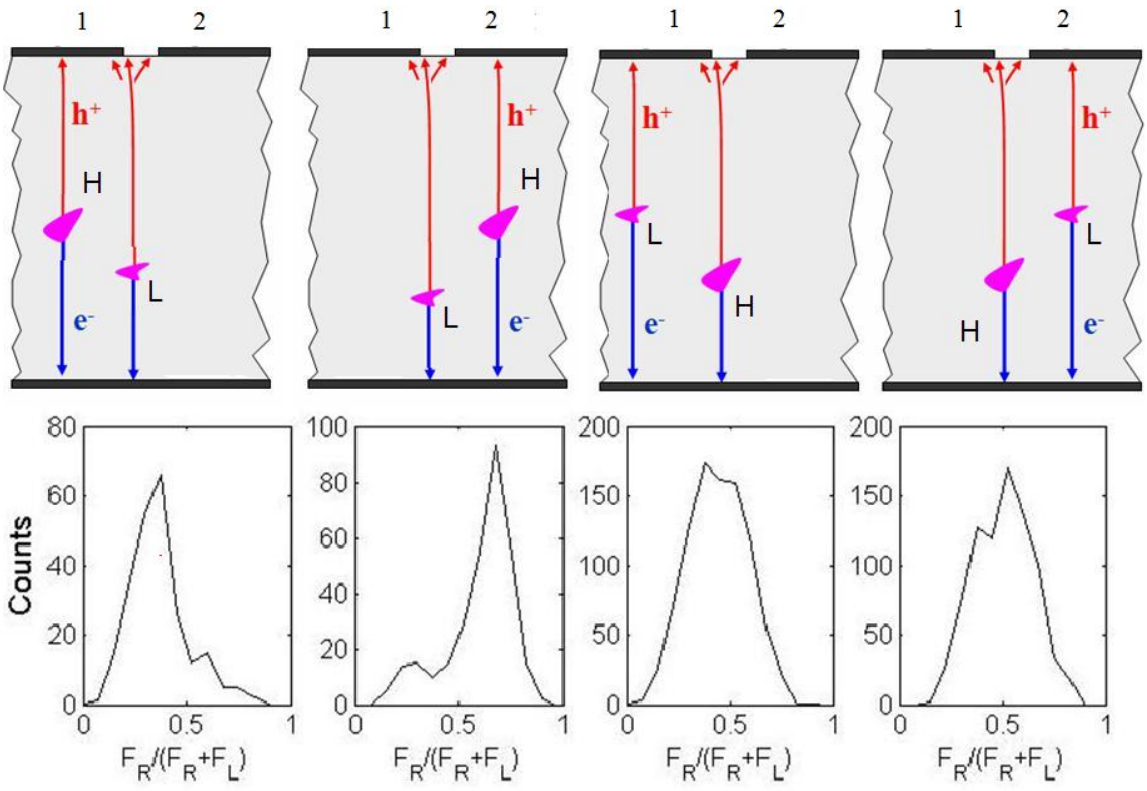

Fig. 55. The schematics in the top row indicate the CCE algorithm's prediction for the location of higher (H) and lower (L) energy interactions. In the bottom row, measured fast signals next to adjacent firing strips are binned using Eqn. 22 for comparison with predictions.

V.C.3.2. CCE fast signal behavior

As mentioned in II.C.2, the Spect32 system takes a peak-to-peak measurement of fast signals on every channel when any strip triggers. These are called fast energies. The fast energies on either side of a firing strip are used for lateral interpolation. These adjacent strips are called bystanders. The lateral interaction position in one dimension is proportional to the ratio

$$\frac{F_R}{F_L + F_R} \tag{22}$$

where F_R is the fast energy of the bystander lying the to the right side of the firing strip and F_L is the fast energy to the left.

In Fig. 55, measured fast energies next to adjacent firing strips 1 and 2 are compared with prediction of the location of high and low energy interactions. Cathode side data for 662 keV CCEs are binned according to Eqn. 22, where the left and right bystanders lie on either side of adjacent firing strips. In this case, the bystanders are separated by the pair of firing strips. The schematics on the top row in Fig. 55 indicate the algorithm's prediction for relative interaction position. In Fig. 55(a), for example, it is predicted that the lower energy interaction is located in the gap and the higher energy interaction falls within the bounds of the left strip.

When a high energy interaction occurs within strip bounds, as in Fig. 55(a) and Fig. 55(b), the distribution is then dominantly biased toward that particular strip. When the high energy interaction occurs in a gap, as in Fig. 55(c) and Fig. 55(d), there tends to be a slight asymmetry toward the strip that collects the lower energy interaction. This result is expected because the amplitude of induced transient signals is proportional to the interaction energy and proximity. Thus, measurement results are consistent with algorithm predictions for all 4 scenarios, helping to verify algorithm accuracy. Furthermore, corresponding results at 356 keV and on the anode side (not pictured) are consistent with those shown in Fig. 55.

V.C.3.3. CCE inter-strip interpolation results

The final verification of the CCE method is that the inter-strip interpolation method is consistent for SSIs and CCEs. The CCE inter-strip interpolation method was briefly

discussed in Section C.2. In the two following sections, the results of implementing the method on anode and cathode sides are given.

(a) (b) (c) (d)

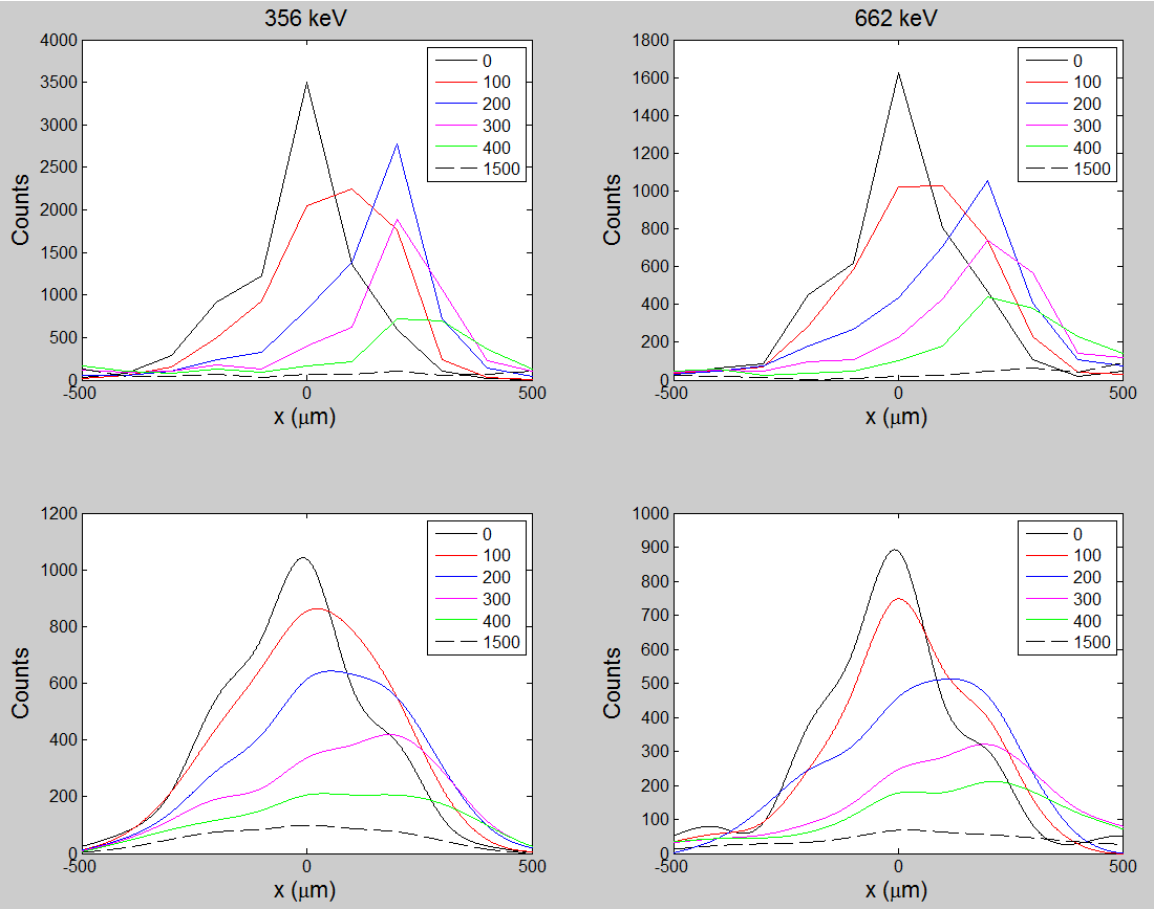

Fig. 56. (a) and (b) show the SSI inter-strip interpolation histograms presented in Fig. 47 for the anode side. (c) and (d) show the CCE inter-strip interpolation histograms. For each collimator position indicated in figure legends, the inter-strip position x was binned for all gap events.

V.C.3.3.1. Anode side

For each collimator position, the inter-strip position x was binned for all gap events. For convenience, Fig. 56(a) and Fig. 56(b) show the SSI inter-strip interpolation histograms presented in Fig. 47. Fig. 56(c) and Fig. 56(d) show the CCE inter-strip interpolation histograms. To aid in comparison, the latter have been smoothed. Figure

headings show irradiation energies for each column, and graph legends give collimator positions in μm.

Upon inspection, the CCE interpolation method produces results consistent with those of the SSI interpolation method. As collimator position shifts from the gap center toward the strip edge at 250 μm, the mean of each distribution shifts out as well. However, the FWHM of each CCE distribution is noticeably broadened in comparison to the corresponding SSI distribution. This is attributed to the systematic error introduced by determining $P\left(r,1-f\left|x_i\right.\right)$ at either 356 keV (Fig. 56(c)) or 662 keV (Fig. 56(d)) for CCEs. While the interpolated SSI events are monoenergetic at these energies, the energies of interpolated CCEs are not. Instead, these energies correspond to either the initial Compton scatter or the subsequent photoelectric absorption of a CCE. Thus, the broadening of the CCE distributions is expected, and it is possible to improve upon this result through an accurate simulation of $P\left(r,1-f\left|x_i\right.\right)$ across all relevant energies.

At 1500 μm, the data set consists of CCEs with first scatters within strip bounds and second scatters at random gap positions. Only the location of the first scatter is controlled via collimation, so the continuum across the gap at 1500 μm is expected. As position the gap center is approached, the data set includes more and more gap interactions at the first scatter location rather than the second scatter location. At the gap center, all gap interactions are at the first scatter location.

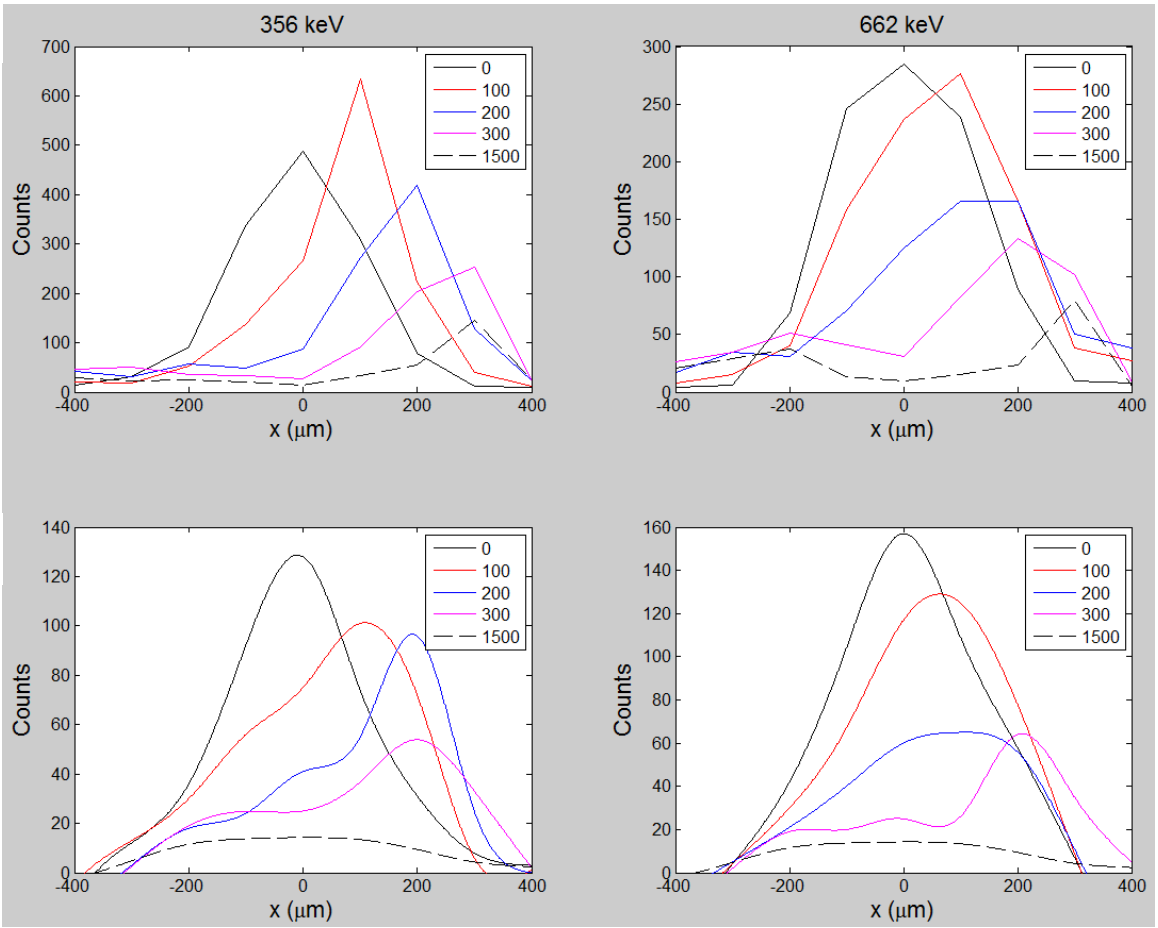

Fig. 57. (a) and (b) show the SSI inter-strip interpolation histograms presented in Fig. 50 for the cathode side. (c) and (d) show the CCE inter-strip interpolation histograms. For each collimator position indicated in figure legends, the inter-strip position x was binned for all gap events.

V.C.3.3.2. Cathode side

For each collimator position, the inter-strip position x was binned for all gap events. For convenience, Fig. 57(a) and Fig. 57(b) show the SSI inter-strip interpolation histograms presented in Fig. 50. Fig. 57(c) and Fig. 57(d) show the CCE inter-strip interpolation histograms. To aid in comparison, the latter have been smoothed. Figure headings show irradiation energies for each column, and graph legends give collimator positions in μm.

Upon inspection, the CCE interpolation method produces results consistent with those of the SSI interpolation method. As collimator position shifts from the gap center toward

the strip edge at 250 μm, the mean and most probable values of each distribution tend to shift out as well. On the cathode side, the FWHM of some CCE distributions look broadened in comparison to the corresponding SSI distribution. To quantify the change, the position resolution was calculated for CCE distributions at 0, 100, and 200 μm as before.

Table VI.
Comparison of position resolution for SSIs and CCEs on the anode and cathode sides

	356 keV			*662 keV*		
	0 μm	100 μm	200 μm	0 μm	100 μm	200 μm
$FWHM_{Anode}^{SSI}$	152	316	159	183	342	305
$FWHM_{Anode}^{CCE}$	325	437	467	256	342	431
$FWHM_{Cathode}^{SSI}$	253	157	189	315	290	330
$FWHM_{Cathode}^{CCE}$	254	348	182	284	318	388

The inter-strip position resolution for SSIs and CCEs is compared on anode and cathode sides in Table VI. As a whole, the position of lower energy CCEs cannot be determined as well as the SSIs. As mentioned, the position resolution is degraded for CCEs due to the systematic error of using $P(x \mid r, 1-f)$ at E_{peak} instead of $E_{gap,i}$ for all i. It is also possible that improved statistics for CCEs would have an impact on the results. Despite this degradation, Fig. 56 and Fig. 57 show that the CCEs that are also gap events have been correctly identified. Furthermore, it is possible to determine the position of the gap event with lateral resolution finer than the width of the strip gap. The

next section demonstrates that inter-strip position resolution for CCEs may be further improved through simulation of $P(x|r,1-f)$ across all energies.

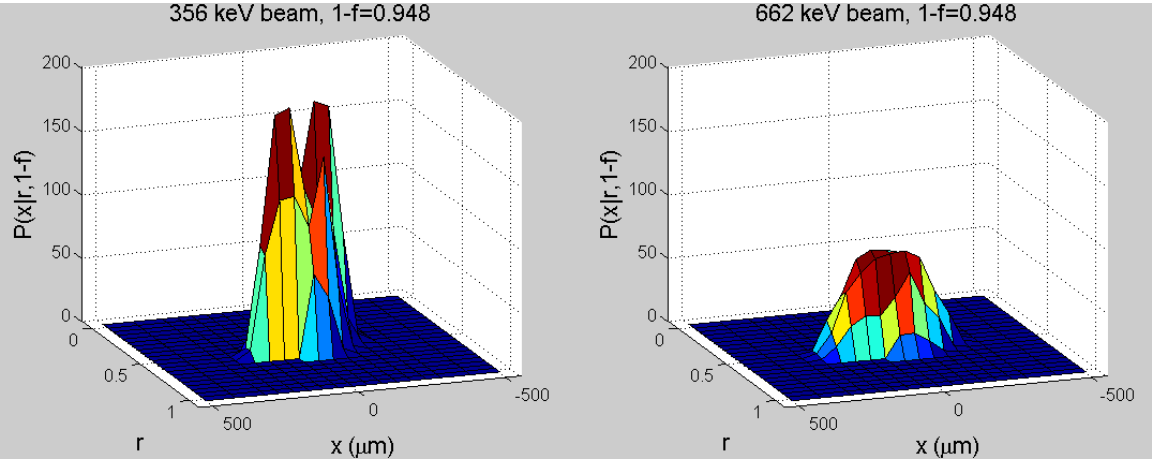

Fig. 58. Simulated conditional probability $P(x|r,1-f)$ at 356 or 662 keV for one value of $1-f$. The FWHM of $P(x|r,1-f)$ at any value of r gives the position resolution for a history with these values. The vertical axis is scaled by counts out of 1000.

V.D. Simulation of inter-strip position resolution

Surface modeling technique 2 was used to simulate the inter-strip position method for 356 keV and 662 keV SSIs in the UM HPGe detector. At each energy, 1000 histories were simulated at 50 μm increments across the detector gap, and Eqn. 18 was used to find $P(x|r,1-f)$ for x_i between -500 and 500μm. Fig. 58 shows $P(x|r,1-f)$ at 356 and 662 keV for one value of $1-f$. Over the full range of $1-f > 0.93$, the FWHM of $P(x|r,1-f)$ was determined for all values of $r \geq 0.5$ where $P(x|r,1-f)$ was significant. To aid in determining the FWHM, a cubic spline was fit to $P(x|r,1-f)$ for each $\{r_i,1-f_i\}$. At 356 keV, FWHM = 161±32 keV. At 662 keV, FWHM = 307±62 keV. These values agree well with the SSI results presented in Table VI.

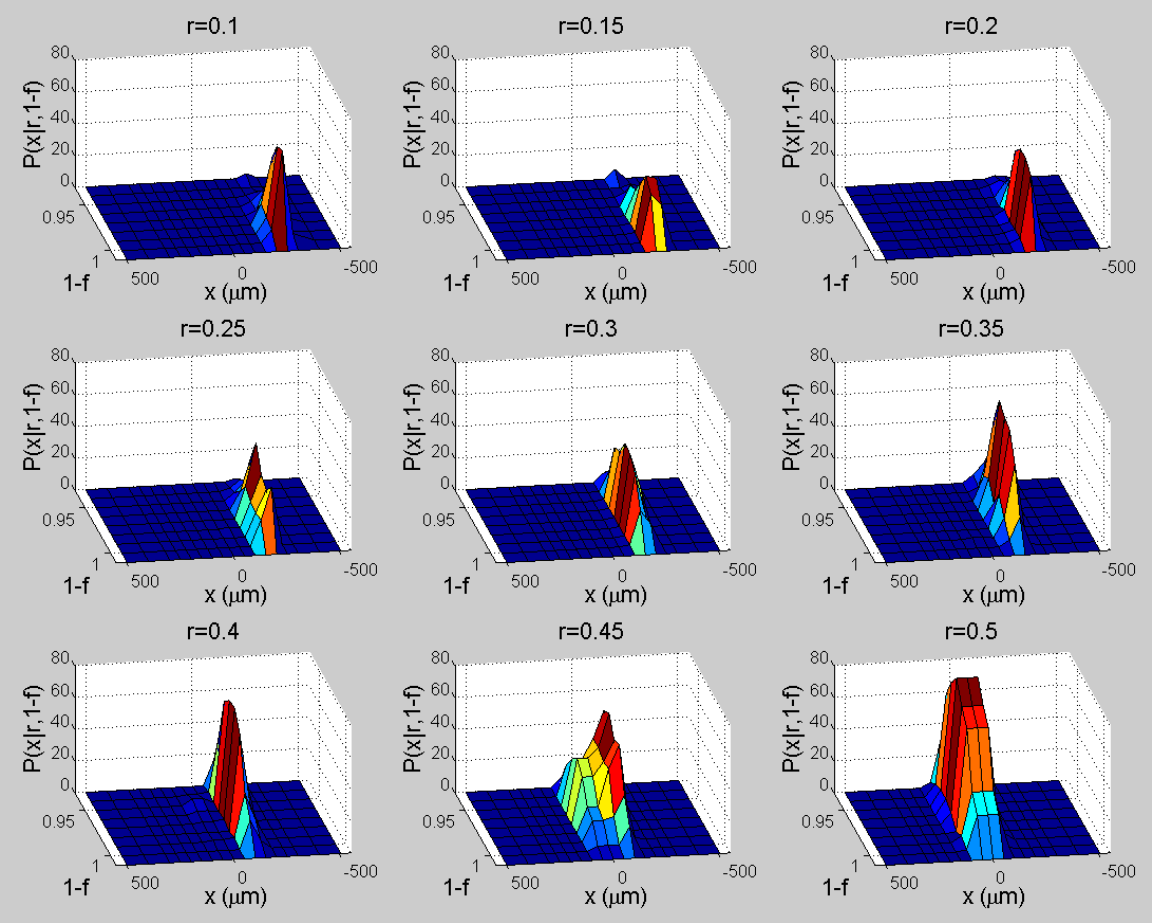

Fig. 59. Simulated conditional probability $P(x|r,1-f)$ at 356 or 662 keV for the values of r shown in figure headings. The FWHM of $P(x|r,1-f)$ at any value of $1-f$ gives the position resolution for a history with these values. The vertical axis is scaled by counts out of 1000.

Next, the procedure was repeated for simulated 200 keV clouds. These histories were simulated using GEANT4, as described in III.A. Compared to 356 and 662 keV clouds, a 200 keV charge cloud is more likely to take on any value of $1-f$ at a given interaction position in the gap. This is because 200 keV clouds have smaller extent, so they are more likely to stay in the center of the gap region, where charge loss is most probable. Since 200 keV clouds are better separated by r than $1-f$, Fig. 59 shows $P\left(x|r,1-f\right)$ at 200 keV for several values of r. As r increases from zero toward 0.5, the interpolated position x moves from the edges of strip 2 (at -250 μm) toward the gap center (at 0 μm).

Additionally, x moves from 1 toward $1-f_{\max}$ as r increases from zero toward 0.5. The FWHM of $P(x|r,1-f)$ at any value of $1-f$ gives the position resolution for a history with these values. Over the range of r shown in Fig. 59, the FWHM of $P(x|r,1-f)$ was determined for several values of $1-f_i$ at each r_i where $P(x|r,1-f)$ was significant. To aid in determining the FWHM, a cubic spline was fit to $P(x|r,1-f)$ for each selected $\{r_i,1-f_i\}$. At 200 keV, FWHM = 71±10 keV. This calculation does not consider the effects of a reduced *ISIR* at 200 keV (cf. Eqn. 17), which is expected to degrade the position resolution. Thus, the calculated resolution at 200 keV represents the limit for the UM HPGe detector as noise goes to zero.

The calculated resolution at 200 keV also suggests that inter-strip position resolution of CCEs could be improved upon through a simulation which has been benchmarked by measurements. Consider, for example, inter-strip interpolation of 356 keV CCEs, as shown in Fig. 56(c) and Fig. 57(c). As discussed in the last section, use of $P(x|r,1-f)$ at 356 keV for CCEs at 356 keV does not give the optimal result. This is because the first scatters in the gap have energies $E_{gap\,i}$ below the Compton edge of 207 keV, and it has been demonstrated that $P(x|r,1-f)$ changes significantly at 200 keV compared to 356 keV. If a detector gap simulation agrees with measured data at a few sampled energies across the range of interest, then accurate calculation of $P(r,1-f|x_i)$ at any first scatter energy should be possible as well, leading to an improved inter-strip interpolation result. To be effective for all gap events, this will require a simulation benchmarked for charge loss and charge-splitting on both anode and cathode sides.

Furthermore, the identification of gap events will require simulation of triggering in the detection system. Moreover, modeling of the noise in the detection system should also be included because it becomes important at lower gamma ray energies.

Chapter VI

Conclusion

Measurement-based methods for charge loss correction and inter-strip interpolation of gap events in the UM HPGe DSSD detector have been described. Over the energy range 60 – 1274 keV, charge loss correction increases photopeak counts by 15% on the anode side and 5% on the cathode side. On the anode side, the 15% increase in photopeak efficiency measured for a single gap was consistent with the measured increase over the gaps between eight adjacent strips. The smaller increase in efficiency for the cathode side is attributed to lower charge loss at the cathode side compared to the anode side. This work is the first to demonstrate a charge-loss correction for implementation in signal processing.

Inter-strip interpolation is able to determine the locations of recovered events, yielding Single Site Interaction position with lateral resolution of ~160 μm at 356 keV and ~310 μm at 662 keV. According to simulation, lateral resolution in the 500 μm gap is fundamentally limited to these values due to charge cloud size. At 200 keV, simulation shows that position resolution of less than 100 μm is achievable in the detector gap. Although inter-strip interpolation has not been demonstrated before in strip detectors, prior work on in-strip interpolation in HPGe DSSDs has shown lateral resolution as good

as ~250 μm (in a detector with 2 mm pitch) at 200 keV for interactions at some depths [23].

The energy-position dependence of the detector gap was exploited to perform charge loss correction and inter-strip interpolation for Close Compton Events where one of the two interactions falls in a gap. This CCE method performed charge loss correction nearly as well as the SSI method, limited only by signal-to-noise at low energies. Furthermore, lateral position resolution for the gap interaction was still finer than the width of the gap. The source of the systematic error degrading the lateral resolution of the gap interaction was identified, and potential for improvement through a simulation benchmarked by measurements was demonstrated. Proper energy and position determination of CCEs is important for Compton imaging with the UM detector because CCEs account for over half of all adjacent triggers at 662 keV.

The charge loss correction and inter-strip interpolation methods use slow signals for inter-strip interpolation, so depth of interaction is inconsequential. They are not computationally expensive, so they are suitable for real-time imaging applications. Furthermore, these methods should be applicable for HPGe DSSDs with different gap-to-strip width ratios, although this would likely require two changes. First, the fitting constants in Eqn. 15 may require recalculation for each detector side. It may be possible for these fitting constants to be determined through flood field measurements alone, which would greatly simplify the process. In this case, fitting constants could be determined through optimization techniques focusing on the four evaluation criteria given in IV.B.3. Second, the conditional probability $P\left(r,1-f\left|x_i\right.\right)$ at all relevant energies must

be determined through measurement or through a simulation which has been benchmarked by measurements.

Moreover, the inter-strip position interpolation method is attractive because the position uncertainty of each inter-strip interaction is calculated along with its position, where its uncertainty is given by its probability interval (cf. Eqn. 18). In the Appendix, a Bayesian method for in-strip lateral position interpolation (cf. Eqn. 23) is proposed as well. These Bayesian methods lend themselves to better use by advanced imaging reconstruction algorithms such as gamma-ray energy-imaging integrated spectral deconvolution [50]. This algorithm assigns greater weighting to events where there is higher confidence in the estimated parameters, such as interaction position.

Considering future HPGe DSSD designs for use in Compton imaging, depth resolution much closer to the intrinsic limit [38] and reduced strip pitch on the order of 1.5 mm or less are recommended to reduce complications introduced by CCEs. Furthermore, simulation suggests that charge loss might be reduced (or augmented, if desired) by engineering the material properties of a-Ge layers such that trapping yields fixed charge of the proper magnitude and polarity. If one desires to avoid the need for charge loss correction and inter-strip interpolation altogether, the gap width should be reduced to ~100 μm for gamma-ray detection. This change would introduce additional noise due to an increase in inter-strip capacitance, and electronic readout would become more costly and complex. However, the use of plasma-etched grooves in between strips may reduce this inter-strip capacitance [16]. Additionally, recent advances in FPGA development are allowing for reduction in electronics complexity and lower power consumption.

Appendix

Spect32 position interpolation and measurements on prior electronic acquisition systems

The Spect32 system employs a novel technique for lateral position interpolation of all 1-1 events in real-time. At 356 keV and 662 keV, most 1-1 events are caused by in-strip SSIs. In Section A, the lateral interpolation of in-strip SSIs is discussed and compared with the best reported result. The lateral interpolation of interactions which occur in the vicinity of a gap is described in Section B. In both sections A and B, software was written in-house to analyze the data output from the Spect32 system. Section C shows the performance of the Imager32 planar imaging software designed by PhDs for use with the Spect32 system. This software was modified in-house for more convenient use with the UM detector, and is currently undergoing further development by PhDs.

Section D shows how charge loss measurements were used to determine the depth resolution of the UM HPGe detection system. This measurement is compared with a second technique to determine the depth resolution of the detection system. In Section E, depth interpolation was used to show that charge loss is a surface effect in the HPGe detector. In addition, sections D and E provide: 1) improved understanding of the

detector's ability to separate SSIs from CCEs, and 2) additional verification of agreement between measured charge loss data and simulation of charge loss on the anode side.

Prior to use of the Spect32 system, measurements of interactions in detector gaps were recorded using two other acquisition systems. In Section D.2, depth timing measurements on a fast oscilloscope to determine system depth resolution are described. In Section F, charge loss measurements using conventional NIM electronic modules are presented. Moreover, these measurements are compared with Spect32 charge loss measurements to show that measured charge loss behavior is independent of the electronic acquisition system employed. In Section G, pulse shape measurements using the fast oscilloscope are shown, and the shaping of fast signals by the Spect32 system is simulated.

A. Lateral position interpolation for in-strip interactions

As mentioned in II.C.2, the Spect32 system records a peak-to-peak measurement of shaped fast signals on every channel when any strip triggers. These measurements are called fast energies. The fast energies on either side of a firing strip are used for lateral interpolation. The lateral interaction position in one dimension is proportional to the ratio

$$\frac{F_R}{F_L + F_R} \tag{22}$$

where F_R is the fast energy of the bystander lying to the right side of the firing strip and F_L is the fast energy to the left of the firing strip.

To determine the lateral position resolution for SSIs, a Cs-137 source was collimated to 50 μm (FWHM=68 μm) and scanned over a full strip pitch on the cathode side. In Fig. 60(a), all 662 keV 1-1 events are binned according to Eqn. 22 for several interaction depths. The depths from the cathode side are given in figure headings and the uncertainty at each depth is ±1 mm. Fig. 60(b) shows collimator positions and the relative locations of fast signals. All irradiation positions in the graph legend are given in μm.

At each depth shown in Fig. 60(a), the location of peak values shifts along with collimator position. This means that $\frac{F_R}{F_R + F_L}$ is monotonic with the shift in lateral interaction position for SSIs which occur within the lateral bounds of a detector strip. As interaction depth increases beyond 3 mm, the distributions at each position are better resolved and their centroids move inward toward $\frac{F_R}{F_R + F_L} = \frac{1}{2}$. The shifting of centroid locations is attributed to the change in polarity of the bystander signals from bipolar to unipolar as depth increases beyond 3 mm [51]. Thus, lateral position is better resolved by the Spect32 system when bystander signals are unipolar. Additional information regarding the shaping of raw signals by the fast filter is discussed in Section G.3.

(a)

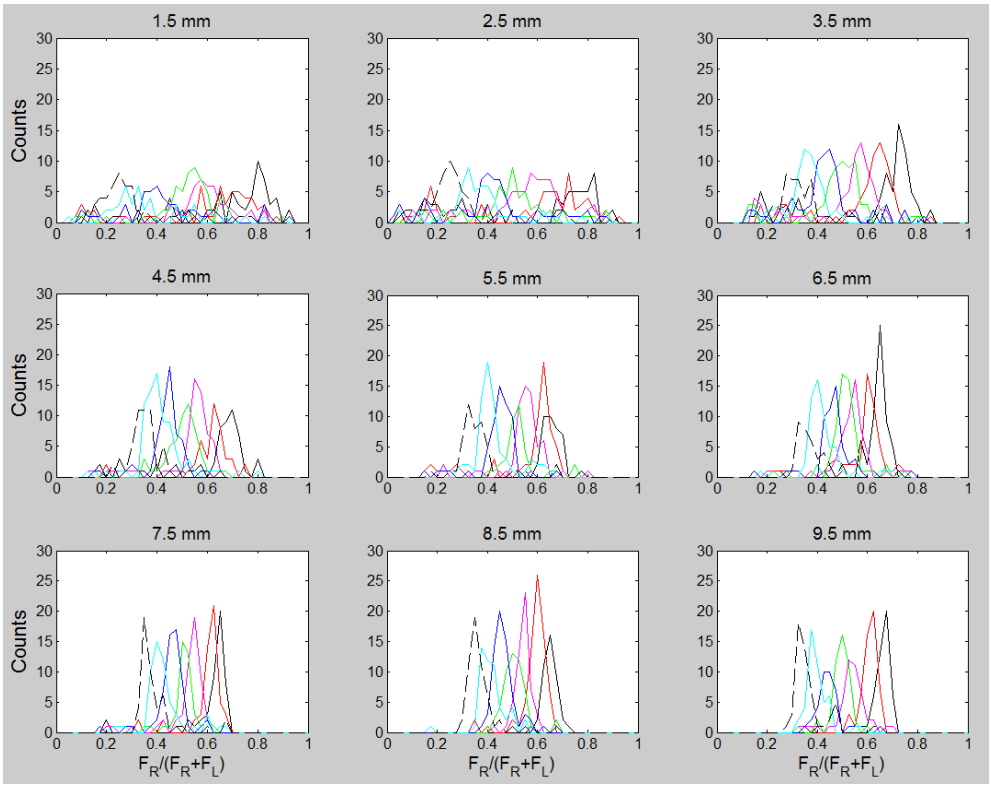

(b)

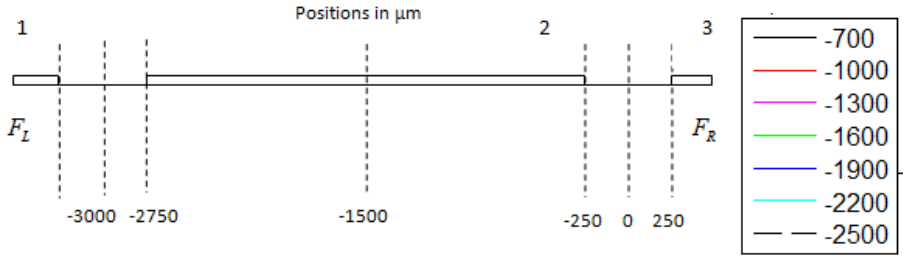

Fig. 60. (a) 662 keV 1-1 SSIs are binned according to Eqn. 22 for several interaction depths. (b) identifies strips where fast signals are recorded and shows collimator locations.

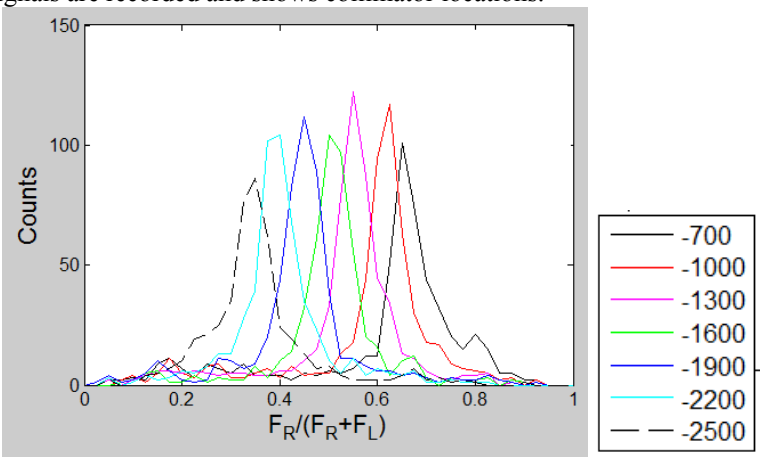

Fig. 61. The sum of the data shown in Fig. 60(a) across all interaction depths.

Fig. 61 shows $\frac{F_R}{F_R + F_L}$ at each collimated position after summing the counts from all depths together. Even after combining all depths, the distributions at each lateral position can still be resolved from one another at 662 keV. Furthermore, the result appears the same at 356 keV. For optimal lateral position resolution, the fast trapezoidal filter was set with a rise time of 30 ns, a flat top time of zero ns, and a fall time of 30 ns. As mentioned in II.C.2, these FPGA firmware settings were adjustable through an interface built into Imager32 software. The optimal filter settings were determined empirically by incremental adjustment until the best resolution was achieved across all detector depths. This empirical testing was conducted at 356 keV and 662 keV on anode and cathode sides. The histograms of $\frac{F_R}{F_R + F_L}$ from fast signals recorded on cathode strips appear nearly identical to those shown in Fig. 60 and Fig. 61.

The data shown in Fig. 60 and Fig. 61 suggest that position resolution for in-strip SSIs is ~300-400 μm because it is possible to resolve all distributions from one another at 300 μm lateral spacing. Moreover, the data show that position resolution is independent of electron energy and charge cloud size at 356 keV and 662 keV. Physically, this is true because carriers are not lost to the gap or split between strips for in-strip SSIs. However, position resolution is degraded at shallow depths where fast signals are bipolar. Furthermore, separation of interactions by depth is advantageous due to the shifting of centroid position with depth, as seen in Fig. 60. This shifting with depth results in undesired tailing of the distributions shown in Fig. 61.

The data presented in Fig. 60 suggest that position resolution changes with both interaction depth and lateral position. In this work, the position resolution at all possible interaction locations has not been explicitly calculated (as it was for the inter-strip interpolation method in Chapter V). Yet, the data presented here suggest that the lateral position x for an in-strip SSI of any energy is best estimated from

$$P(x_i \mid F_R, F_L, z) = \frac{P(x_i)P(F_R, F_L, z \mid x_i)}{\sum_{j=1}^{N} P(x_j)P(F_R, F_L, z \mid x_j)} \tag{23}$$

where z is interaction depth and x_j for $j = 1, 2...N$ are collimated in-strip positions. At each x_j, the quantity $P(F_R, F_L, z \mid x_j)$ can be determined from the measurements shown in Fig. 60(a). Like the inter-strip interpolation method, this Bayesian interpolation technique allows estimation of the in-strip position and its uncertainty. Based upon the data shown in Fig. 60(a), position uncertainty is expected to increase at shallow depths. Furthermore, position estimation at shallow depths can be improved if the measured counts at these depths were higher.

In summary, lateral resolution for in-strip interactions is reported to be ~300-400 μm at 356 keV and 662 keV. For comparison, lateral resolution for in-strip SSIs has been reported by others, as discussed in II.A.5. The best lateral resolution attained at any interaction depth was 250 μm at 200 keV for a similar HPGe DSSD with 2 mm strip pitch. However, it was not possible to attain this position resolution at all interaction depths due to the complication of bipolar fast signals at some depths. At 122 keV, the best position resolution was found to be 0.5 mm due to reduced signal-to-noise of the fast

signals [23]. Furthermore, these results were obtained through offline analysis of measured fast signals. Considering that the best achievable in-strip lateral resolution scales inversely with strip pitch, it appears that the lateral in-strip resolution achieved with the Spect32 system is as good as the best resolution achieved in [23]. Moreover, the Spect32 method has been implemented in FPGA firmware so that it is conducive to real-time Compton imaging.

B. Lateral position interpolation for interactions in the vicinity of a gap

Fig. 62(a) continues where Fig. 61 leaves off, approaching the gap center. Events which lose charge to the gap are included in this analysis, and slow energies on adjacent strips are summed together. As the gap center (0 μm) is approached, 1-1 counts decrease. Concurrently, the number of SSIs that produce triggers on both adjacent cathode strips increase, as shown in Fig. 62(b). These adjacent strips fire due to splitting of the hole cloud between the strips. In Fig. 62(b), F_R and F_L are three strips apart because they lie on either side of the adjacent firing strips. Considering the shape of each distribution, it is not possible to determine the lateral position of SSIs on an event-by-event basis when adjacent strips fire. This is not surprising, considering that the bystanders are each removed from the interaction by a strip pitch. Thus, it is necessary to use the inter-strip interpolation method described in Chapter V.

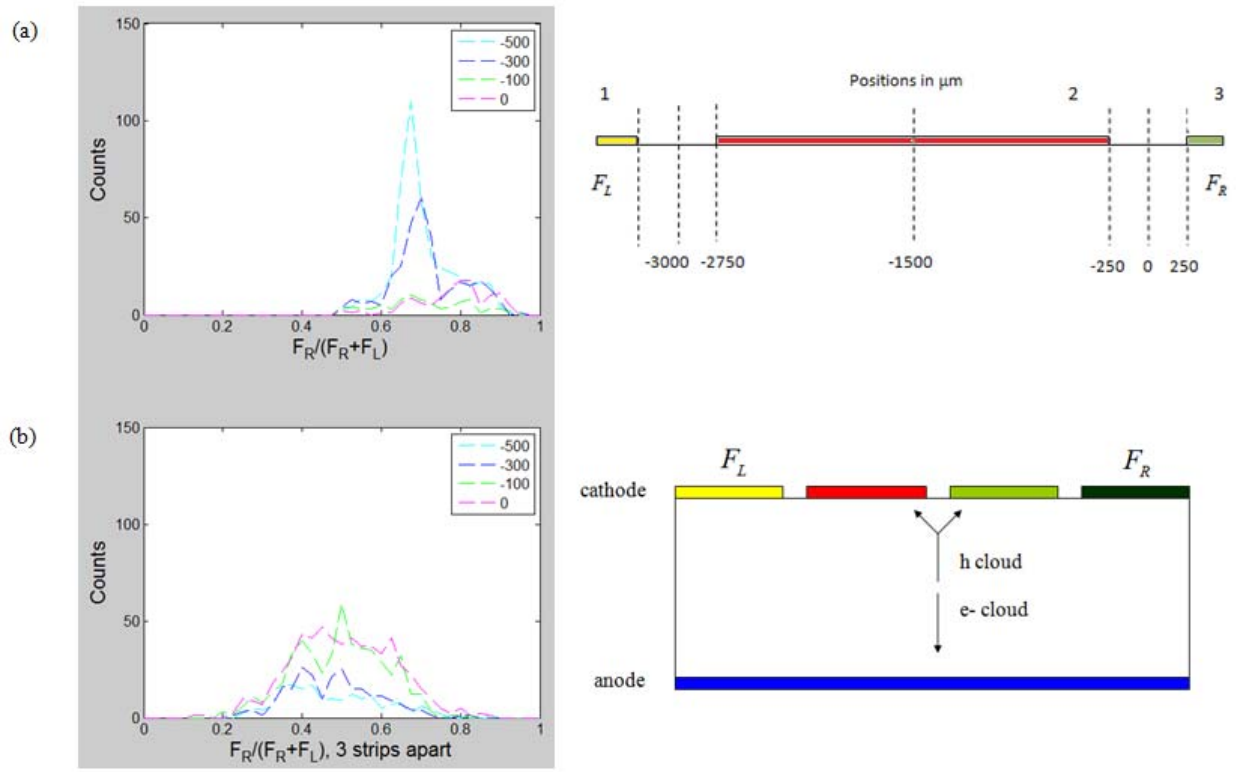

Fig. 62. (a) 662 keV 1-1 SSIs are binned according to Eqn. 22, summed over all interaction depths. The schematic to the right shows the position of fast signals. (b) 662 keV SSIs which trigger adjacent cathode strips are binned according to Eqn. 22. The schematic to the right shows the position of the fast signals lying on either side of firing strips.

C. Spect32 planar imaging performance

The Imager32 planar imaging software bins and plots the 3D interaction positions of 1-1 events at a single energy. The performance of this software at 356 keV is reported next. First, all Spect32 channels were instrumented and calibrated for energy. After flood field irradiation with a Ba-133 source, the Spect32 software was used to automatically find the 356 keV peak on each channel and perform the calibration. After calibration, a longer duration flood field irradiation was performed. This data was used to make a distribution table per Eqn. 22 for each imaging pixel, where a pixel is formed by a strip and one of its depth cuts. Fig. 63 gives the distribution for a single pixel, where

$\frac{F_R}{F_R + F_L}$, which ranges from 0 to 1, is separated into 1024 bins. For comparison, this distribution agrees with the sum of the separate lateral distributions seen at a single depth in Fig. 60(a).

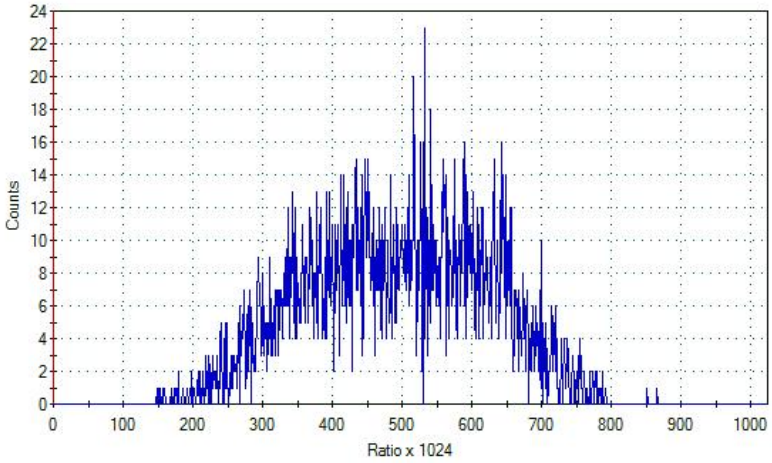

Fig. 63. Data used by Imager32 software to determine the distribution table of a single pixel for lateral position interpolation. The data was acquired upon flood field irradiation with a 356 keV source.

Imager32 software automatically bins each pixel's distribution into 9 equal-area parts. These 9 bins are assumed to correspond to 9 equally spaced locations from edge-to-edge of a single strip. According to the histograms shown in Fig. 60(a), this assumption is reasonable when the appropriate fast filter settings are used. However, it is expected that the use of Eqn. 23 to perform lateral interpolation will yield a slightly improved result because the distributions at adjacent lateral positions overlap in Fig. 60(a). Referring back to Fig. 63, the binning shown is carried out for each detector side, allowing the generation of 3D imaging voxels. Next, an energy window was chosen for imaging. By default, the 356 keV peak was selected with a window width equal to its mean FWHM (across all instrumented channels) of 2.96 keV.

Fig. 64(a) shows a planar image of a 356 keV source collimated to 50 μm by 1 cm. The collimator was aligned so that all photo-interactions occurred at the center of anode strip 2 (position -1500 μm). Eight adjacent anode strips (0-7 plotted along the bottom) and all 23 cathode strips were instrumented (8-30 plotted along the side) by the Spect32 system. All depth cuts were selected for planar imaging. The image was acquired over a period of 1000 s. Referring to Fig. 64(a), there is a line source located at the center of strip 2, so the image does agree with the source location. The width of the distribution is indicative of the breadth of the beam (56 μm FWHM) and the system position resolution. For comparison, the distributions at the strip center in Fig. 61 show essentially the same information.

The line source distribution seen in Fig. 64(a) was observed to shift with collimator position. To demonstrate, Fig 64(b) is an image formed over an equal time period near the rightmost edge of strip 2. The intensity of the image is diminished because charge loss to the gap causes events to fall below the narrow 2.96 keV energy window. When the collimator was shifted another 200 μm toward strip 3, the image shown in Fig. 64(c) was produced. Similar images were produced when the source was shifted 100 or 200 μm further toward strip 3. At the gap center, the line source is no longer resolved because nearly all events have fallen below the narrow energy window. Widening the window does result in a slight increase in counts, especially closer to the gap edges. However, at the gap center, the 356 keV line source is still not resolved for any window width. The same happens when the 356 keV source is replaced by the 662 keV source and the experiment is repeated. This result is expected because charge is split between

adjacent strips, but the current version of planar imaging software does not account for this physical phenomenon.

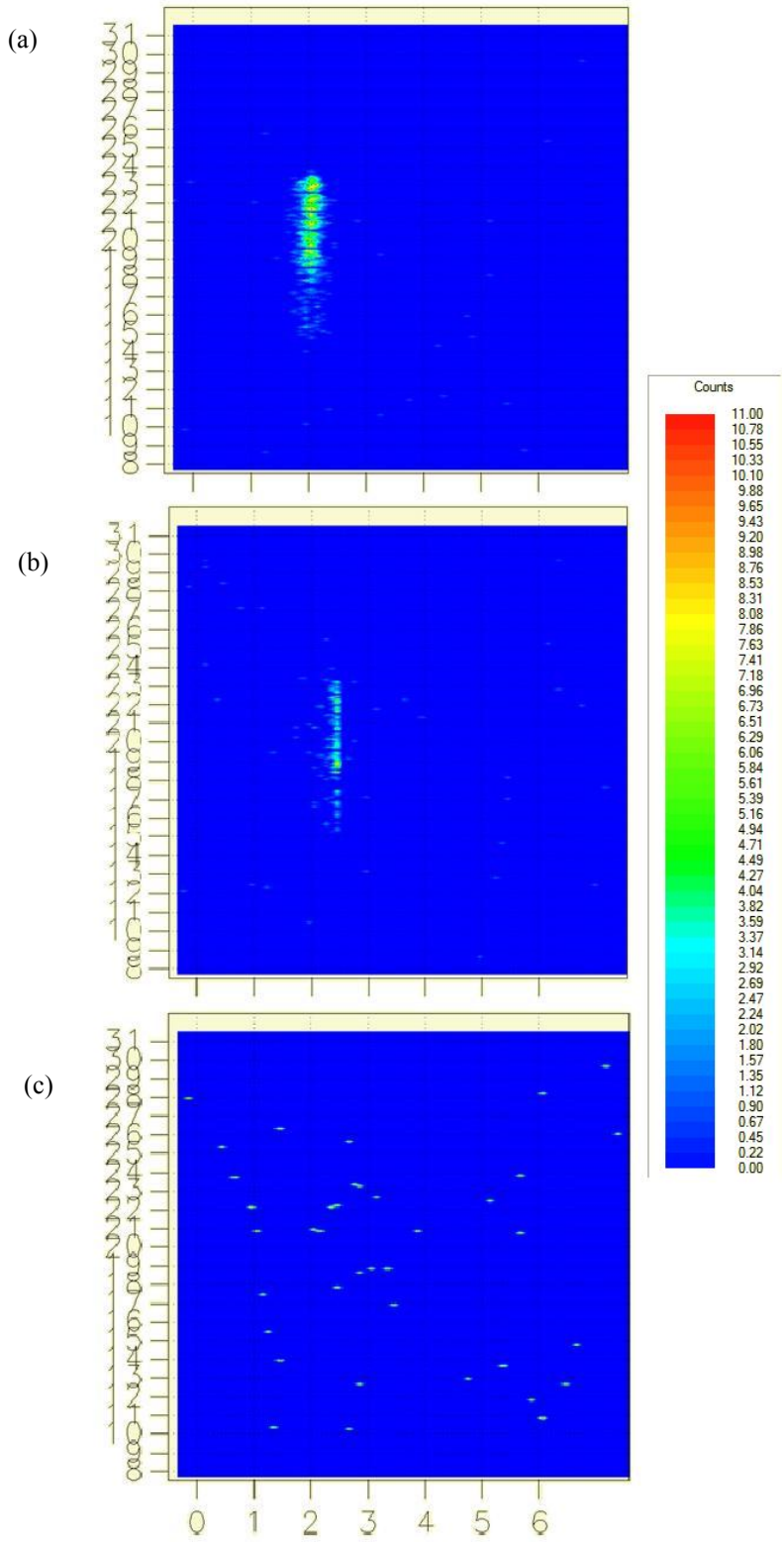

Fig. 64. Planar images formed in Imager32 software of a 356 keV line source positioned (a) at the center of anode strip 2, (b) near to the rightmost edge of anode strip 2, and (c) in the gap between anode strip 2 and strip 3.

D. Depth timing measurements to determine depth resolution

In this section, depth timing measurements to determine the system depth resolution are presented. Section D.1 provides a better understanding of the use of depth timing in the Spect32 system to separate SSIs from CCEs. Section D.2 shows that the depth resolution of the detection system is improved using a fast oscilloscope as the acquisition system.

1. Relationship between charge loss measurements and Spect32 depth timing

Charge loss measurements were used as one method to determine the depth resolution of the detection system. A Ba-133 source was collimated to 50 μm by 1 cm, aligned so that all first interactions occurred at the gap center between two adjacent anode strips. Only these two adjacent channels were instrumented using the Spect32 system, and all events which produced triggers on one or both strips were recorded.

Next, an attempt was made to use depth timing alone to separate SSIs from CCEs. It was presumed that a system with ideal depth resolution would be able to separate nearly all SSIs from CCEs because the separate interactions of CCEs are unlikely to occur at the same interaction depth. According to simulation technique 2, which was verified for the anode side in IV.A.5.1, SSIs which originate at the gap center lose ~5.5% of their charge-carriers. Furthermore, CCEs lose a smaller fraction of charge compared to SSIs at the same lateral position because the second interaction is likely to be recorded under a neighboring strip. For CCEs, charge loss is proportional to the energy of the electron produced by the first Compton scatter. Thus, it was presumed that charge loss

measurements at the gap center could be used to determine the depth resolution of the detection system.

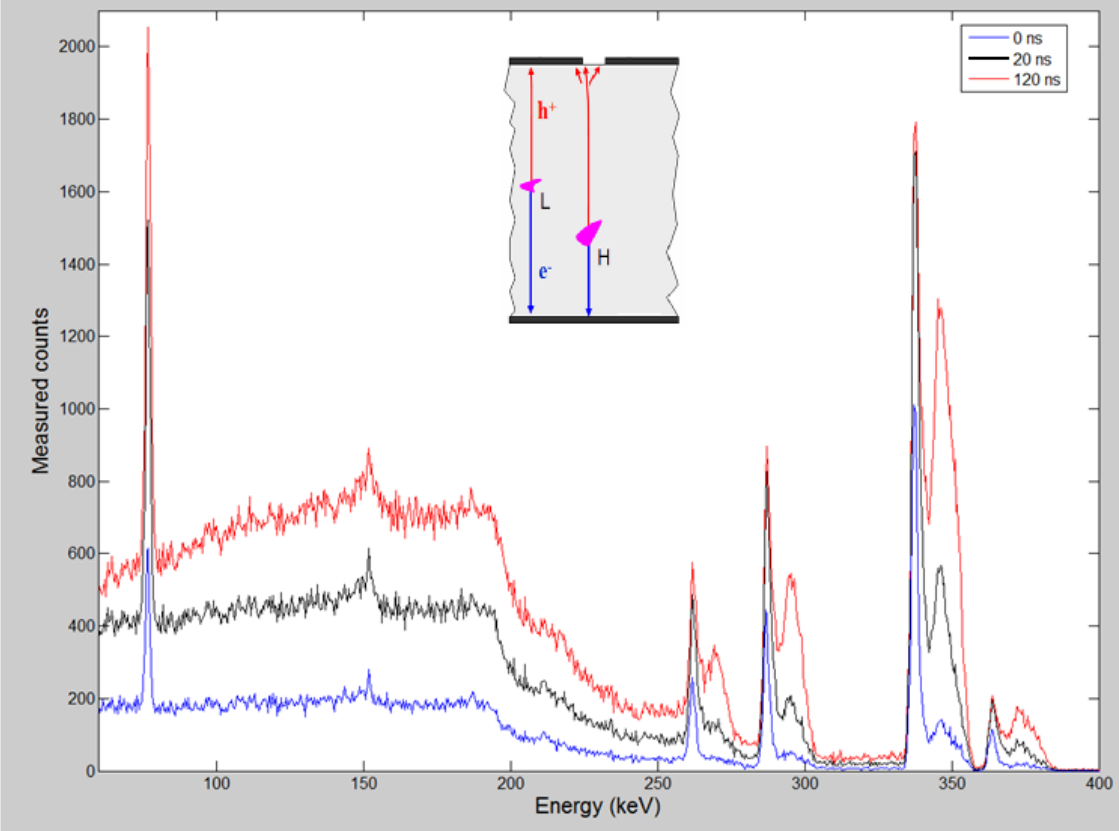

Fig. 65. The spectra from the sum of two adjacent anode strips when a Ba-133 source is collimated to the center between the strips. All events are plotted for adjacent triggers that fire within 0, 20, and 120 ns of each other. The schematic of two drifting charge clouds in the figure is meant to show that depth timing alone was used to separate SSIs at the gap center from CCEs where only the first interaction was constrained to the gap center.

In Fig. 65, the spectra from the sum of the two adjacent anode strips are shown. Events are binned for adjacent triggers within 0, 20, and 120 ns of each other, as indicated in the figure legend. A normal Ba-133 spectrum has photopeaks at 81 keV (34%), 276 keV (7%), 302 keV (18%), 356 keV (62%), and 384 keV (9%), but all of the most prominent peaks of each of the measured spectra occur at a deficit of 5.5%. At 120 ns, all SSIs and CCEs are included because the carriers from all interactions in a

Compton sequence are collected within 120 ns. At 120 ns, there is only one peak corresponding to the 81 keV peak because the cross section for Compton scattering is low (see Fig. 66(b)). As gamma ray energy increases, the fraction of CCEs increases, as shown in Fig. 66(a), so the relative prominence of the second peak at higher $1-f$ increases.

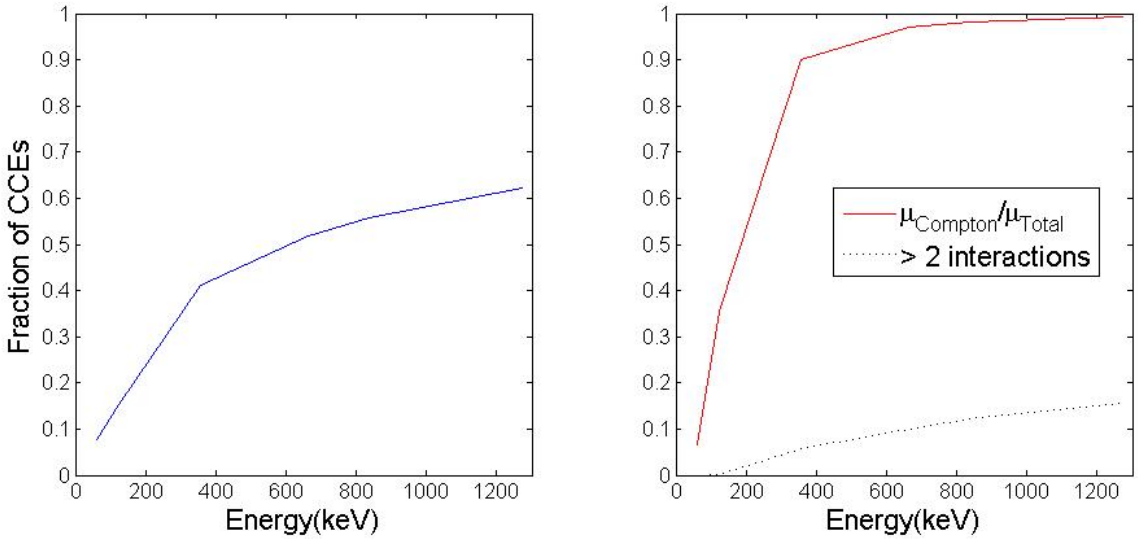

Fig. 66. Fig. 54 is shown here again for convenience. (a) The measured fraction of CCEs as a function of gamma ray energy. (b) As indicated by the legend, the ratio of the attenuation coefficents for Compton scattering to the total $\mu_{Compton}/\mu_{Total}$, or the fraction of CCEs consisting of more than two interactions.

At 20 ns, the prominence of this second peak at higher $1-f$ is diminished because many CCEs are eliminated. At 0 ns, this second peak is further diminished, but the height of the peak at lower $1-f$, corresponding to SSIs, is significantly diminished as well. The change from 20 ns to 0 ns can be better seen at 356 keV in Fig. 67(a). Fig. 67(b) shows simulation of 356 keV SSIs at the gap center (0 μm), evincing that the peak at $1-f \sim 0.945$ corresponds to SSIs. While CCEs are better discriminated at 0 ns compared to 20 ns, efficiency in resolving SSIs is also greatly reduced. Thus, it is

demonstrated that the depth resolution of the Spect32 system is about ± 20 ns, which corresponds to ±1 mm. The depth uncertainty is relatively high because the system clock is 20 ns and there is uncertainty in determining the 50% crossing times of both anode and cathode signals.

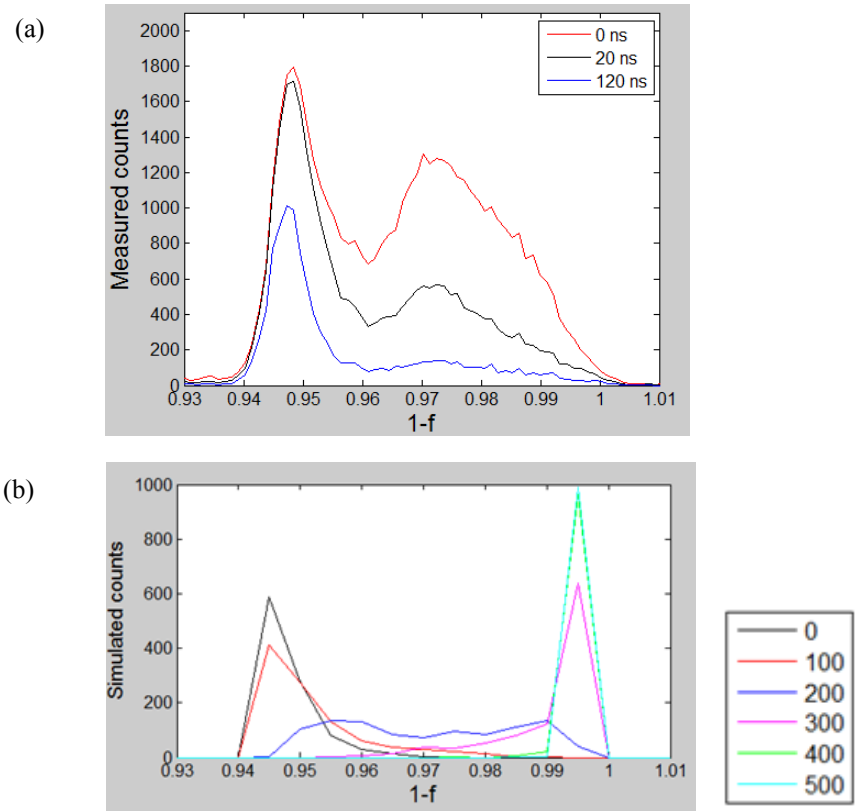

Fig. 67. (a) A close-up of the shifted 356 keV peak shown in Fig. 65. Gamma ray energy has been divided by $E_{peak} = 356keV$ to yield the charge collection fraction $1-f$. (b) For comparison, simulation of 356 keV SSIs via technique 2, which was verified for the anode side. The figure caption gives lateral interaction positions.

2. Determination of system depth resolution using a fast oscilloscope

As mentioned in III.C.2, the depth resolution of the Spect32 system was also determined to be ± 20 ns using the method described in [45]. According to this method, the depth resolution can be found from separate irradiations of anode and cathode sides

with a 60 keV source. To explore the effect of a higher sampling rate, this method was repeated using an Agilent MSO6104A scope as the acquisition system. This 1 GHz scope samples at 4 GSa/s. Coincidence triggers between one cathode strip and one anode strip were recorded, and 50% constant fraction times were programmed to be automatically measured by the scope. The measurements are shown in Fig. 68. Using the oscilloscope as the readout system, the depth resolution of the system was determined to be ~600 μm. Clearly, better depth resolution is possible with improved timing and/or interpolation methodology.

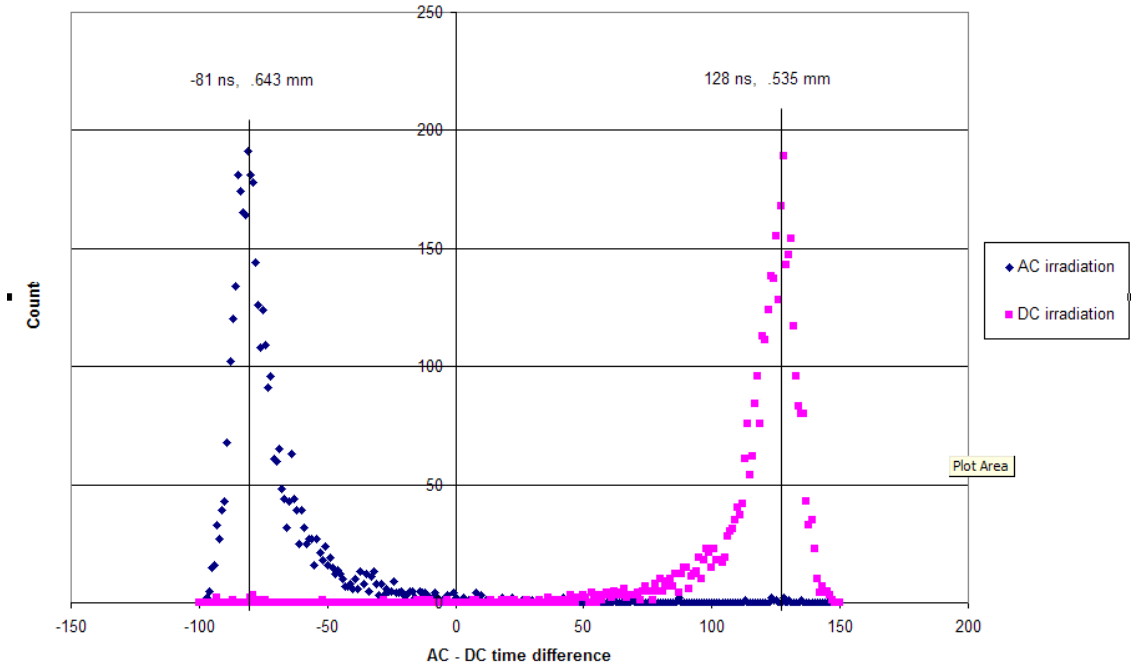

Fig. 68. Determination of depth resolution of the UM HPGe detector readout by a fast oscilloscope. The detector was irradiated by a 60 keV source from the cathode (AC) and anode (DC) sides. The depth resolution is determined based upon the positions and the widths of the peaks.

E. Use of Spect32 depth interpolation to show that charge loss is a surface effect

In Fig. 69, depth interpolation has been used to show charge collection as a function of depth from the cathode surface. The anode SSI data set at 356 keV was selected. Depths are indicated in figure headings, and lateral positions are indicated by colors in the legend. The uncertainty in depth resolution is ±1 mm. The count rate increases gradually as a function of depth because the source irradiates the detector from the anode side. At each depth, charge loss of up to $1-f_{\max}=0.93$ is observed. As the axial center of the detector (5.5 mm depth) is approached from either detector surface, it appears that the charge collection fraction of SSIs at 0 μm or 100 μm increases. At 5.5 mm depth, the peak counts at $1-f=0.945$ and $1-f=0.97$ are nearly equal. This effect is attributed to the presence of unresolved CCEs, which are more likely to be mistaken for SSIs which originate at the axial center of the detector. This is the case because the axial position of the 2-3 separate interactions is effectively averaged out when a CCE is indistinguishable from a SSI, and this average tends to lie near the axial center of the detector.

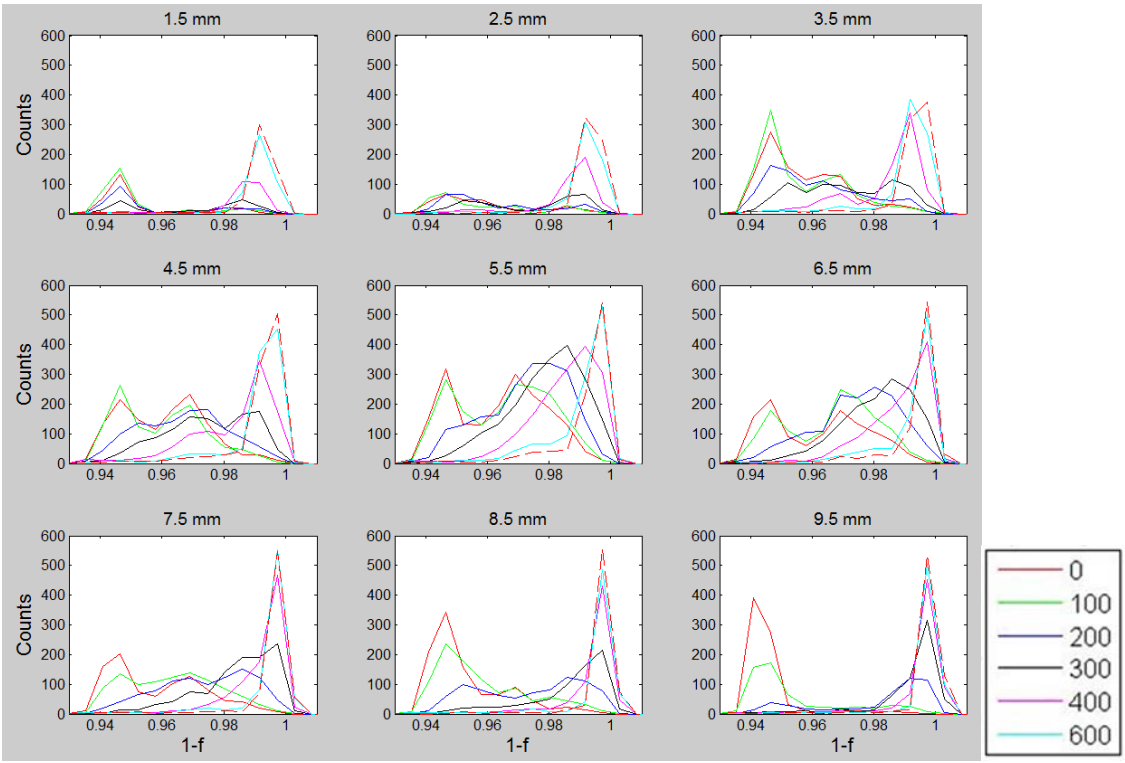

Fig. 69. Charge collection as a function of depth from the cathode surface. The anode SSI data set at 356 keV was selected. The legend shows lateral irradiation positions in μm.

Neglecting the effect of unresolved CCEs, the data presented in Fig. 69 show that charge loss of SSIs is largely independent of interaction depth in HPGe detectors. Charge loss is independent of interaction depth because carriers from interactions at any depth drift to the surface, and charge collection is a surface phenomenon. According to the simulations presented in III.C.4, the effect of diffusion on charge loss as interaction depth changes is a minor effect. Compared to the effect of unresolved CCEs, the effect of diffusion is too small to be observed in the data shown in Fig. 69. In a detector with ideal depth resolution, it is expected that the effect of diffusion at different depths may still be very difficult to measure. This finding justifies the choice not to include any depth dependence in the inter-strip interpolation method.

Measurements shown in Fig. 67(a) and Fig. 69 provide further verification of the agreement between the anode data set and simulation technique 2. Referring to the 0 ns plot in Fig. 67(a), the exclusion of most unresolved CCEs through timing methods provides the best agreement between simulation (shown in Fig. 67(b)) and measurement. In Fig. 69, the plots near the detector surfaces at 1.5 mm, 8.5 mm, and 9.5 mm agree best with the simulation shown in Fig. 67(b) because unresolved CCEs are less likely to be confused with SSIs which interact near the surface.

In the UM HPGe detector, it is expected that improved depth timing would be increasing crucial to characterize charge loss and obtain data for inter-strip interpolation at gamma ray energies in the 50-300 keV range. As gamma ray energy decreases, the mean free path between the position of the initial Compton scatter and the second interaction position decreases. Thus, at 3 mm strip pitch, the fraction of unidentified CCEs is expected to increase as gamma ray energy decreases. For the same depth resolution, the problem worsens as strip pitch increases above 3 mm strip. Thus, to minimize the complications introduced by CCEs, improved depth timing and a reduction in strip pitch for future HPGe detectors are recommended. The lower the gamma ray energy of interest, the more important it is to implement these recommendations.

F. Charge loss measurements using conventional NIM electronic modules

In this section, charge loss measurements using conventional NIM electronic modules are described. These measurements are presented and compared with Spect32 charge loss measurements to show that measured charge loss behavior is independent of the electronic acquisition system employed. Furthermore, the measurements are largely

independent of the particular gap selected for analysis on the anode side or the cathode side. Finally, the dependence of charge loss measurement upon peaking time is discussed.

The reader should note that charge loss was not studied as operating voltage was increased beyond 700 V because the detector manufacturer cautioned that higher voltages may damage the preamplifiers. Furthermore, simulations of the UM HPGe DSSD in MEDICI showed that higher operating voltage resulted in increased E_z but not increased $\frac{E_\ell}{E_z}$. Thus, it is expected that increased operating voltage will not result in a significant reduction in charge loss in the UM detector.

1. Experimental setups for charge loss measurement using NIM electronics modules

For this experiment, adjacent detector channels were sent through spectroscopy amplifiers set to 2 μs shaping time (ORTEC 572), summed together (ORTEC 533), then analyzed with a multi-channel analyzer (ORTEC 926 MCB). Compared with the Spect32 system discussed in Section D.1, the timing mechanisms of these NIM electronic modules did not allow the separation of SSIs from CCEs. Furthermore, it was not possible to instrument an entire detector side to help separate SSIs from CCEs based upon triggering.

Next, energy spectra were acquired with a 662 keV collimated radiation beam incident upon either the front face of the detector (setup 1) or the side of the detector (setup 2). In setup 1, the collimator widths were 100 μm × 2 mm. Setup 2, which is pictured in Fig. 29, allowed for collimation into an anode side gap (parallel to the anode strips), as well as

to a specific detector depth. In setup 2, the collimator widths were 75 μm × 1 cm. For each setup, the smaller collimator dimension was aligned between the two instrumented strips. For examination of charge loss at the anode side, radiation was collimated between adjacent anode strips. For examination of charge loss at the cathode side, radiation was collimated between adjacent cathode strips.

For setup 2, a mounted laser level and a digital protractor system (with precision 0.01°) were used for external detector-beam alignment. Alignment was then checked by collimating first along the anode surface and next along the cathode surface, each time comparing the 5 – 50% constant fraction rise times of 10,000 recorded signals on channel AC 1 (first cathode strip) and then on AC 23 (last cathode strip), which are laterally separated by 66 mm. This measurement was performed with the Agilent MSO6104A scope. At each surface, there was agreement between signal rise times on AC 1 and AC 23, meaning that alignment of the beam along the detector depth was correct.

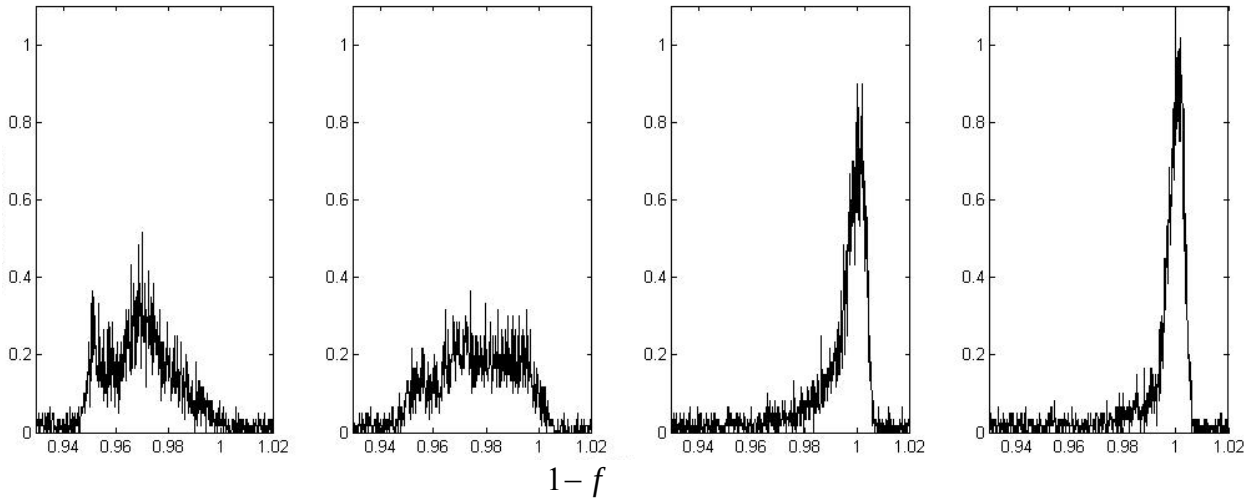

Fig. 70. Charge loss measurements in a gap between anode strips, where the detector is irradiated on its face (setup 1). A 662 keV source was collimated to the gap center and to positions removed by 150 um, 450 um, and 700 um, shown in order from left to right. Spectra are shown for the sum of adjacent strips by conventional NIM modules. Counts are normalized to the peak counts at 1500 um, and energy is divided by 662 keV to yield charge collection fraction.

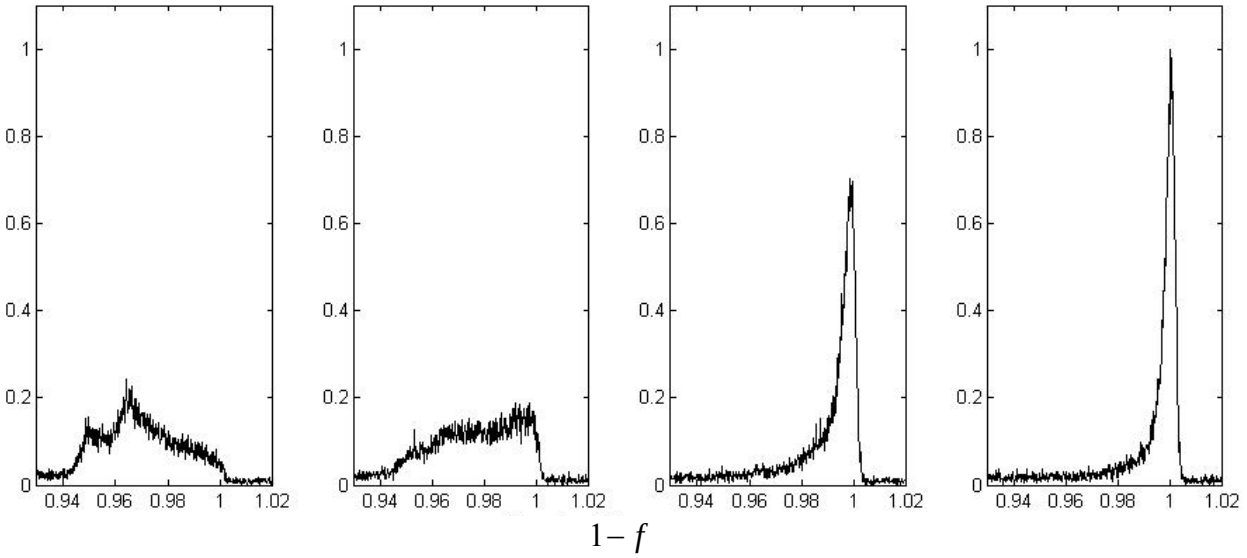

Fig. 71. Charge loss measurements in a gap between anode strips, where the detector is irradiated from its edge (setup 2). A 662 keV source was collimated to the gap center and to positions removed by 150 um, 450 um, and 700 um, shown in order from left to right. The spectra are consistent with those shown in Fig. 70, although the counts here because the source positioning allows for improved detection efficiency.

2. Comparison of charge loss measurements using different acquisition systems

Fig. 70 shows charge loss measurements on the anode side at 662 keV when setup 1 was employed. From left to right, the collimated source was positioned at the gap center

and at positions removed by 150 μm, 450 μm, and 700 μm. The spectrum at 700 μm is identical to the one at the strip center (1500 μm). The peak at 1500 μm is normalized to 1, and energy is divided by 662 keV to show the charge collection fraction. In Fig. 71, setup 2 was employed to make the same measurements shown in Fig. 70. These results are nearly identical except that more counts were recorded for setup 1 compared to setup 2.

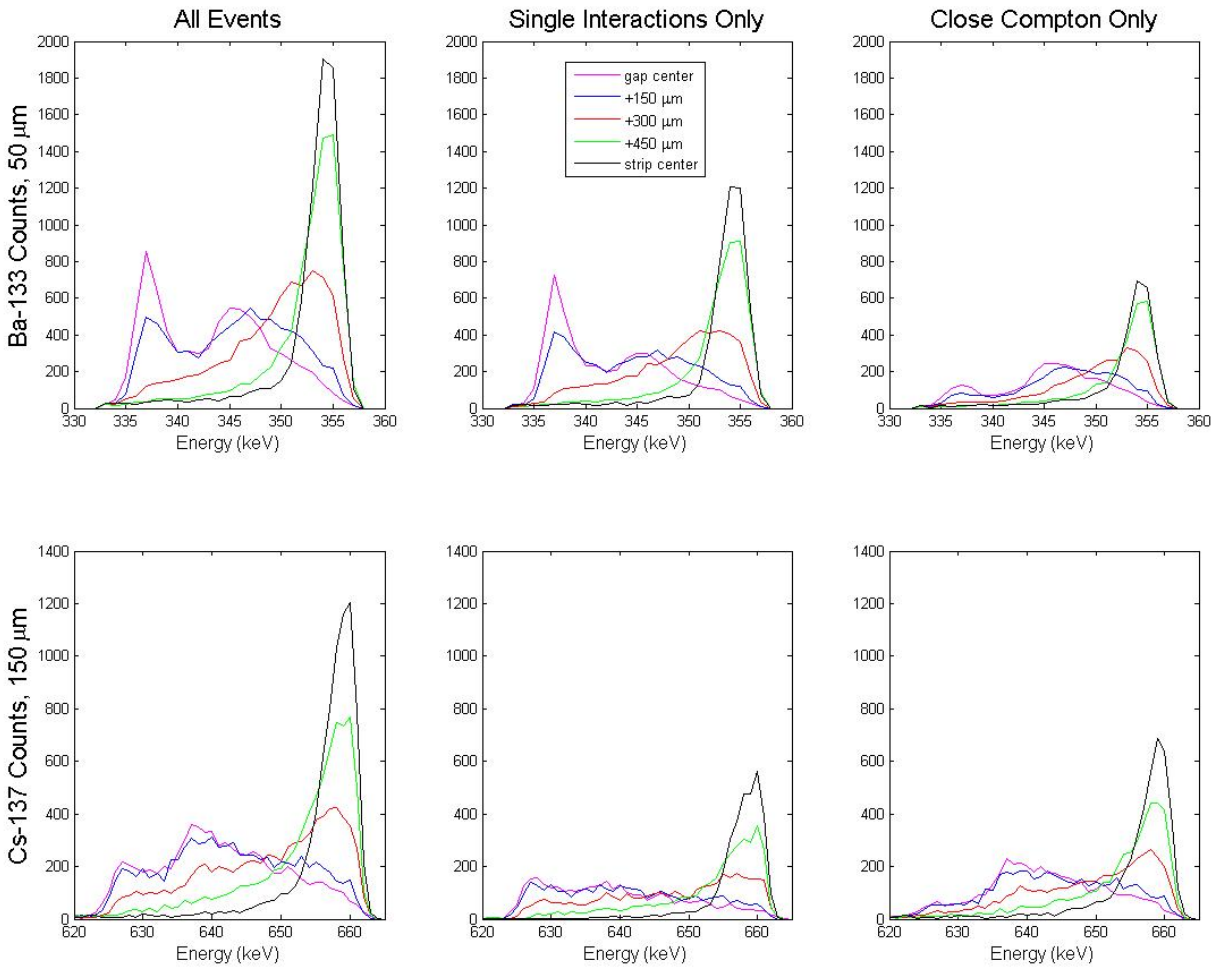

Fig. 72. Charge loss measurements from the Spect32 system are shown for comparison with the measurements shown in Fig. 70 and Fig. 71. The top row shows measurements at 356 keV and the bottom row shows measurements at 662 keV. The column headings indicate whether SSIs, CCEs, or all events are selected. The figure caption indicates collimator positions.

In the bottom row of Fig. 72, charge loss measurements taken by the Spect32 system at 662 keV are shown for comparison with the measurements shown in Fig. 70 and Fig. 71. In the first column, all events have been selected, including SSIs and CCEs. The second (SSI) and third (CCE) columns sum together to produce the result shown in the first column. The Spect32 charge loss measurement setup was similar to setup 1, except that the collimator was opened to 150 μm for the Spect32 measurement to increase the counts at 662 keV. In the Spect32 system, the rise time of the slow trapezoidal filter was set to its maximum of 5 μs for charge loss measurements. Despite these minor differences, the agreement between the measurements acquired with different systems is very good at 662 keV on the anode side. This is also the case at 356 keV on the anode side and at both 356 keV and 662 keV on the cathode side.

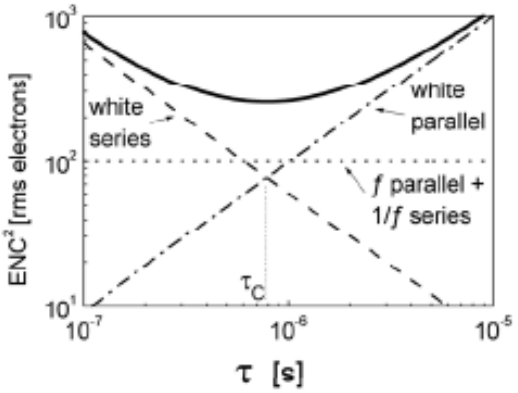

Fig. 73. Illustration of the change in electronic noise components as a function of the peaking time τ of the shaping amplifier [52].

3. Discussion of charge loss measurements, electronic noise, and peaking time

For the Spect32 and NIM acquisition systems employed to make charge loss measurements, charge loss was found to be independent of the selectable peaking time τ. In the Spect32 system, it is possible to select a rise time of up to 5 μs for the trapezoidal

filter. On the ORTEC 572 spectroscopy amplifiers, it is possible to extend the shaping time to up 10 μs, where shaping time is 2.2 τ. The preamplifiers are not cooled on the UM HPGe DSSD, so extension of the peaking time beyond ~10 μs is not expected to improve charge collection or energy resolution because the white parallel $(1/f^2)$ source of electronic noise increases as τ increases. This concept is illustrated in Fig. 73 [52]. Furthermore, some preliminary experiments using an Agilent MSO6104A scope as the acquisition system showed that inductive sources of cross-talk between adjacent preamplifier inputs may also present complications in precisely determining charge collection on adjacent strips over the 300 μs preamplifier fall time. An attempt to dissipate this inductive cross-talk by placing magnetic shielding around the preamplifier box was ineffective.

G. Pulse shape measurements of interactions between strips using a fast oscilloscope

Pulse shape measurements using a fast oscilloscope, which samples at 4 GSa/s, are shown in this section so the reader may obtain a better understanding of the raw fast and slow signals processed by the Spect32 system. Measurements are shown from the four-channel scope because the Spect32 system only allows acquisition of a signal on a single channel at 50 MSa/s. Finally, the processing of measured fast signals by the Spect32 system is simulated.

1. Experimental setup for pulse shape measurements

For measurement of pulse shapes, the detector had five channels instrumented, four adjacent channels on the anode side (DC 11-14) and one on the cathode side. A 662 keV

radiation source was collimated to 70 μm × 500 μm. The 70 μm dimension was aligned to the center of a gap between adjacent anode strips DC12 and DC13, where the gap was centrally located among the four instrumented anode strips. The 500 μm dimension was orientated parallel to each detector surface, grazing the anodesurface of the detector. First interactions occurred across the entire irradiated surface portion of the detector because 662 keV gamma rays are deeply penetrating through centimeters of germanium. This setup is pictured in Fig. 29.

To investigate interactions in the gap between anode strips, events were triggered on coincidence between the cathode strip and at least one of the center two anode strips (DC12 and DC13), with a triggering threshold of ~ 15 keV. On the anode side, triggering off DC 12 alone, DC 13 alone, and coincidence between the two were explored, but little difference was found at the gap center. The cathode signal was digitized at 1 GSa/sec, 8 bits, and 500 MHz bandwidth using an Agilent infiniuum oscilloscope (Model 54810A). Anode strip signals were digitized on a second Agilent oscilloscope at 2 GSa/sec, 8 bits, and 1 GHz (Model MSO6104A). Events were stored for offline analysis by a SPARC workstation. Event energy was determined by averaging slow signals before and after the collection transient and taking the difference, resulting in an energy resolution of ~ 3 keV.

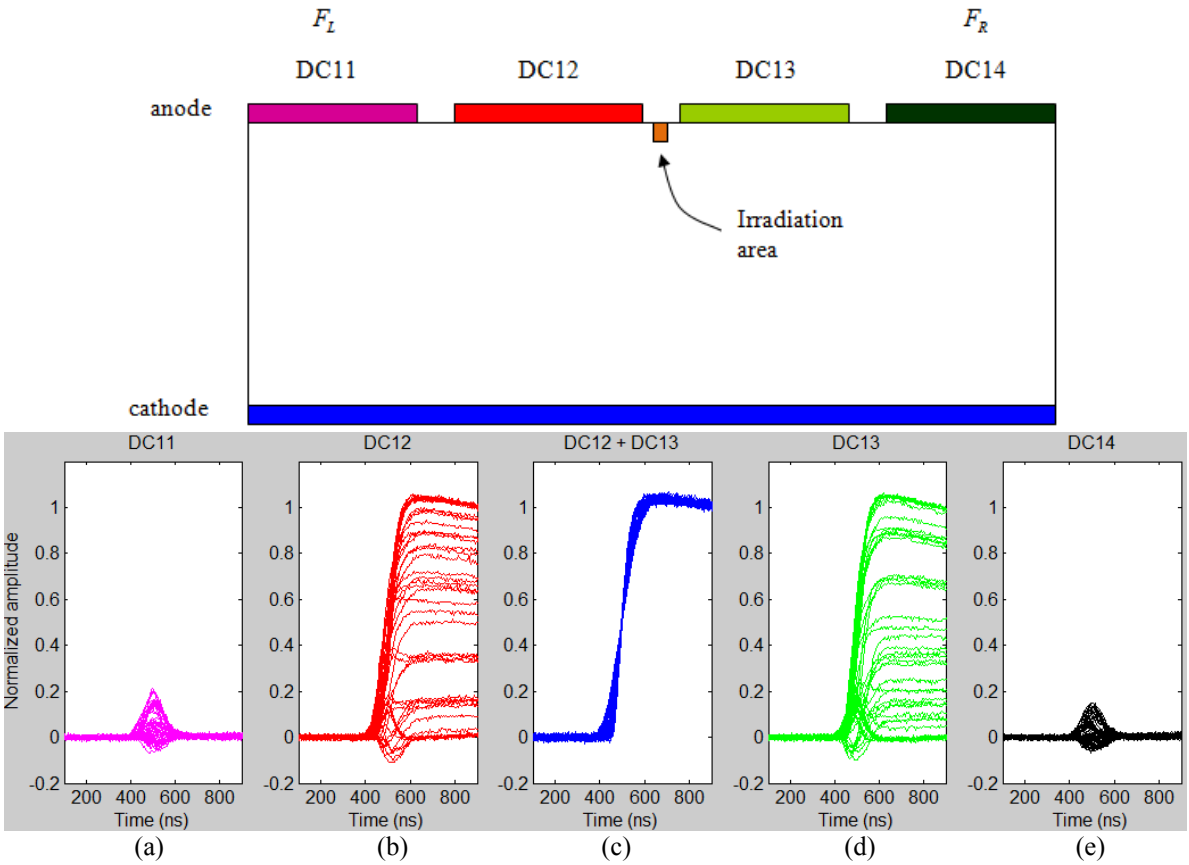

Fig. 74. Signals recorded from anode strips DC 11 (a), DC 12 (b), DC 12 + DC 13 (c), DC 13 (d), and DC 14 (e). The irradiation area is depicted in the schematic above.

2. Pulse shape measurements at the detector surface using a fast oscilloscope

Fig. 74 shows signals recorded from anode strips DC 11 (a), DC 12 (b), DC 12 + DC 13 (c), DC 13 (d), and DC 14 (e). One hundred events which fell within the 662 keV peak with respect to both anode and cathode sides are plotted. The amplitudes of all signals were normalized to 662 keV, and the 50% constant fraction rise time of DC 12 + DC 13 signals were adjusted to 500 ns to make the data easier to see. The scope was triggered off coincidences between the cathode strip and anode strip DC 13.

As with the NIM electronics setup (Section F), it is very difficult to distinguish SSIs from CCEs when using the fast scope as an acquisition system. It may be possible to

infer some information by comparing the rise times of the signals on DC12 and DC13, but no effort was made to do this. Consequently, about half (cf. Fig 66(a)) of the events shown in Fig. 74 are presumed to be due to CCEs.

For 662 keV interactions at the gap center, charge is often collected on both DC 12 and DC 13. Collection on adjacent strips is expected because about half of the events are CCEs, and the most probable value of the charge-splitting ratio $r = 0.5$ for 662 keV SSIs at the gap center. Referring to Fig. 74(c), it appears that the signal-to-noise is high enough at 662 keV to observe charge loss as the pulse height deficit in many of the summed signals, i.e., charge loss may explain some of the vertical broadening.

According to pulse shape simulations (not pictured), the bipolar pulses of non-zero amplitude observed on DC 12 in Fig. 74(b) and DC 13 in Fig. 74(d) are expected for some SSIs near the detector surface. For SSIs near the detector surface, bipolar pulses are expected on either DC 12 or DC 13, depending on which strip collects the greatest fraction of charge-carriers. These signals should have amplitude with magnitude less than 10% of the sum of DC 12 + DC 13. Furthermore, referring to Fig. 74(a) and Fig. 74(e), fast signals of negative or bipolar amplitude are expected for SSIs near the detector surface. These fast signals should have amplitude with magnitude less than 10% of the sum of DC 12 + DC 13. For interactions closer to the cathode side, unipolar fast signals of positive polarity are expected. According to simulation, these fast signals should have amplitude with magnitude less than 20% of the sum of DC 12 + DC 13. Thus, the following attest to the presence of CCEs in the data: 1) the infrequence of observed bipolar signals of non-zero amplitude in Fig. 74(b) and Fig. 74(d), and 2) the presence of

many unipolar fast signals of positive polarity in Fig. 74(a) and Fig. 74(e). In the CCEs, the first interaction is constrained to occur at the anode surface in the gap between strips, but the subsequent interaction(s) many occur anywhere within the lateral bounds of DC12 or DC13.

3. Simulated shaping of measured fast signals by the Spect32 system

This section is meant to provide a better understanding of the fast energies recorded by the Spect32 system. A fast energy is defined as a peak-to-peak measurement recorded for a shaped fast signal. The Spect32 system records fast energies on each detector channel when any single channel fires. However, the only fast energies useful for lateral interpolation are the ones recorded on the strips adjacent to firing strips. Furthermore, the firing strip must be triggered by an in-strip SSI. As mentioned in Section A, the optimal fast filter for lateral position interpolation of SSIs was found to be a triangular filter with 60 ns rise and fall times.

Fig. 75 displays simulated filtering of a subset of the measured fast signals shown in Fig. 74(a) and 74(e). The raw fast signals are shown in the top row, and the shaped signals in the bottom row have been convolved with a triangular filter which has 60 ns rise and fall times. For each simulated event, raw and shaped signals appear in the same color. The quantization error introduced in the Spect32 system by sampling fast signals at 50 MHz is not simulated.

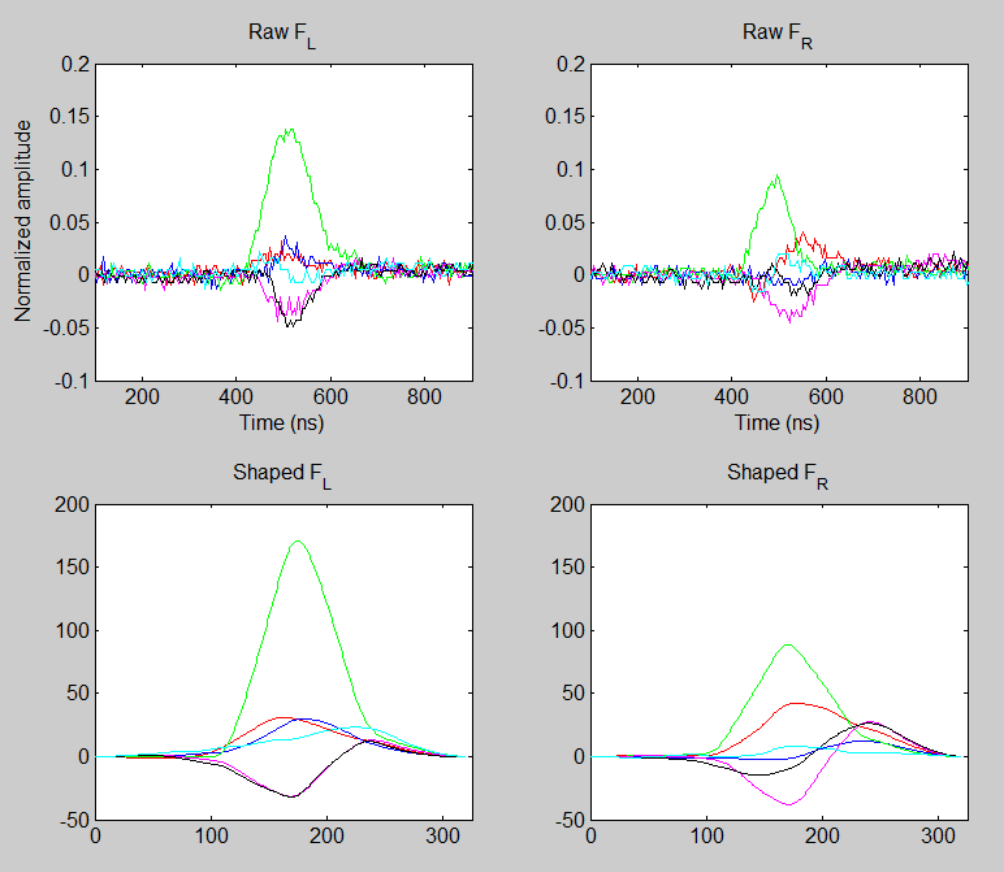

Fig. 75. Simulated filtering of a subset of the measured fast signals shown in Fig. 74(a) and 74(e). The raw signals are shown in the top row. Fast energies on adjacent strips are determined from peak-to-peak measurements of the shaped fast signals (bottom row).

In Fig. 75, the polarity of the raw fast signals is observed to be the same as the polarity of the shaped signals. Furthermore, the fast filter removes electronic noise from the raw signals. This allows for a more precise measurement of the fast energies on adjacent strips, which are determined from the difference in the numbers corresponding to the max and min values of the shaped fast signal. Thus, a recorded fast energy effectively measures the magnitude of the ripple in a fast signal. These observations are relevant to fast signals which are measured on either side of one or two adjacent firing strips. The case of a single adjacent firing strip is shown in Fig. 60, Fig. 61, and Fig. 62(a). The case of two adjacent firing strips is shown in Fig. 55, Fig. 62(b), and Fig. 74.

Bibliography

[1] S. Boggs et al. (2005, Dec.). NASA vision mission concept study report: Advanced Compton Telescope. [Online]. Available: http://arxiv.org/abs/astro-ph/0608532.

[2] F. Lebrun, "The ISGRI CdTe gamma camera in-flight performance," *IEEE Trans. Nuc. Sci.*, vol. 52, pp. 3119-3123, Dec. 2005.

[3] PHDs Co., 777 Emory Valley Rd, Suite B, Oak Ridge, TN, 37830, http://www.phdsco.com/index.html

[4] Private communication with Ethan Hull, 2/9/06.

[5] D. Protic and T. Krings, "Detection Characteristics of Ge detectors with microstructured amorphous Ge contacts," *IEEE Trans. Nucl. Sci.*, vol. 51, pp. 1129-1133, Jun. 2004.

[6] M. Amman, P.N. Luke, S.E. Boggs, "Amorphous-semiconductor-contact germanium based detectors for gamma-ray imaging and spectroscopy," *NIM A*, vol. 579, pp. 886-890, Sep. 2007.

[7] Z. He, "Review of Shockley-Ramo theorem and its application in semiconductor gamma-ray detectors," *NIM A*, vol. 463, pp. 250-267, May 2001.

[8] A.J. Tavendale, G.T. Ewan, *NIM A*, vol. 25, pp. 185, 1963.

[9] R.H. Pehl, R.C. Cordi, F.S Goulding, in *IEEE Trans Nuc Sci*, NS-19, 1972, pp. 265.

[10] R.M. Keyser and T.W. Raudorf, "Germanium radiation detector manufacturing," *NIM A*, vol. 286, pp. 357-363, Jan. 1990.

[11] P.N. Luke et al., "Amorphous Ge bipolar blocking contacts on Ge detectors," *IEEE Trans. Nuc. Sci.*, vol. 39, pp. 590-594, Aug. 1992.

[12] S.R. Amendolia et al., "Germanium microstrip detectors with 50 and 100 μm pitch," *NIM A*, vol. 226, pp. 117-121, Sep. 1984.

[13] M. Amman and P.N. Luke, "Three-dimensional position sensing and field shaping in orthogonal-strip germanium gamma-ray detecors," *NIM A*, vol. 452, pp. 155-166, Sep. 2000.

[14] E.L. Hull and R.H. Pehl, "Amorphous germanium contacts on germanium detectors," *NIM A*, vol. 538, pp. 651-656, Feb. 2005.

[15] Private communication with Ethan Hull, 5/25/06.

[16] D. Protic and T. Krings, "Microstructures on Ge detectors with amorphous Ge contacts," *IEEE Trans. Nucl. Sci.*, vol. 50, pp. 998-1000, Aug. 2003.

[17] J. Marler and V. Gelezunas, *IEEE Trans. Nucl. Sci.*, NS-20, No. 1, 1973.

[18] R.E. Stone et al., *IEEE Trans. Nuc. Sci.*, NS-33, No. 1, 1986.

[19] D.L. Upp et al. (2004, Sep.). New cooling methods for HPGe detectors and associated electronics. ORTEC, Oak Ridge, TN. [Online]. Available: www.ortec-online.com/papers/new_cooling.pdf

[20] E. Broerman et al. (2004, Sep.). Performance of a New Type of Electrical Cooler for HPGe Detector Systems. ORTEC, Oak Ridge, TN. [Online]. Available: www.ortec-online.com/papers/inmm_xcool.pdf

[21] The ORTEC Detectives High Purity Germanium Portable Nuclide Identifiers. (2004, Jun.). ORTEC, Oak Ridge, TN. [Online]. Available: www.ortec-online.com/ pdf/detective_ppt.pdf

[22] R.A. Kroeger et al., "Charge spreading and position sensitivity in a segmented planar germanium detector," *NIM A*, vol. 422, pp. 206-210, Feb. 1999.

[23] M. Burks et al., "Signal interpolation in germanium detectors for improved 3-D position resolution," in *IEEE NSS Conf. Record*, vol. 2, 2004, pp. 1114-1118.

[24] E.A. Wulf et al., "Strip interpolation in silicon and germanium strip detectors," in *IEEE NSS Conference Record*, vol. 2, 2004, pp. 925-929.

[25] P. Sangsingkeow et al., "Advances in germanium detector technology," *NIM A*, vol. 505, pp. 183-186, Jun. 2003.

[26] K. Vetter et al., "Performance of the GRETA prototype detectors," *NIM A*, vol. 452, pp. 105-114, Sep. 2000.

[27] Mihailescu et al., "Methods for increasing the efficiency of Compton imagers," presented at the IEEE NSS, San Juan, Puerto Rico, 2005.

[28] R.A. Kroeger et al., “Three-Compton telescope: theory, simulations, and performance,” *IEEE Trans. Nuc. Sci.*, vol. 49, pp. 1887-1892, Aug. 2002.

[29] D.M. Smith et al., “The HESSI spectrometer,” ASP Conferences Series, vol. xxx, 2000. [Online]. Available: hesperia.gsfc.nasa.gov/hessi/Data_Analysis/spectroscopy/ds_paper.ps

[30] G.D. Holman. (2006, Dec.). RHESSI Home Page at NASA Goddard Space Flight Center. [Online]. Available: http://hessi.ssl.berkeley.edu/instrument/germanium.html

[31] C.E. Svensson et al., “Position sensitivity of the TIGRESS 32-fold segmented HPGe clover detector,” *NIM A*, vol. 540, pp. 348-360, Mar. 2005.

[32] I.Y. Lee et al., “Developments in large gamma-ray detector arrays,” *Rep. Prog. Phys.*, vol. 66, pp. 1095-1144, Jul. 2003.

[33] M.A. Deleplanque et al., “GRETA: utilizing new concepts in γ–ray detection,” *NIM A*, vol. 430, pp. 292-310, Jul. 1999.

[34] G. Nellis et al., “Reverse Brayton Cryocooler for NICMOS” in *Cryocoolers 10*, Springer US, 1999, pp. 431-438.

[35] G. Rossi, J. Morse, D. Protic, “Energy and position resolution of germanium microstrip detectors at X-ray energies from 15 to 100 keV,” *IEEE Trans. Nuc. Sci.*, vol. 46, pp. 765-773, Jun. 1999.

[36] G. Rossi et al., “X-ray response of germanium microstrip detectors with energy and position resolution,” *NIM A*, vol. 392, pp. 264-268, Jun. 1997.

[37] W. Coburn et al., “Results of charge sharing tests in a Ge-strip detector,” NSS Conf. Record, Nov. 2001 IEEE, vol. 1, pp. 226-229.

[38] S. Amrose et al., “Numerical simulations of 3D positioning in cross-strip Ge detectors,” NSS Conf. Record, Nov. 2001 IEEE, vol. 1, pp. 230-233.

[39] S. Agostinelli et al., “Geant4—a simulation toolkit,” *NIM A*, vol. 506, pp. 250-303, Jul. 2003.

[40] ICRU Report 37, 1984.

[41] K. Vetter et al., “Three-dimensional position sensitivity in two-dimensionally segmented HP-Ge detectors,” *NIM A*, vol. 452, pp. 223-238, Sep. 2000.

[42] Ansoft, 225 W Station Square Dr, Suite 200, Pittsburgh PA 15219, http://www.ansoft.com/products/em/max3d/

[43] G.F. Knoll, Radiation Detection and Measurement, 3rd ed., John Wiley & Sons, Inc. New York, 2000, pp. 356, 379, 410.

[44] Synopsys, 700 E Middleview Rd, Mountain View, CA 94043, http://www.synopsys.com/products/mixedsignal/taurus/device_sim_ds.html

[45] M. Cunningham et al., "First-generation hybrid compact Compton imager," in *IEEE NSS Conf. Record*, vol. 1, Oct. 2005, pp. 312-315.

[46] Private communication with Dr. Gene Haller, LBNL, 7/5/2007.

[47] Private communication with Ethan Hull, 8/22/07.

[48] K. Vetter et al., "High-sensitivity Compton imaging with position sensitive Si and Ge detectors," *NIM A*, vol. 579, pp. 363-366, Aug. 2007.

[49] M.J. Berger et al., XCOM: Photon Cross Sections Database, [Online]. Available: http://physics.nist.gov/PhysRefData/Xcom/Text/XCOM.html.

[50] D. Xu and Z. He, "Gamma-ray energy-imaging integrated spectral deconvolution," *NIM A*, vol. 574, pp. 98-109, Apr. 2007.

[51] J.P. Hayward and D.K. Wehe, "Observation of charge-sharing in an HPGe double-sided strip detector," *NIM A*, vol. 579, pp. 99-103, Aug. 2007.

[52] V. Radeka, "Detector Signal Processing," presented at the IEEE NSS, Honolulu, Hawaii, 2007. [Online]. Available: http://www.inst.bnl.gov/nss07/